U.S. Department of Transportation

Federal Railroad Administration

Field Investigation and Modeling of Track Substructure Performance Under Trains Moving at Critical Speed

Office of Research, Development
and Technology
Washington, DC 20590

DOT/FRA/ORD-18/21

Final Report
July 2018

REPORT DOCUMENTATION PAGE

Form Approved
OMB No. 0704-0188

1. AGENCY USE ONLY (Leave blank)	2. REPORT DATE	3. REPORT TYPE AND DATES COVERED
	July 2018	Technical Report – September 2015

4. TITLE AND SUBTITLE	5. FUNDING NUMBERS
Field Investigation and Modeling of Track Substructure Performance Under Trains Moving at Critical Speed	DTFR53-12-C-00029
6. AUTHOR(S) Aaron Judge, Carlton Ho, Hai Huang, James Hyslip, and Yin Gao	
7. PERFORMING ORGANIZATION NAME(S) AND ADDRESS(ES) Penn State 110 Technology Center University Park, PA 16802	8. PERFORMING ORGANIZATION REPORT NUMBER
9. SPONSORING/MONITORING AGENCY NAME(S) AND ADDRESS(ES) U.S. Department of Transportation Federal Railroad Administration Office of Railroad Policy and Development Office of Research, Development and Technology Washington, DC 20590	10. SPONSORING/MONITORING AGENCY REPORT NUMBER DOT/FRA/ORD-18/21

11. SUPPLEMENTARY NOTES
COR: Cameron D. Stuart

12a. DISTRIBUTION/AVAILABILITY STATEMENT	12b. DISTRIBUTION CODE
This document is available to the public through the FRA Web site at http://www.fra.dot.gov.	

13. ABSTRACT (Maximum 200 words)

The purpose of this research performed by Pennsylvania State University between September 2012 and September 2015 was to formulate and validate a 3D dynamic track-subgrade interaction model, to conduct field measurements of subgrade conditions and track responses to train passes at a variety speeds, and to use the model to predict the track performance when trains run at critical speed. When a train approaches critical speed, vibrations propagate within the track structure and subgrade at a speed close to the Rayleigh wave velocity of the subgrade soil. Ground vibrations combine in-phase, resulting in significantly increased vibrations in the track system, adjacent soil deposits, and adjacent structures. Field sites with soft subgrade properties were selected to validate the model. Based on the study's results, the 3D dynamic track-subgrade interaction model is an effective way to predict the track performance and critical speed condition of the track.

14. SUBJECT TERMS	15. NUMBER OF PAGES
Track-subgrade modeling, field validation, critical speed, high-speed rail, ground vibration, ground penetrating radar, GPR	97
	16. PRICE CODE

17. SECURITY CLASSIFICATION OF REPORT	18. SECURITY CLASSIFICATION OF THIS PAGE	19. SECURITY CLASSIFICATION OF ABSTRACT	20. LIMITATION OF ABSTRACT
Unclassified	Unclassified	Unclassified	

NSN 7540-01-280-5500

Standard Form 298 (Rev. 2-89)
Prescribed by ANSI Std. 239-18
298-102

METRIC/ENGLISH CONVERSION FACTORS

ENGLISH TO METRIC

LENGTH (APPROXIMATE)

1 inch (in)	=	2.5 centimeters (cm)
1 foot (ft)	=	30 centimeters (cm)
1 yard (yd)	=	0.9 meter (m)
1 mile (mi)	=	1.6 kilometers (km)

AREA (APPROXIMATE)

1 square inch (sq in, in^2)	=	6.5 square centimeters (cm^2)
1 square foot (sq ft, ft^2)	=	0.09 square meter (m^2)
1 square yard (sq yd, yd^2)	=	0.8 square meter (m^2)
1 square mile (sq mi, mi^2)	=	2.6 square kilometers (km^2)
1 acre = 0.4 hectare (he)	=	4,000 square meters (m^2)

MASS - WEIGHT (APPROXIMATE)

1 ounce (oz)	=	28 grams (gm)
1 pound (lb)	=	0.45 kilogram (kg)
1 short ton = 2,000 pounds (lb)	=	0.9 tonne (t)

VOLUME (APPROXIMATE)

1 teaspoon (tsp)	=	5 milliliters (ml)
1 tablespoon (tbsp)	=	15 milliliters (ml)
1 fluid ounce (fl oz)	=	30 milliliters (ml)
1 cup (c)	=	0.24 liter (l)
1 pint (pt)	=	0.47 liter (l)
1 quart (qt)	=	0.96 liter (l)
1 gallon (gal)	=	3.8 liters (l)
1 cubic foot (cu ft, ft^3)	=	0.03 cubic meter (m^3)
1 cubic yard (cu yd, yd^3)	=	0.76 cubic meter (m^3)

TEMPERATURE (EXACT)

[(x-32)(5/9)] °F	=	y °C

METRIC TO ENGLISH

LENGTH (APPROXIMATE)

1 millimeter (mm)	=	0.04 inch (in)
1 centimeter (cm)	=	0.4 inch (in)
1 meter (m)	=	3.3 feet (ft)
1 meter (m)	=	1.1 yards (yd)
1 kilometer (km)	=	0.6 mile (mi)

AREA (APPROXIMATE)

1 square centimeter (cm^2)	=	0.16 square inch (sq in, in^2)
1 square meter (m^2)	=	1.2 square yards (sq yd, yd^2)
1 square kilometer (km^2)	=	0.4 square mile (sq mi, mi^2)
10,000 square meters (m^2)	=	1 hectare (ha) = 2.5 acres

MASS - WEIGHT (APPROXIMATE)

1 gram (gm)	=	0.036 ounce (oz)
1 kilogram (kg)	=	2.2 pounds (lb)
1 tonne (t)	=	1,000 kilograms (kg)
	=	1.1 short tons

VOLUME (APPROXIMATE)

1 milliliter (ml)	=	0.03 fluid ounce (fl oz)
1 liter (l)	=	2.1 pints (pt)
1 liter (l)	=	1.06 quarts (qt)
1 liter (l)	=	0.26 gallon (gal)
1 cubic meter (m^3)	=	36 cubic feet (cu ft, ft^3)
1 cubic meter (m^3)	=	1.3 cubic yards (cu yd, yd^3)

TEMPERATURE (EXACT)

[(9/5) y + 32] °C	=	x °F

QUICK INCH - CENTIMETER LENGTH CONVERSION

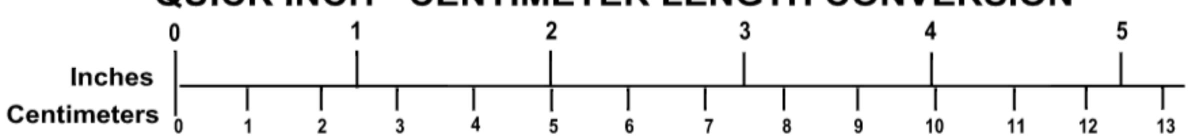

QUICK FAHRENHEIT - CELSIUS TEMPERATURE CONVERSION

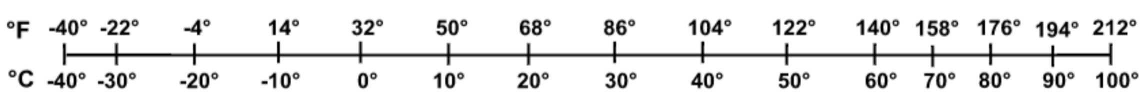

For more exact and or other conversion factors, see NIST Miscellaneous Publication 286, Units of Weights and Measures. Price $2.50 SD Catalog No. C13 10286

Updated 6/17/98

Contents

Illustrations

Tables

Executive Summary

Pennsylvania State University, in partnership with Amtrak, the University of Massachusetts, and HyGround Engineering performed work sponsored by the Federal Railroad Administration to study the effect of higher train speeds in areas having relatively soft subgrade conditions. This project was conducted between September 2012 and September 2015. The work that was performed included:

1. Conducting a comprehensive field investigation, including both laboratory testing and on-site characterization, of a problem site, Great Swamp National Wildlife Refuge, in Kingston, RI.
2. Creating an instrumentation plan for quantitatively evaluating track vibrations and its change under different train speeds.
3. Modifying and validating a three-dimensional (3D) dynamic track-subgrade interaction model to study the track performances and critical speed phenomenon. This track model was also used to predict track performance out of physical range.

Amtrak identified the need to investigate the Northeast Corridor (NEC) site at Kingston because it was suspected that a condition called critical speed might exist at this location. Normally, a railroad system's critical speed is the speed at which vibrations propagate within the track structure and subgrade at a speed close to the Rayleigh wave velocity of the subgrade soil. As trains travel at speeds approaching the critical speed, track vibrations are significantly increased. The increased vibration levels can lead to higher levels of track degradation and, if speeds are sufficiently high, may pose a risk of train derailment.

The field measurements were made during regional and high speed (Acela) passes. Track soil characteristics were determined using Dynamic Cone Penetrometer (DCP) and the Spectral Analysis of Surface Waves (SASW). Light Detection and Ranging (LiDAR) and ground penetrating radar (GPR) data were also provided, giving the detailed information of cross sections and layers. Track responses to train passes were measured with accelerometers.

Field data demonstrated that the track experienced the cone-shaped surface wave motion characteristic of the critical speed phenomena at speeds as low as 90 km/hr. Higher train speeds (200 km/hr) cause larger, nonlinear rail vertical deflections. However, the rail deflection did not have a significant increase within the current operational speeds according to field measurements. However, even though the rail deflection increased in a nonlinear behavior, the magnitude of the increased deflection was not significant at these speeds.

A 3D dynamic track-subgrade interaction model was modified and validated to further explore the track performance with higher train speeds and stress intensity in the cross section. Results from the field measurements (as well as the computer model) showed the rail deflection did not significantly increase under current operational speeds. However, cone-shaped ground surface wave motions were observed, even at the speed of 90 km/hr. This means the cone-shaped surface wave motion and the increase in rail deflection did not occur at the same time. The modeling revealed a phenomenon that might be significant: high level of stress concentration within the track cross section started when cone-shaped ground surface wave motion occurred. Further, the model predicted that significantly increased rail deflection will not happen until train speed reaches 300 km/hr.

In summary, the field investigations had accurately measured the track performance at various train speeds and successfully validated the 3D dynamic track-subgrade interaction model. Even though the track deflection at current operational speeds did not exhibit significant increase, the modeling results showed high-level of stress at current operational speed of Acela trains. The model may indicate why this track segment required high maintenance. By increasing the speed to over 300 km/hr in the model, both the stress level and rail displacement will be substantially increased.

Additional research is recommended to quantify ballast particle movement under these conditions. These results will help to confirm the relationship between train speeds, soil characteristics, and the need for increased track maintenance.

1. Introduction

A project conducted between September 2012 and September 2015 by Pennsylvania State University (Penn State Altoona), in partnership with Amtrak, the University of Massachusetts, and HyGround Engineering was sponsored by the Federal Railroad Administration (FRA) to study the effect of higher train speeds in areas having relatively soft subgrade conditions. The following sections will outline a comprehensive field investigation of a problem site in Kingston, RI's, Great Swamp National Wildlife Refuge (commonly known as the Great Swamp) with the creation of an instrumentation plan for quantitatively evaluating track vibrations and the subgrade's change under different train speeds and a modified three-dimensional (3D) dynamic track-subgrade interaction model to study the track performances and critical speed phenomenon.

1.1 Background

High-speed rail (HSR) has become a powerful technological advancement in the transportation industry due to its environmentally friendly performance and time savings for passengers. Over 10,000 miles of HSR rail have been built across the globe. Increasing speeds bring many challenges to railway systems, including train control, passenger safety and comfort, and hazards from noise and vibrations. This research focuses on ground-borne vibration induced by HSR. Increased vibrations from higher speed trains, combined with relatively soft subgrade conditions can accelerate track deterioration of tracks and can damage track components, degrade passenger comfort, and may negatively impact operational safety.

When high-speed trains run over soft ground, where Rayleigh waves travel slower, a significant increase in vibration level can occur as train speeds approach the critical speed of the overall system. The critical speed is classically defined as the speed at which vibrations propagate within the track structure and subgrade at a speed close to the Rayleigh wave velocity of the subgrade soil.

As a train's speed approaches the Rayleigh wave speed, any soil that has a low shear-wave velocity will experience increased degradation due to resonant forces within the soft subgrade. High vibration levels lead to safety limits on train speed. The critical speed effect also causes a cone-shaped wave motion in the ground surface. As can be seen in Figure 1, the displacement of the ground surface resembles a cone-shaped wave motion as the train speed increases.

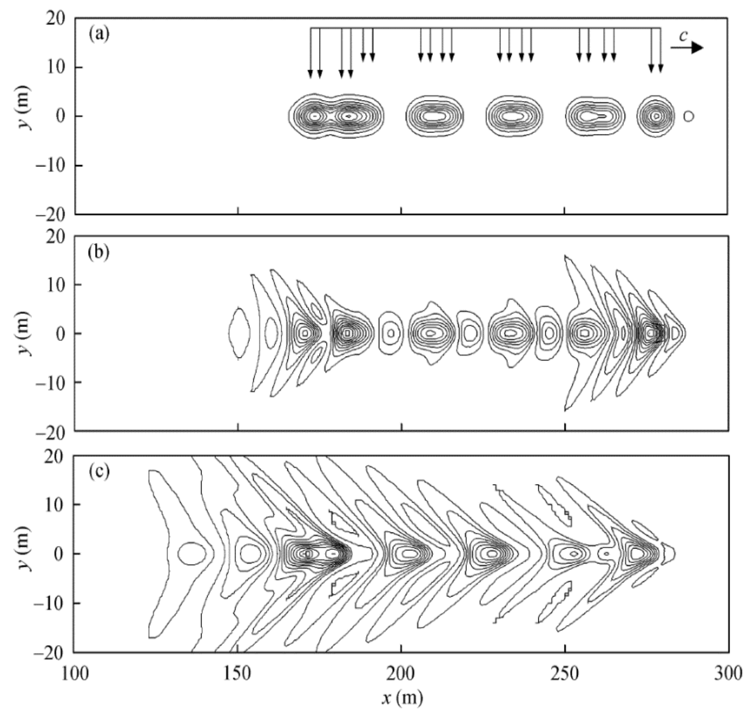

Figure 1. Vertical Displacement Fields of the Ground Surface When Train Running at Different Speeds (a) c=100km/h; (b) c=200km/h; (c) c=300km/h (Bian, 2008)

For example, the X-2000 (Swedish HSR) was running at the maximum speed on the Goteborg-Malmo line in 1997 when it generated excessive vibration in the soil and overhead contact line support poles (Galvin, 2009). Furthermore, at Ledsgard, Sweden, a new railway line with a design speed of 200 km/h has generated high vibrations on soft cohesive soil. As a result, the train speeds were decreased from 200 km/h to 160 km/h, and then to 130 km/h (Berggren, 2002). The high vibrations were caused by train speeds that were approaching critical speed. A similar phenomenon also occurred on the Northern Ireland Railways where the subgrade is constructed on soft, peaty soils (Barbour, 2010).

1.2 Objectives

The following were the objectives of this research:

- To perform comprehensive field instrumentation and testing for track responses near Kingston site for various train speeds.
- To conduct field validation tests at applicable sites with varying speeds to verify the accuracy of a previously developed track model.
- To use the model and field investigations to evaluate the track performance under different speed and loading conditions. Clearly define the concept of critical speed and its impact on track performances and safety.

1.3 Overall Approach

Penn State Altoona's approach to this project was to collect field data from in service railroad tracks that carry high-speed passenger traffic and compare the data to the results of a concurrently developed analytical model of the track structure. The effort involved support from Amtrak and other universities and private firms.

1.4 Scope

The project met the objectives by:

1. Conducting comprehensive field investigation of the problem site including both laboratory testing and on-site characterization.
2. Creating an instrumentation plan that is designed to quantitatively evaluate track vibration and its change under different train speeds.
3. Modifying and validating a three-dimensional (3D) dynamic track-subgrade interaction model to study the track performances and critical speed phenomenon. This track model will also be utilized to predict track performance out of physical range.

1.5 Organization of the Report

This report provides documentation of the project activities and presents the results. The report is organized as follows:

Section 1: Introduction – Introduces the concept of critical speed and presents the scope and approach to the project

Section 2: Field Investigation – Describes the work conducted at filed locations to gather relevant data

Section 3: Validation of A Dynamic Track-Subgrade Interaction Model – Discusses the dynamic track model and how it was used to predict the behavior of the track structure in response to train traffic.

Section 4: Model Prediction and Analysis – Presents the results of the project

Section 5: Conclusion – Summarizes the results of the project and presents areas for future research.

2. Field Investigation

Obtaining field data was an important aspect of the project. These data were used to train and validate the analysis model. This section describes the activities related to field data gathering on Amtrak.

2.1 Site Information

The Northeast Corridor (NEC) is a rail line owned primarily by Amtrak, which runs 731 km from Boston, MA, to Washington, DC. This line has sections of Class 8 Track that allow speeds of 250 km/hr. The NEC is not restricted to HSR trains (the Acela), it also serves regional passenger trains as well as commuter and freight trains.

This study focuses on a straight section of NEC track that is currently classified for speeds up to 250 km/hr. This track runs northeast/southwest through the northern section of the Great Swamp National Wildlife Refuge (commonly known as the Great Swamp area), west of South Kingston, RI. It is used for both HSR trains and regional passenger trains. The ties are concrete and the rail weight is 56 kg/m.

Some geotechnical and geophysical test methods were used to determine the track condition and site geological information. Dynamic Cone Penetrometer (DCP) testing was performed by the authors to determine the soil modulus and changes in the layers. HyGround Engineering used ground penetrating radar (GPR) to obtain the layer depths, fouling index, and moisture. Light Detection and Ranging (LIDAR) was used to determine the cross sections and Spectral Analysis of Surface Wave (SASW) tests were performed to calculate the shear wave velocity profiles. Laboratory tests were performed, such as bender elements (a lab test to measure the shear wave velocity of soil), to estimate the soil's shear wave velocity. Shear vane and fall cone tests were performed to determine shear strength and modulus. Water content and density were also measured.

2.1.1 Site Geological Information

The location of the Rhode Island test site area is shown in Figure 2. Testing was performed at two locations in the Great Swamp shown in Figure 3. Track 1 (Southbound) was used for all tests due to access restrictions.

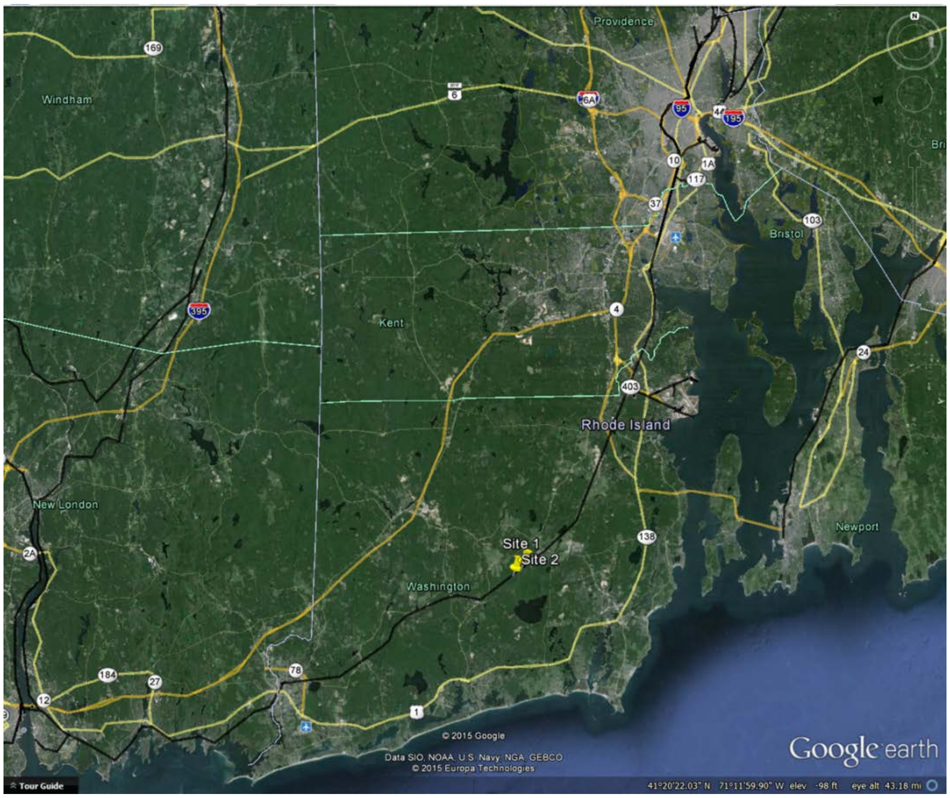

Figure 2. Kingston Site Location in Southern Rhode Island

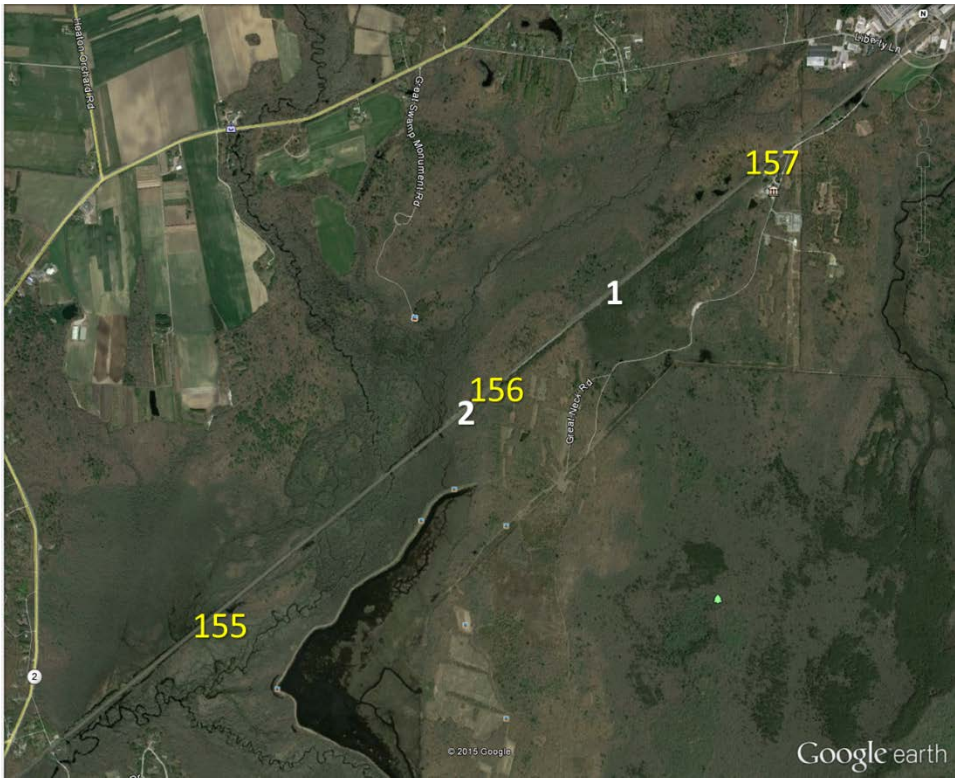

Figure 3. Test Sites 1 and 2 at Kingston, RI

The surficial geology in the Great Swamp is comprised entirely of various glacial deposits (moraines, kames, outwash, etc.) or swamp deposits. The soil deposits are dominated by ground moraine, subglacial till, undifferentiated ice contact deposits, and an organic swamp soil deposit. The glacial ground moraine is a light-colored deposit consisting of uniform fine sand. The ground moraine is a competent material for foundations as it is generally strong. The subglacial till and undifferentiated ice contact deposits have many of the same engineering characteristics of the ground moraine, which is underneath the swamp deposits. As a result of the uneven glacial melting, the ground moraine has a hummocky topography that results in a variation in elevation and swamp deposit thickness. The swamp deposits consist of normally consolidated dark organic clays and silts which are generally soft and deformable. The thickness of the swamp deposits varies from 2 m to 7.5 m, with most of the deposits having the lower range of thickness. It would not be uncommon to find peaty soil with high water content that has Rayleigh wave velocities as low as 110 km/hr to 140 km/hr. Figure 4 presents a surficial Geology map by Kaye (1960) with the mileposts and sites marked.

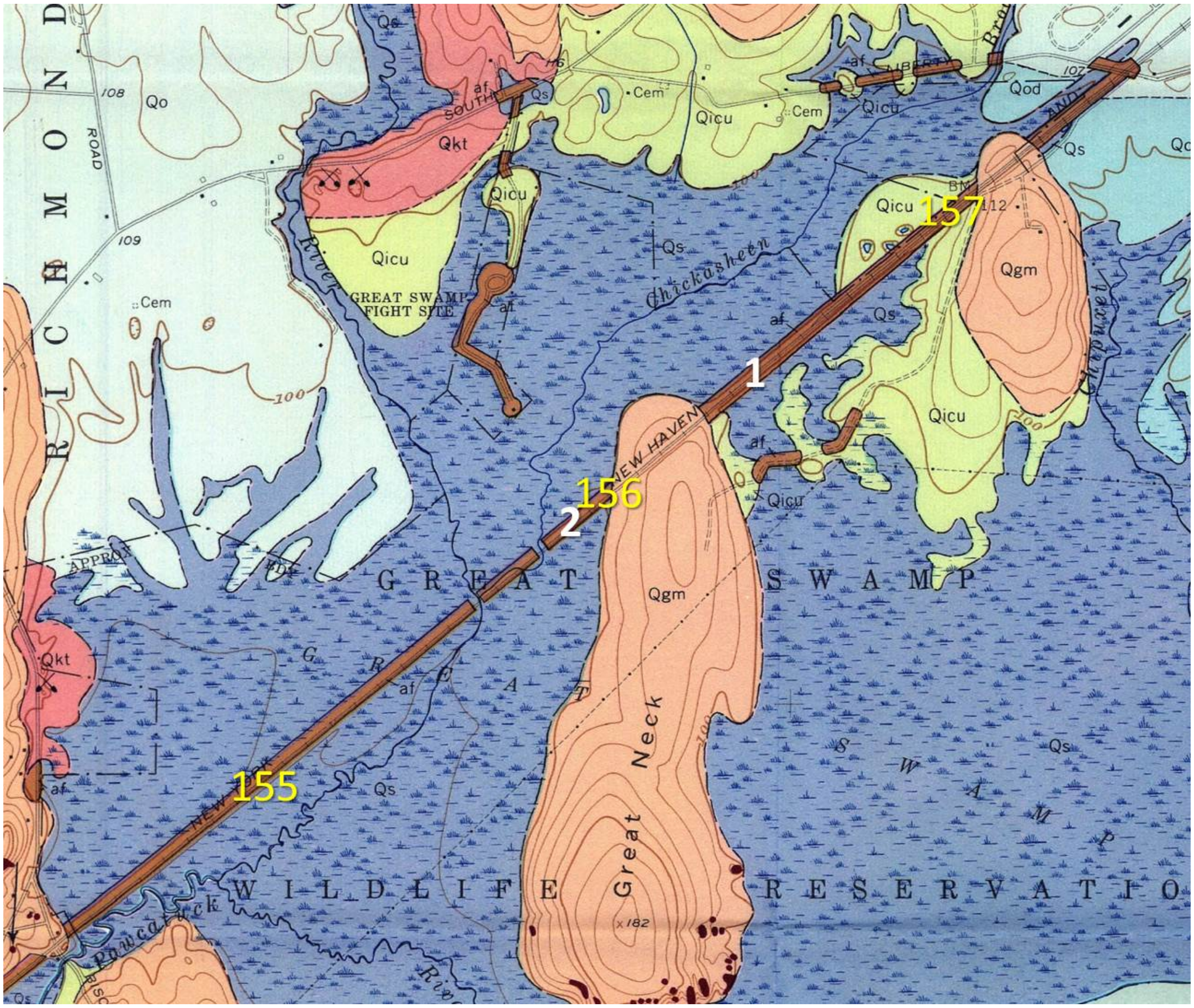

Figure 4. Surficial Geology Map by Kaye (1960) with the Mileposts and Sites Marked

2.2 GPR and LIDAR

GPR was collected at the sites by HyGround Engineering in June 2011. A high-rail truck with antennas mounted on the left, center, and right sides of Track 1 was used to survey the track. The data were processed to estimate the fouling indices, layer depths, and moisture profiles as shown in Figure 5 through Figure 7. Geometry and LIDAR data are also shown with the GPR data. LIDAR data were provided for the track and right of way which helped in the selection of the sites. These data were zeroed to Track 1 which gave the cross sections at the sites that were used in the model.

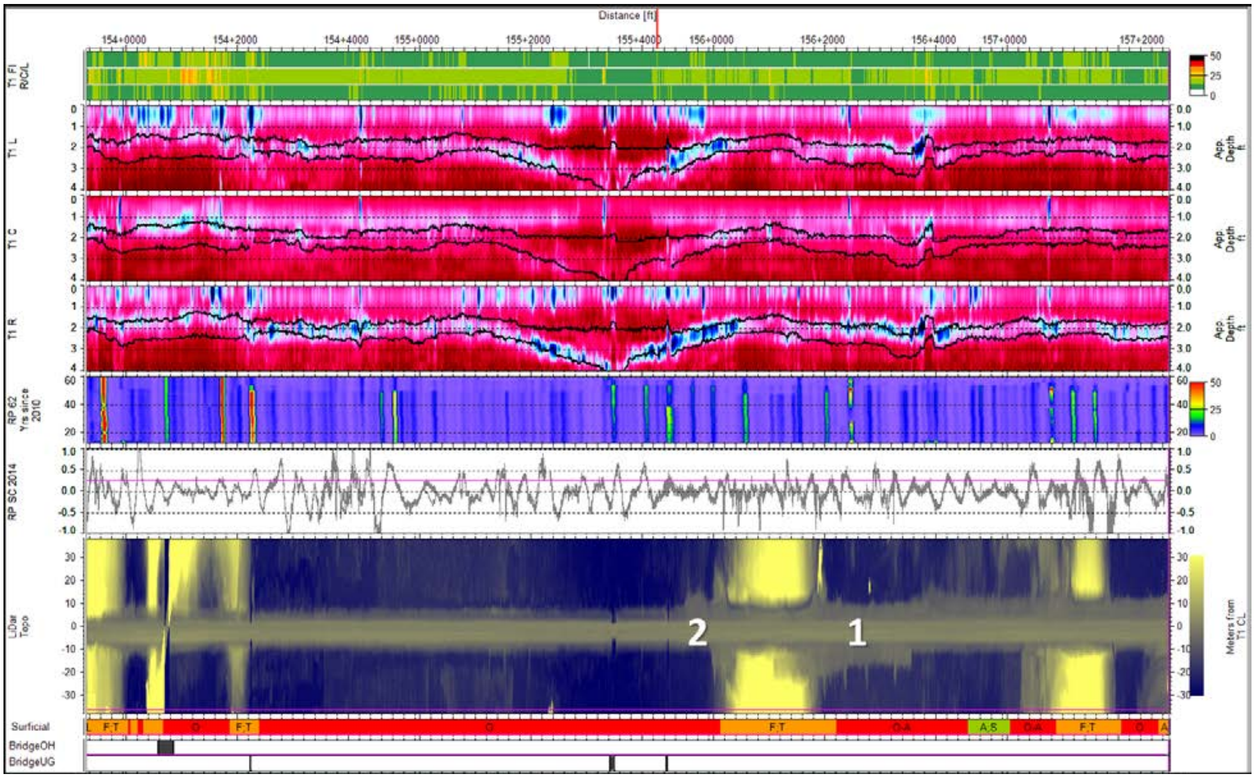

Figure 5. LIDAR, GPR, and Geometry Data at the Kingston Sites

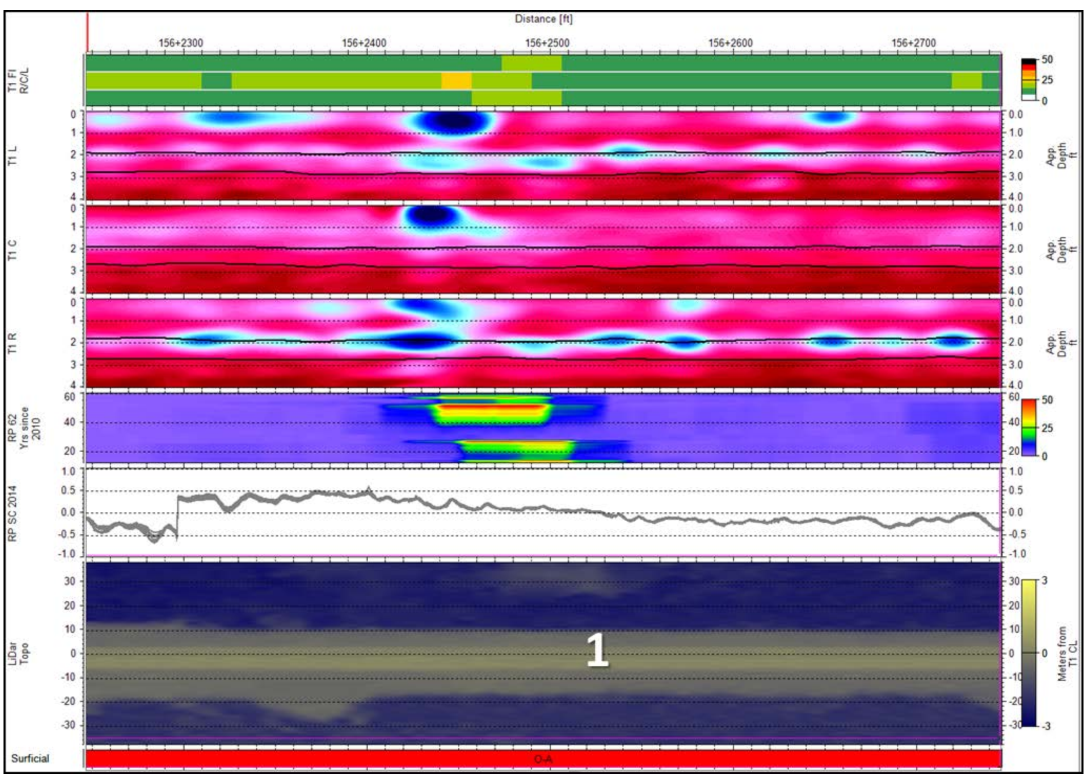

Figure 6. LIDAR, GPR, and Geometry Data at Kingston Site 1

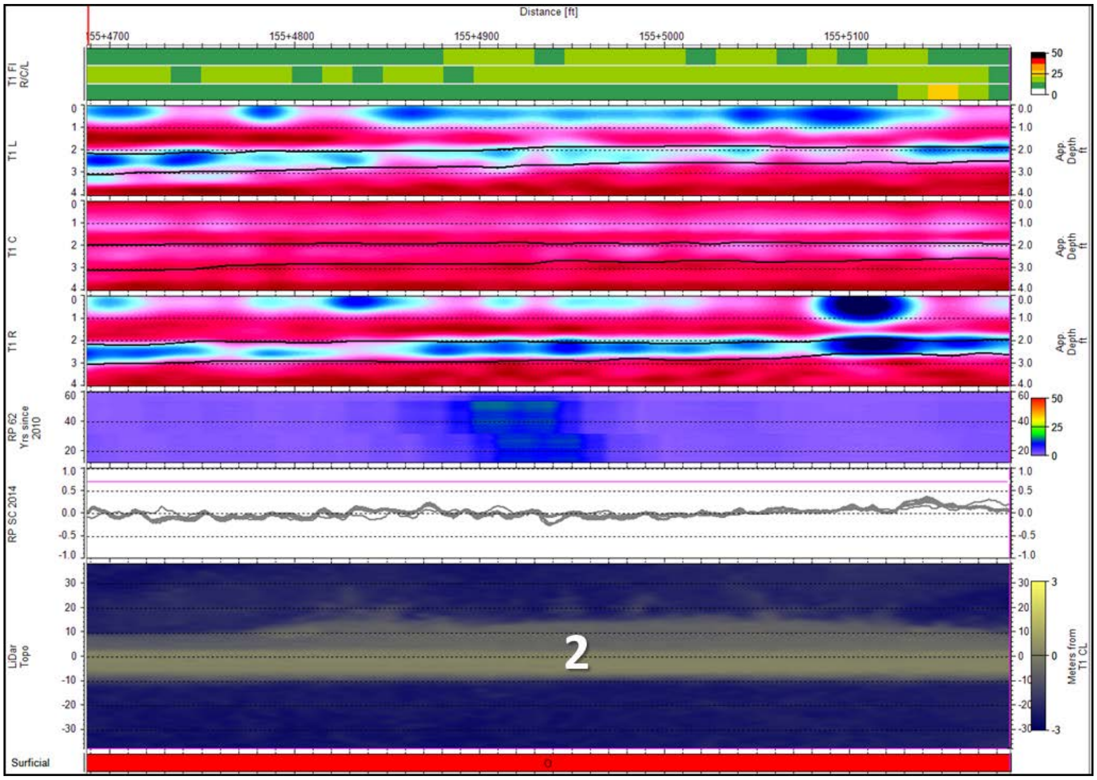

Figure 7. LIDAR, GPR, and Geometry Data at Kingston Site 2

Site 1 has a spot of slightly fouled ballast, roughness, and moisture near the area where measurements were taken. Moisture is present at the top layer of soil on the right (towards Track 2). Site 2 has mildly fouled ballast all around the site and moisture down to the second layer of both the left and right side of Track 1, and there is a spot of very mild roughness too. Both sites are in a fill, over several hundred feet on each longitudinal side, which made these locations excellent places to perform field measurements.

2.3 Dynamic Cone Penetrometer

The DCP test was conducted at the track centerline, shoulder and swamp area of Track 1 at the both sites. The right side of Figure 8 (Track 2), which is omitted from the figure, was assumed to have subgrade stiffness properties that were symmetrical to the track shown (Track 1). The DCP results indicate the in-place relative density of the soil, which is used to estimate the subgrade stiffness. The DCP device uses an 8-kg hammer that drops 575 mm driving a 60 degree cone tip with 20 mm base diameter into the ground. Tests were performed at both sites whenever possible, though testing in the gage was only possible during overnight work. Samples were taken from the embankment at sites for visual identification and are shown on Figure 8. Figure 9 shows the DCP device being used along the edge of the embankment closest to the track. Figure 10, Figure 11, and Figure 12 show the DCP results in 2013, 2014, and 2015, respectively.

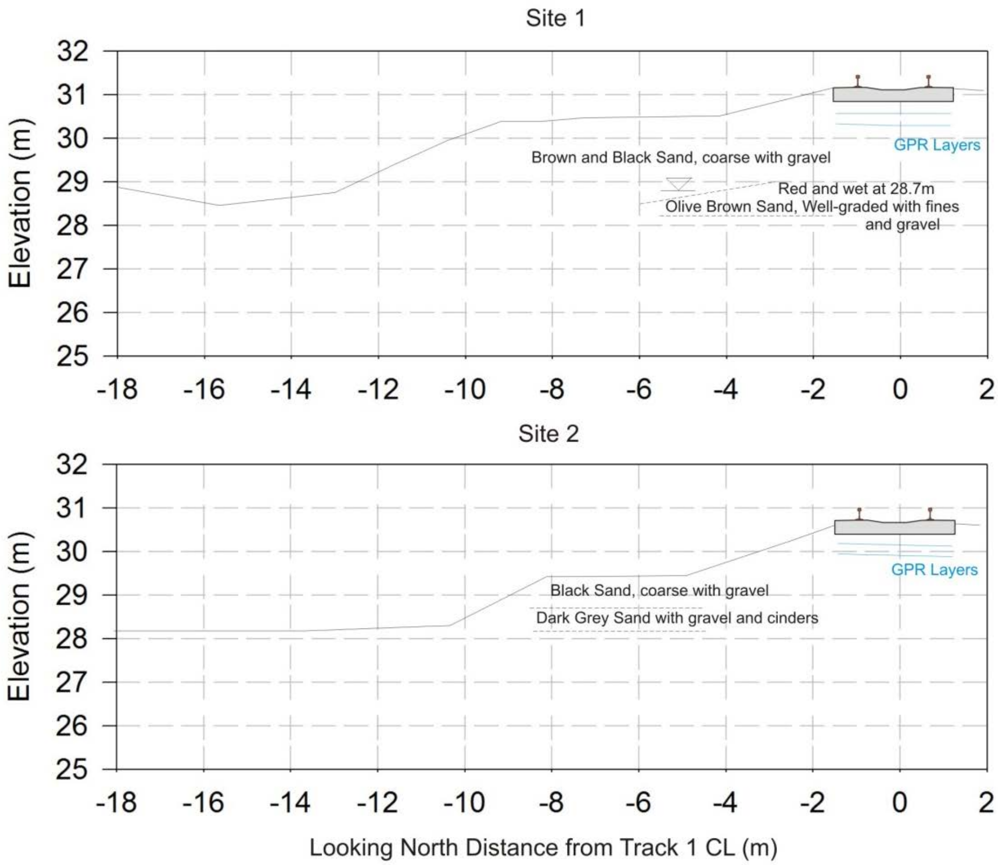

Figure 8. Cross Sections of Sites 1 and 2 with Sampling Layers

Figure 9. DCP Device

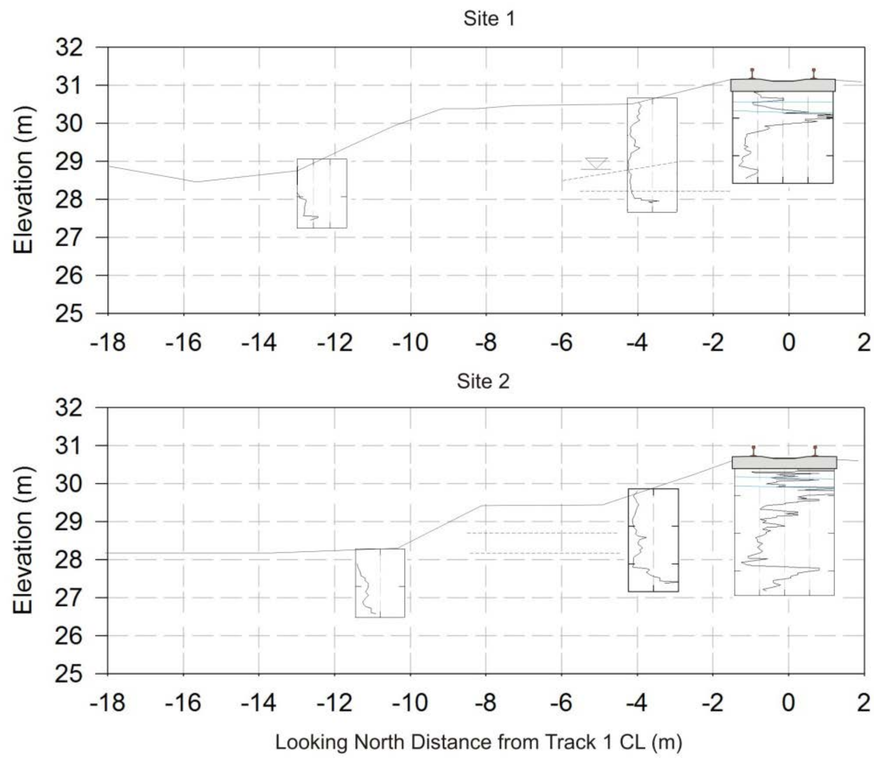

Figure 10. DCP Results in 2013

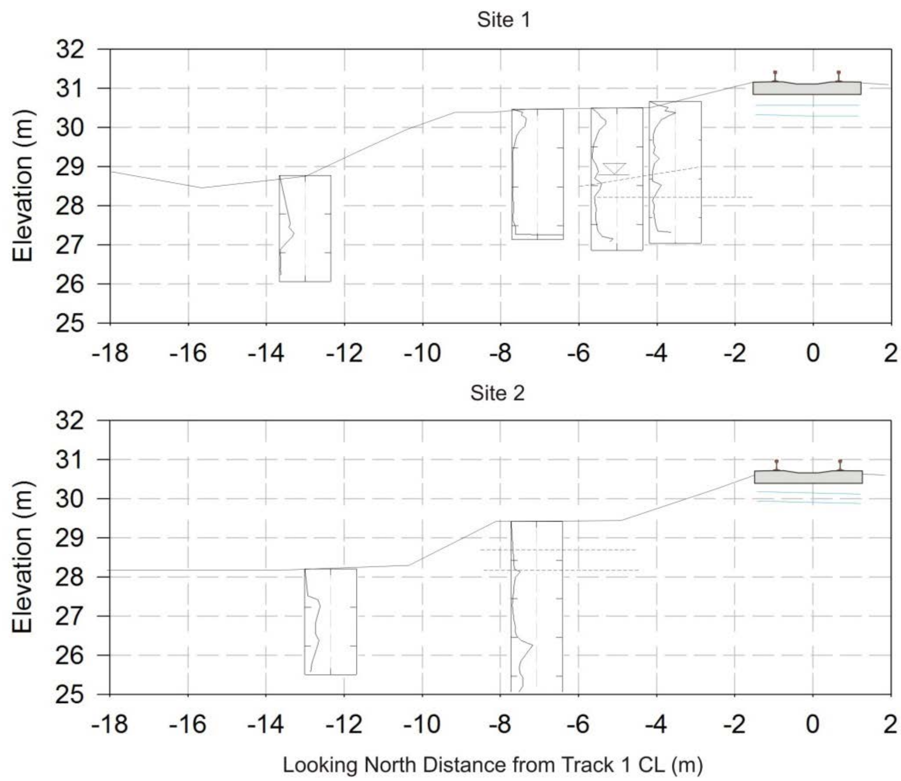

Figure 11. DCP Results in 2014

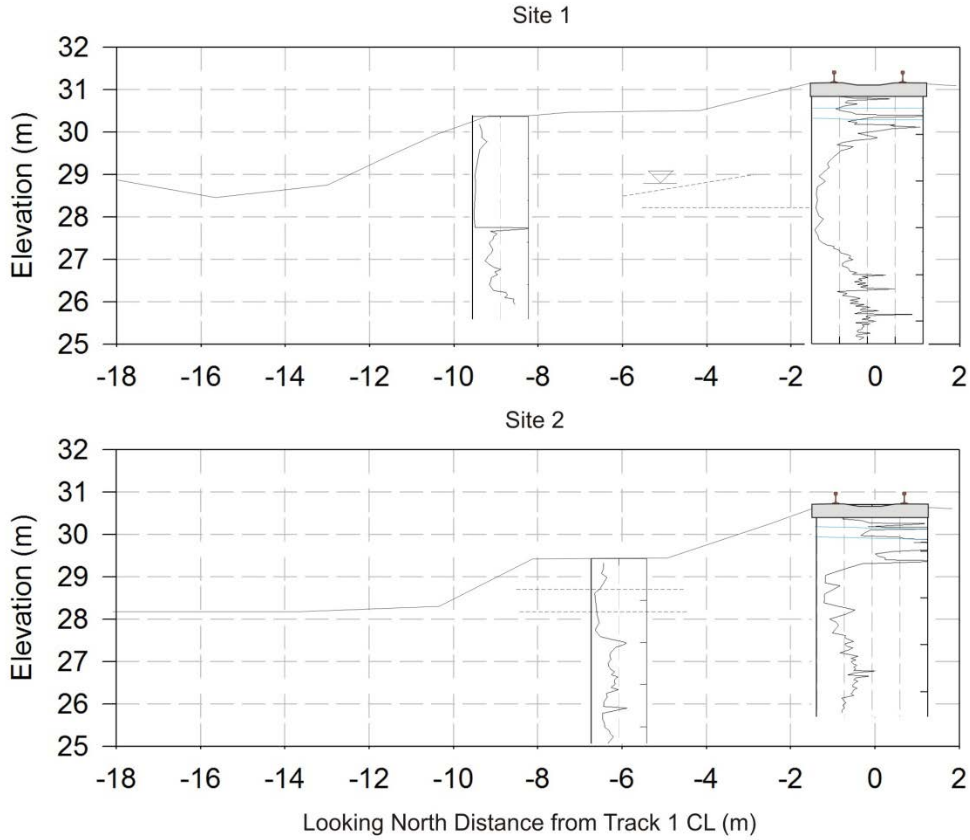

Figure 12. DCP Results in 2015

The stiffness of the ballast and subgrade are calculated using the DCP data. The stiffness ranges at each depth are listed in Table 1. The values have a wide range because the data were collected in different seasons and conditions. The model considered stiffness values from the DCP values collected on that date, or closest to it.

The modulus of the soil can be estimated using the following equations (DeBeer, 1992):

$$E_{DPI} = 10^{3.04758-[1.06166 \log(DPI)]} \tag{1}$$

Where: E_{DPI} = modulus (MPa)

DPI = DCP penetration index (mm/drop)

Equation 1 is for standard DCP equipment only which was used for the Kingston site testing (drop height of 575 mm and a hammer mass of 8 kg).

Table 1. Track and Subgrade Stiffness

Site 1

Centerline		**Embankment**		**Swamp**	
Depth(m)	**E(MPa)**	**Depth(m)**	**E(MPa)**	**Depth(m)**	**E(MPa)**
0-0.6	150-350	0-0.6	30-90	0-1	3-15
0.6-1.3	30-100	0.6-2.7	10-30	1.0-1.5	50-100
1.3-2.6	40-120	2.7-3.6	100-120	1.5-1.62	120-140

Site 2

Centerline		**Embankment**		**Swamp**	
Depth(m)	**E(MPa)**	**Depth(m)**	**E(MPa)**	**Depth(m)**	**E(MPa)**
0-1.1	200-350	0-2.0	30-90	0-0.7	10-20
1.1-2.8	150	2.0-2.5	150	0.7-2.7	50-100
2.8-3.5	70-120				

2.4 Spectral Analysis of Surface Wave

The SASW method is an in-situ seismic method for determining shear wave velocity profiles.[1] A dynamic impact generates surface waves, and those waves are monitored by two or more receivers at known offsets. Since testing is performed on the ground surface, the measurements are less costly than traditional borehole methods. Figure 13, and Figure 14 show an example of the SASW test, which plots wave traveling times versus the surface displacement. Different curves represent the signals received at different locations. The strongest response (usually the first downward peak) is the time point when the surface wave arrives. The surface wave velocity is determined by the time lag and length of offset, providing the modulus of soil (Table 2).

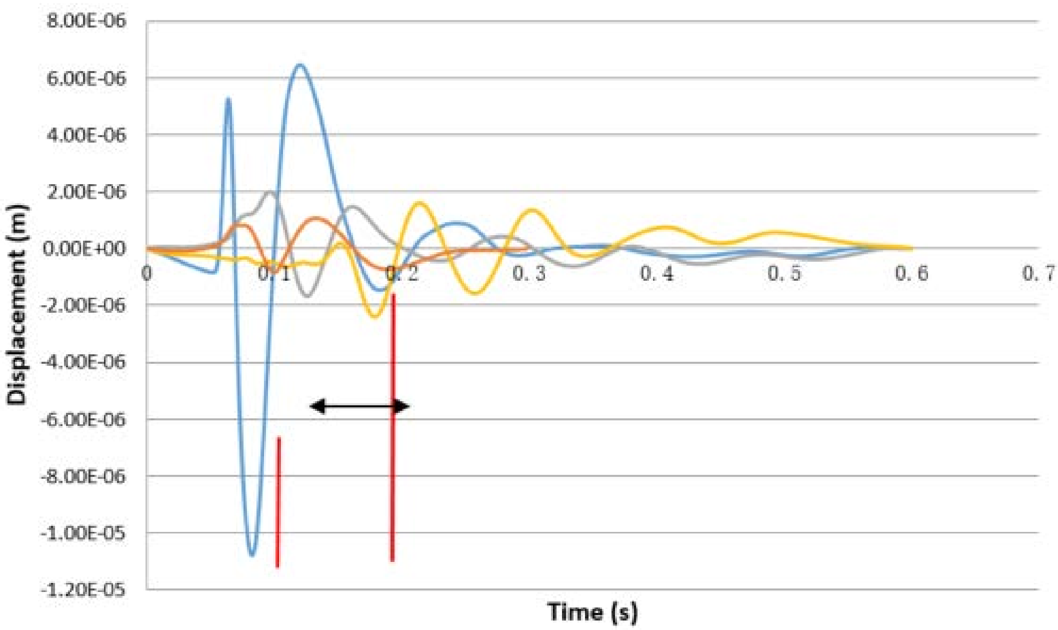

Figure 13. Spectral Analysis of Surface Wave for the Great Swamp at Site 1

---

[1] http://www.geovision.com/PDF/M_SASW.PDF

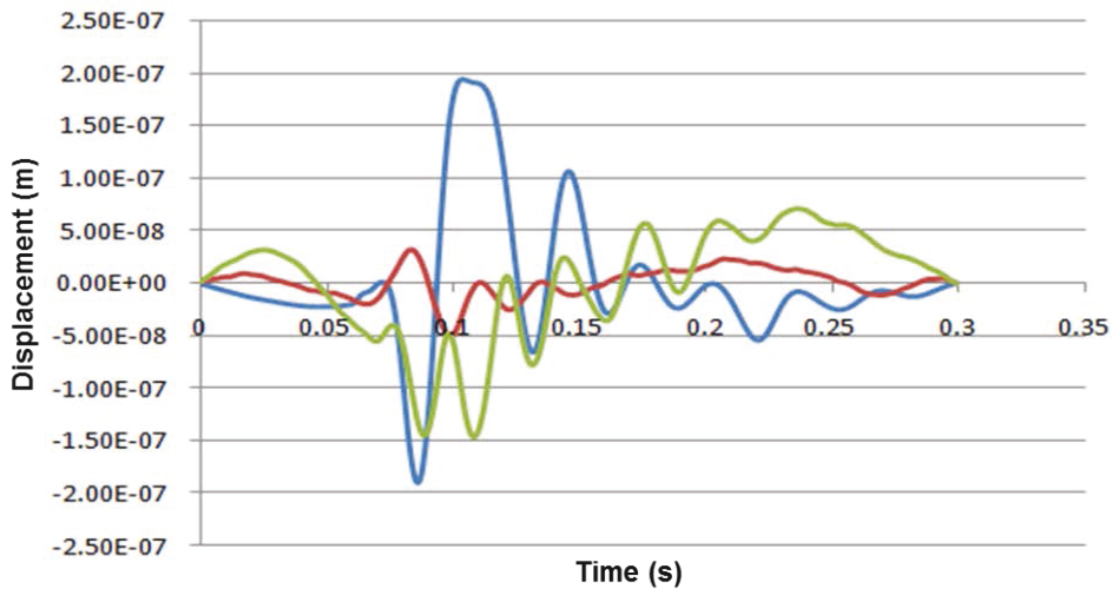

Figure 14. Spectral Analysis of Surface Wave for the Great Swamp at Site 2

Table 2. Subgrade Stiffness by Spectral Analysis of Surface Wave

Location	**Elastic Modulus (MPa)**	
	Site 1	**Site 2**
Embankment	42	56
Swamp	2.9	4

2.5 Laboratory Tests

Several samples from the top 0.3 m of the swamp were brought to the lab for tests. The water content was measured, while Torvane and fall cone tests were performed to calculate the shear strength. The shear wave velocity, which gives an estimate of the modulus of elasticity and the shear modulus, was measured in Bender elements. Table 3 gives the results of these tests.

Table 3. Laboratory Tests Results at Site 1 from Gnatek (2014)

Tube No.	Sample Depth	ρ	vs	Gmax	E	w	Su, TV	Su, FC
(-)	(m)	(g/cm3)	(m/s)	(kPa)	(kPa)	(%)	(kPa)	(kPa)
1-3	0.05-0.13	1.2	29.4	1037	3008	384	4	5.6
1-3	0.13-0.21	1.13	28.2	899	2606	204	5.7	6.2
1-3	0.21-0.29	1.02	21.5	471	1367	215	6.1	13.9
1-4	0.23-0.30	1.07	24.2	627	1817	405	4.2	7.1
1-5	0.08-0.15	1.42	27.7	1090	3160	70	5.6	9.2
1-5	0.18-0.25	1.3	24.4	774	2245	161	4.9	4.8
1-6	0.08-0.15	1.23	31.7	1236	3584	131	5.7	14.5
1-6	0.15-0.23	1.06	25.1	668	1937	376	5.2	11.4
1-6	0.23-0.30	1.06	17.1	310	899	487	4.4	11.9

2.6 Field Instrumentation

To quantify the track performance at the Kingston site, a 3 × 3 array of piezoelectric, triaxial accelerometers were temporarily installed along the track and right of way with a general longitudinal spacing of 25 tie spaces (15 m) and a general lateral spacing of 7.5 m. Steel mounting plates were machined and attached to the concrete ties using an epoxy adhesive (Figure 15). Schematic drawings of the plates are in the appendix. The mounting plates were machined with a bevel to accommodate the geometry of the tie and create a horizontal surface which allows the accelerometers to be level. The six accelerometers installed in the soil adjacent to the track were mounted on insertion spikes, and pushed into the embankment and swamp to a depth of 6 inches. The installation methods were designed to permit rapid installation and removal so that the accelerometer network could be installed at multiple sites along the track.

Each accelerometer recorded the accelerations in three directions: vertical, longitudinal, and lateral. The sampling was conducted at a rate of 1000 Hz. The accelerometer data were recorded using conventional amplification, signal conditioning, and data acquisition. 500 Hz low-pass passive filters were used to eliminate aliasing effects. Figure 16 and Figure 17 show the general plan and cross sectional view of instrumentation. The actual plan in the field may change a bit due to different topographies. (See Appendix A)

Figure 15. Installation of Accelerometers on Concrete Tie (left) and in the Swamp Deposit (right)

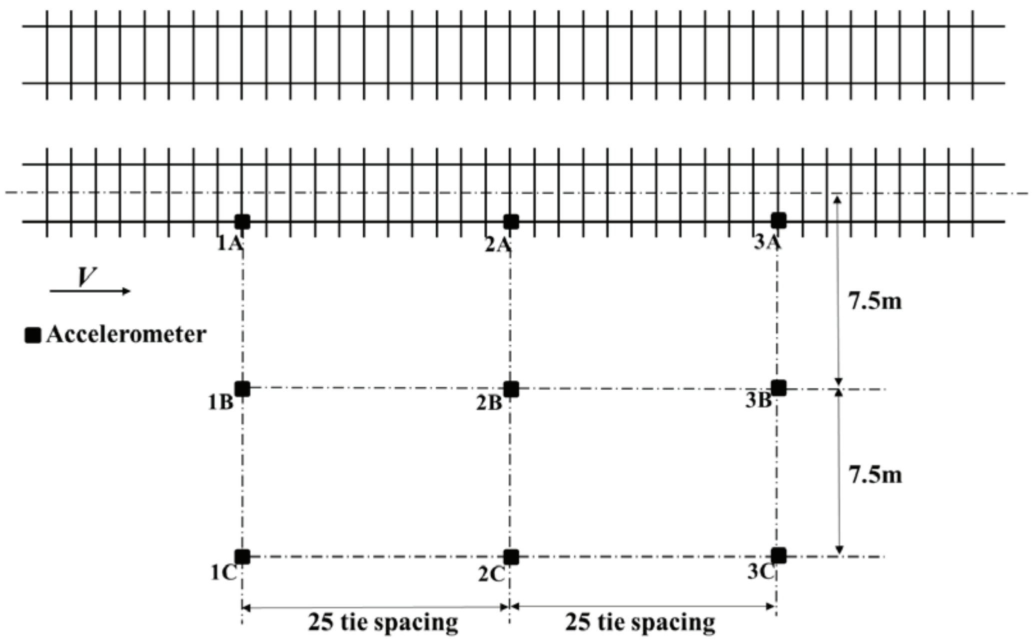

Figure 16. Plan View of Instrumentation

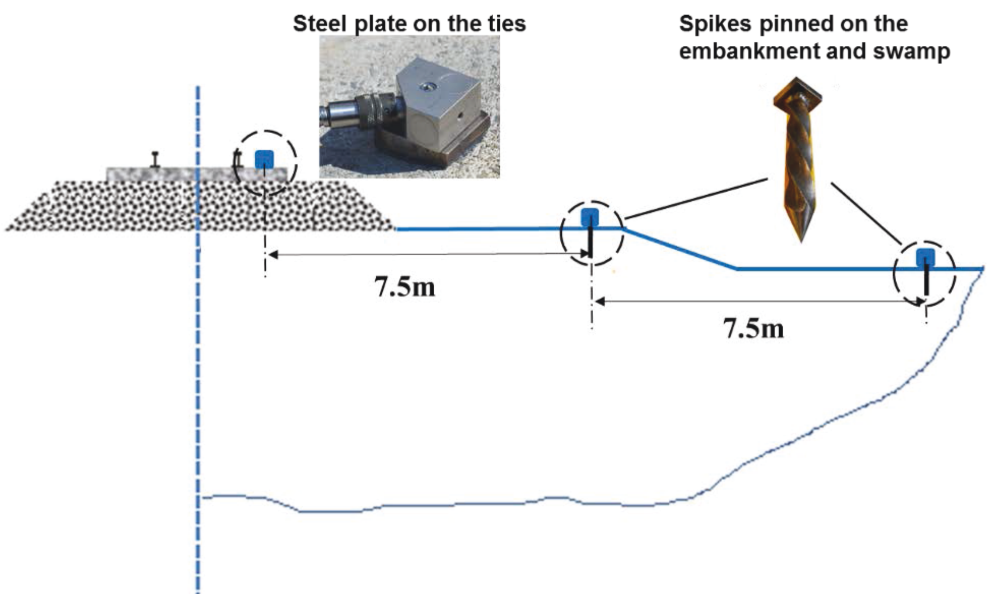

Figure 17. Cross Sectional View of Instrumentation

2.6.1 Data Collection and Interpretation

The site's track and the ground vibration caused by passing trains in the Great Swamp area were measured at different vehicle speeds during different times of the year. Figure 18 presents the vertical acceleration versus time for the tie-mounted and ground-pinned accelerometers and for an Acela train traveling at 193 km/hr. The train was traveling in the southwest direction on Track 1, as indicated by the delay in wave motion arrival times.

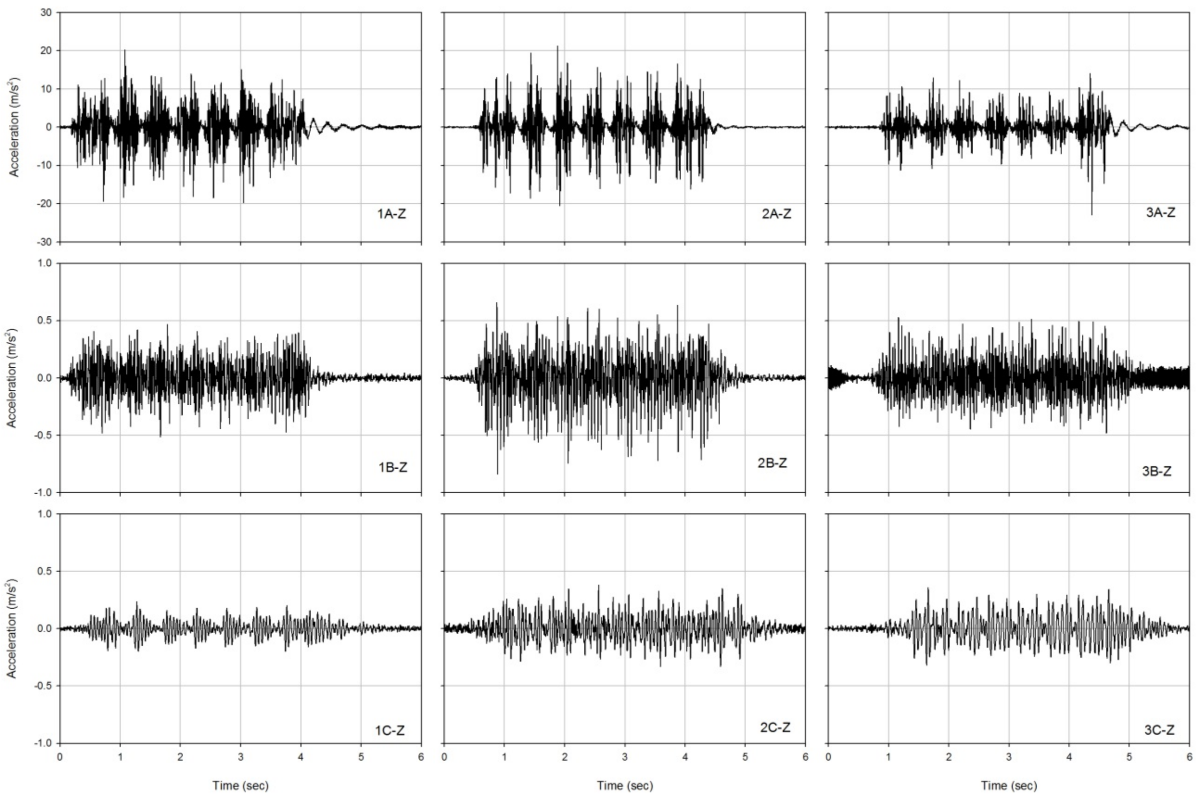

Figure 18. Vertical Acceleration Time Histories for the Passage of an Acela Express Traveling at 193 km/hr, Recorded on November 18, 2013, at 12:49 pm at Site 1 (Gnatek, 2014)

Figure 19 presents the calculated displacement versus time. Each downward peak presents a wheel load of the end locomotives and six passenger cars. The downward displacement for locomotives are larger than passenger cars which means that the locomotives are heavier. The locomotive bogie spacing is shorter than that of passenger cars which is also indicated clearly by the plot.

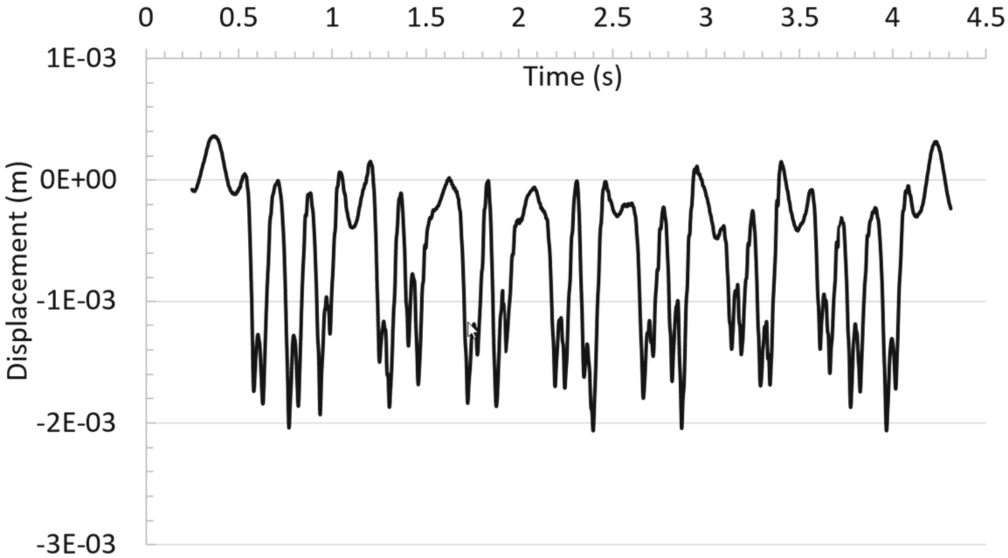

Figure 19. Vertical Displacement Calculation of Tie for an Acela Express Traveling at 193 km/hr, Recorded on November 18, 2013, at 12:49 pm at Site 1

In addition, Figure 20 shows the contour that represents the wave front arrival times in seconds relative to the arrival of the first axle at Accelerometer 1A for an Acela train traveling at 193 km/hr. The forward bend in the wave propagation near the track could result from that the shear wave velocity of the embankment soil exceeding the train speed. However, when the wave propagates to the area about 5 m away from the track centerline to the swamp, the shear wave velocity significantly reduces and wave movement lags behind the train. The cone-shaped wave motion is seen, so the test site at Kingston may have a slight critical speed effect in this test. Figure 21 shows a figure of Regional train at 125 km/hr. As can be seen, the cone-shaped ground wave motion exists, but is attenuated at the lower speeds.

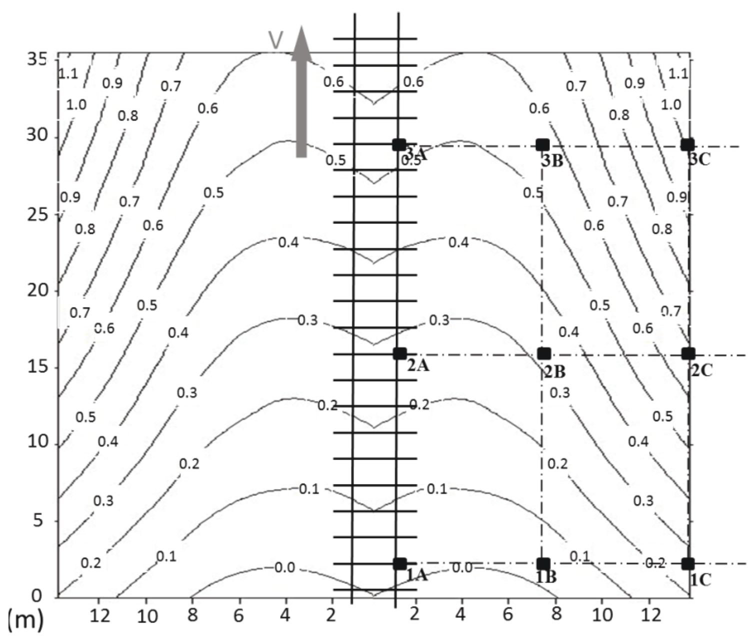

Figure 20. Ground Surface Wave Motion of Acela at 193 km/h

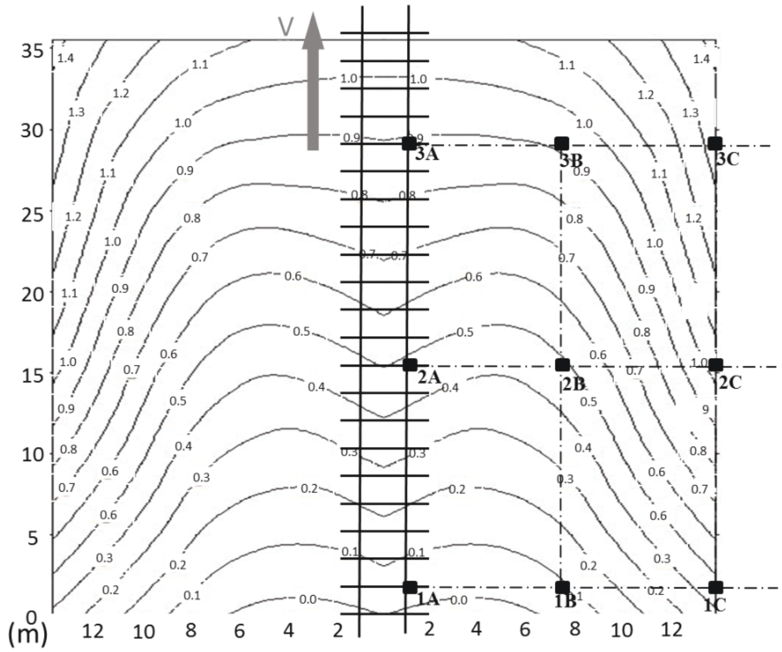

Figure 21. Ground Surface Wave Motion of Regional at 125 km/hr

2.7 Train Information

A high-speed video camera and a photo-electric sensor recorded passing trains to obtain an accurate measure of train speed, so the exact location of the train could be reconciled with the acceleration time histories. The information for each train passage is listed in Table 4.

Table 4. Log of Trains for Which Track and Ground Response were Measured

Date	Time	Location	Velocity (km/hr)	Type
11/18/2013	10:50	Site 1	126.7	Regional
11/18/2013	12:13	Site 1	234.4	Acela
11/18/2013	12:21	Site 1	119.2	Regional
11/18/2013	12:49	Site 1	193.0	Acela
11/18/2013	14:10	Site 2	204.5	Acela
11/18/2013	14:43	Site 2	142.2	Regional
11/18/2013	16:01	Site 2	224.6	Acela
11/18/2013	16:19	Site 2	146.2	Regional
12/19/2013	10:11	Site 1	204.1	Acela
12/19/2013	11:14	Site 1	115.6	Regional
12/19/2013	12:10	Site 1	223.6	Acela
12/19/2013	12:24	Site 1	123.8	Regional
12/19/2013	13:10	Site 1	224.6	Acela
12/19/2013	14:07	Site 1	239.4	Acela
3/18/2014	12:11	Site 1	194.4	Acela
3/18/2014	12:22	Site 1	127.8	Regional
3/18/2014	13:06	Site 1	245.5	Acela

3/18/2014	14:06	Site 1	223.6	Acela
4/9/2014	12:08	Site 1	213.8	Acela
4/9/2014	12:20	Site 1	151.6	Regional
4/9/2014	13:07	Site 1	191.9	Acela
4/9/2014	14:07	Site 1	232.6	Acela
4/10/2014	9:42	Site 2	33.1	Acela
4/10/2014	10:10	Site 2	43.6	Acela
4/10/2014	10:44	Site 2	92.9	Regional
4/10/2014	12:09	Site 2	194.4	Acela
4/10/2014	12:20	Site 2	149.4	Regional
4/10/2014	13:07	Site 2	199.1	Acela
4/10/2014	14:05	Site 2	236.5	Acela
9/27/2014	2:04	Site 2	222.5	Acela
9/27/2014	2:50	Site 2	182.9	Acela
9/27/2014	3:27	Site 2	226.4	Acela
6/10/2015	9:19	Site 2	148.3	Regional
6/10/2015	10:22	Site 2	218.2	Acela
6/10/2015	12.21	Site 2	234.7	Acela
6/10/2015	14:02	Site 2	120.2	Regional

2.7.1 Tested Vehicle Configuration

Figure 22 and Figure 23 show the Acela Express and Regional trainset configurations. The Acela Express has power cars on each end of six passenger cars. The Regional train uses a single locomotive trailed by seven passenger cars. Information regarding the axle loads for the Acela and Regional train set is listed in Table 5 and Table 6.

Table 5. Acela Express Train Set Information (Chrismer, 2014)]

Car Type	No. of Cars	Axles/Car	Car Length (m)	Inter-Bogie Spacing (m)	Inter-Axle Spacing (m)	Mass/Axle (kg)
Locomotive	2	4	21.219	10.744	2.849	23,175
First Class	2	4	26.645	18.136	2.997	16,150
Business Class	3	4	26.645	18.136	2.997	15,775
Café	1	4	26.645	18.136	2.997	15,525

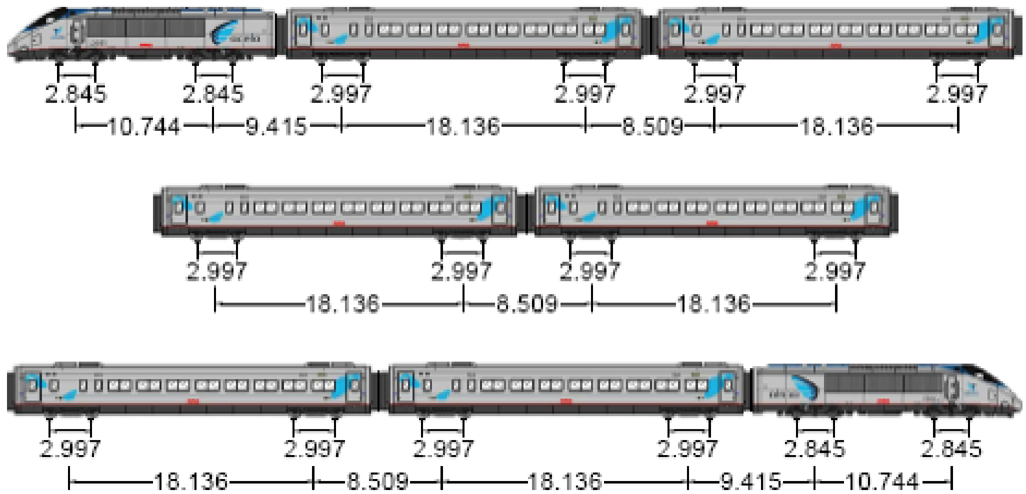

Figure 22. Acela Express Configuration (Dimensions in Meters, Courtesy of Amtrak, (Chrismer, 2014))

Table 6. Regional Train Set Information (Chrismer, 2014)]

Car Type	No. of Cars	Axles/Car	Car Length (m)	Inter-Bogie Spacing (m)	Inter-Axle Spacing (m)	Mass/Axle (kg)
Locomotive	1	4	15.692	7.799	2.943	22,908
Passenger	7 to 9	4	26.01	18.136	2.591	13,155
Café	1	4	26.01	18.136	2.591	12,475

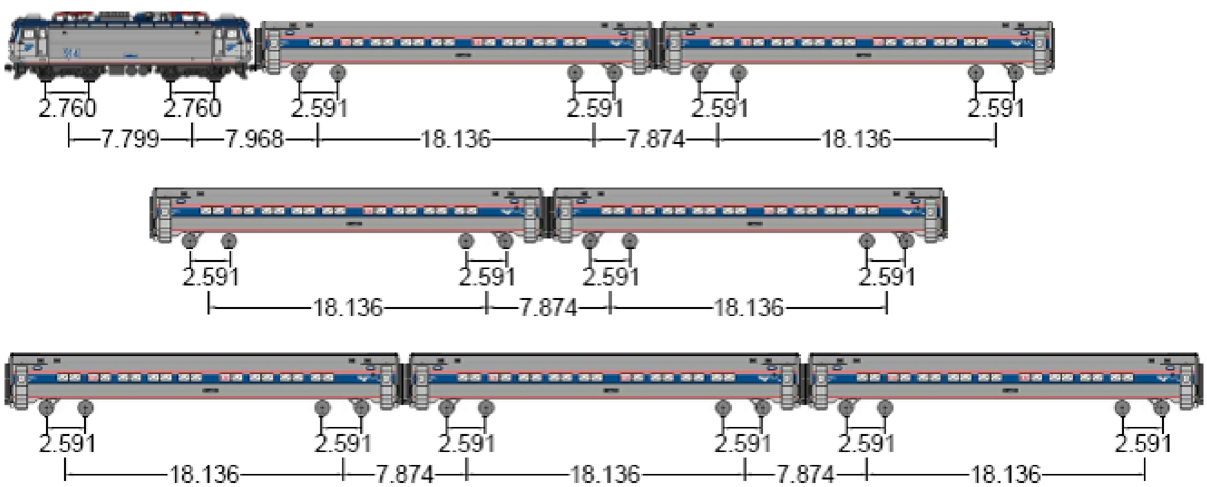

Figure 23. Regional Trainset Configuration (Dimensions in Meters, Courtesy of Amtrak, [Chrismer, 2014])

3. Validation of A Dynamic Track-Subgrade Interaction Model

The field investigation may not explain the frequent maintenance at Kingston and it cannot evaluate the speed effect on track performance comprehensively. The track performance out of the physical range cannot be measured. The modeling technique is the most effective and efficient tool for determining the critical speed at specific site. The authors modified and validated an existing track-subgrade interaction model, developed in the authors' previous research, to evaluate the speed effect at the Kingston site.

In the United States, most of the HSR are constructed on ballasted track, which includes tie, ballast and soil subgrade. A model is needed that accounts for rail surface irregularities, track cross-sectional irregularities, tie-ballast contact scenarios and soil subgrade. The train speed effect on track performance needs to be considered to ensure that deflections are not excessive, especially as train speed approaches the system's critical speed.

In this project, the team modified and validated a dynamic track-subgrade interaction model. The model predicts the tie-ballast responses, and the track and subgrade performance at different vehicle speeds. Figure 24 shows the conceptual dynamic track-subgrade interaction model. The model has three parts: discrete supports (including pad, tie, and ballast), rail beam, and 3D finite element domain for subgrade. For convenience, here they are individually analyzed and later assembled together. The model formulation was based on prior research.

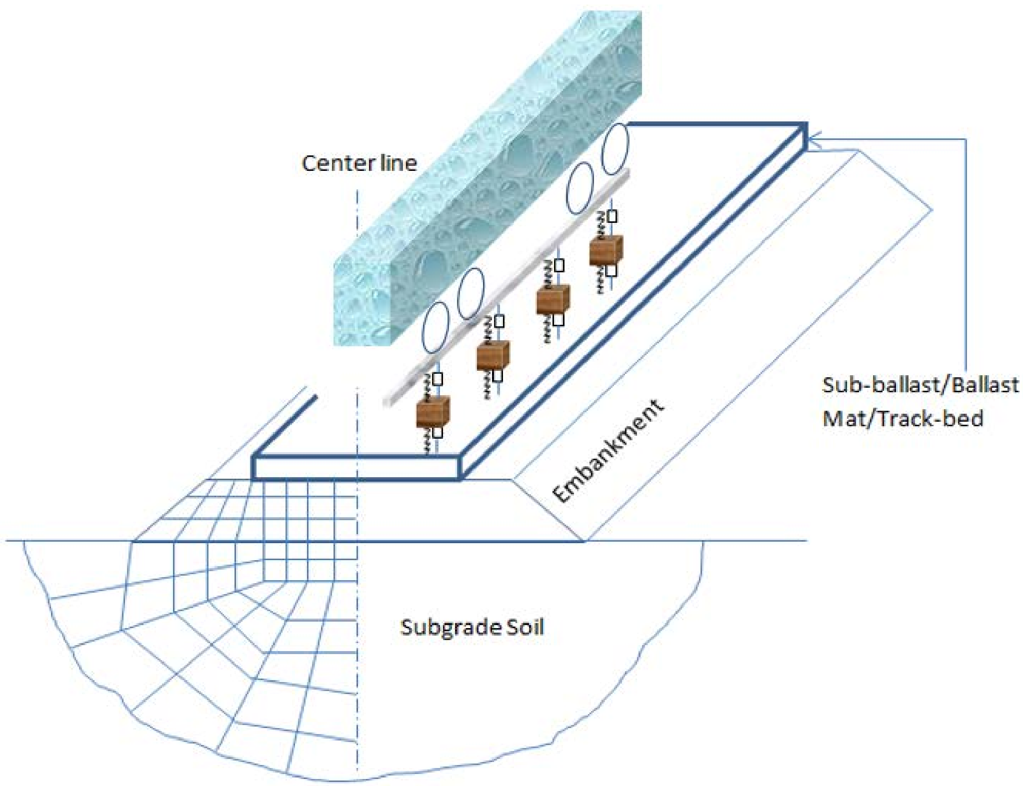

Figure 24. Conceptual Dynamic Track-Subgrade Interaction Model for US HSR

3.1 Modification of The Existing Track Model

The track components in Figure 24 are detailed in Figure 25 with symbols which will be described in a series of equations. The key idea is to merge the track model with the finite element formulation of subgrade, creating a "Sandwich" model.

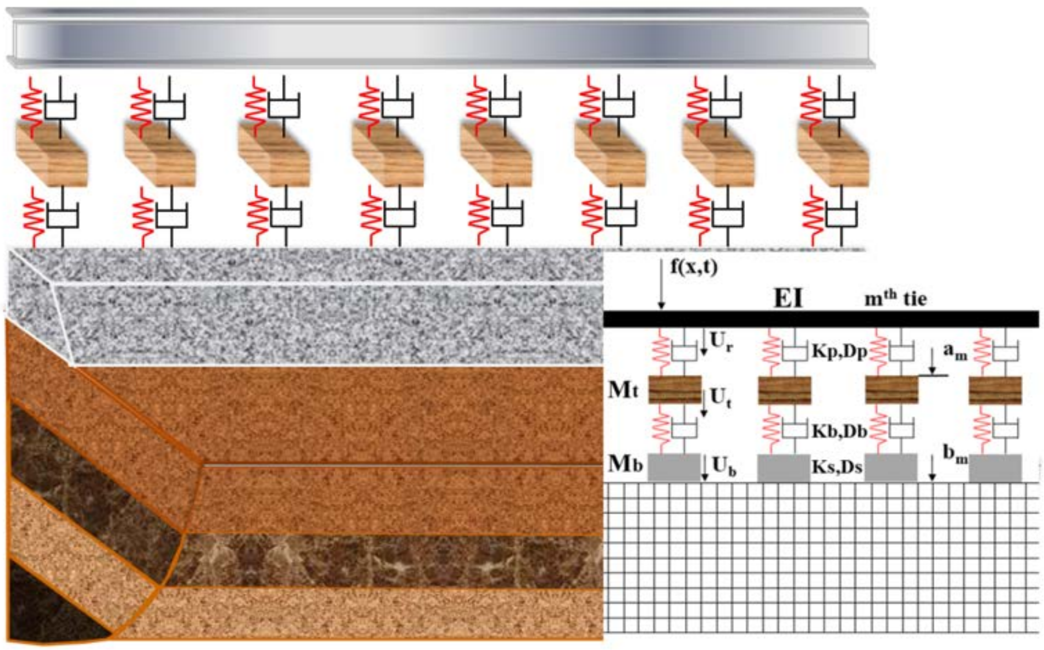

Figure 25. Sandwich Model

The dynamic responses of the moving train in this model can be calculated in three steps:

1. Generate the numerical stiffness (K) and damping (D) of the subgrade by finite element method (FEM).
2. Input the properties of subgrade into track model to get the responses of the track components.
3. Extract the soil displacement from the track model and put it back to the FEM model to get the subgrade responses. The formulation is shown below.

For the system, the point load f(x,t) is applied on top of the beam. For the point load, we have

$$f(x,t) = f(t)\delta(x - vt) \qquad (2)$$

Where, x: load position

t: time

v: train speed

The rail beam is modeled beginning with the governing equation given by Euler Beam Theory:

$$EI\frac{\partial^4 \mathrm{u}}{\partial \mathrm{x}^4} + M_r\frac{\partial^2 \mathrm{u}}{\partial \mathrm{t}^2} = f_{ext}(x,t) = \sum_{m=1}^{n} a_m(t)\delta(x - x_m) + f(t)\delta(x - vt) \qquad (3)$$

Where, a_m: tie force at x_m acting on the rail beam

f_{ext}: external load distribution

E: the modulus of elasticity

I: Bending moment of inertia

M_r: Mass of rail per unit length

u: rail beam deflection

v: train speed.

Force equilibrium and Newton's 2nd law are used in Equation 4 to 7 to give the tie force a_m on rail and ballast force b_m on the subgrade.

$$a_m = (U_r - U_t)K_p + (\dot{U}_r - \dot{U}_t)D_p \tag{4}$$

$$b_m = U_b K_s + \dot{U}_b D_s \tag{5}$$

$$M_t \ddot{U}_t = a_m - [(U_t - U_b)K_p + (\dot{U}_t - \dot{U}_b)D_p] \tag{6}$$

$$M_b \ddot{U}_b = (U_t - U_b)K_b + (\dot{U}_t - \dot{U}_b)D_b - (U_b K_s + \dot{U}_b D_s) \tag{7}$$

Where, U_r: rail deflection; U_t: tie deflection; U_b: ballast deflection;

K_p, K_b, K_s: stiffness of rail pad, ballast and subgrade

D_p, D_b, D_s: damping of rail pad, ballast and subgrade

Mt: mass of tie per unit length

Mb: mass of ballast per unit length

A complex Fourier transform is used to remove the time differentiation from Equations 4 through 7 and are given in Equations 8 through 11. The subscript 'w' means the calculation is transformed to frequency domain and 'i' symbols are imaginary numbers.

$$a_m(w) = [U_{r(w)} - U_{t(w)}](K_p + iwD_p) \tag{8}$$

$$b_m(w) = U_{b(w)}(K_s + iwD_s) \tag{9}$$

$$[U_{r(w)} - U_{t(w)}](K_p + iwD_p) - [U_{t(w)} - U_{b(w)}](K_b + iwD_b) = -w^2 U_{t(w)} M_t \tag{10}$$

$$[U_{t(w)} - U_{b(w)}](K_b + iwD_b) - U_{b(w)}(K_s + iwD_s) = -w^2 U_{b(w)} M_b \tag{11}$$

Where, w: wave number

The wave number is determined by the minimum wave length of the train induced vibrations. In order to solve U_t and U_b with respect to U_r, Equations 10 and 11 were rewritten.

$$(K_p + iwD_p)U_{r(w)} - [w^2 M_t - (K_p + iwD_p + K_b + iwD_b)]U_{t(w)} + U_{b(w)}(K_s + iwD_s) = 0 \tag{12}$$

$$(K_b + iwD_b)U_{t(w)} + [w^2 M_b - (K_b + iwD_b + K_s + iwD_s)]U_{b(w)} = 0 \tag{13}$$

In order to make Equations 12 and 13 simple and concise in the following expression, the two equations are rewritten below:

$$(DK_p)U_{r(w)} - (MT)U_{t(w)} + U_{b(w)}(DK_s) = 0 \tag{14}$$

$$(DK_b)U_{t(w)} + (MB)U_{b(w)} = 0 \tag{15}$$

Where, we set

$$DK_p = K_p + iwD_p;\ DK_b = K_b + iwD_b;\ DK_s = K_s + iwD_s$$

$$MT = w^2 M_t - DK_p - DK_b;\ MB = w^2 M_b - DK_b - DK_s$$

By solving U_t and U_b with respect to U_r, the tie force a_m on rail and ballast force b_m on the subgrade are written in the form below:

$$a_{m(w)} = DK_p(1 + DK_p / \Delta)U_{r(w)} \tag{16}$$

$$b_{m(w)} = (DK_s * DK_b * DK_p)U_{r(w)} / (MT * MB - DK_b^{\ 2}) \tag{17}$$

Where, $\Delta = (MT - DK_b^{\ 2} / MB)$

Equations 16 and 17 represent the forces between the tie and ballast, and the ballast and soil, respectively.

As we can see from Equation 16 and 17, the tie force a_m on rail and ballast force b_m are the functions of U_r. In order to solve U_r, recall the rail beam equation and transform it with respect to x and t,

$$(EIk^4 - M_r w^2 + \mathrm{i}kw)U_{r(k,w)} = \sum_{m=1}^{n} a_m(w)\mathrm{e}^{-\mathrm{i}x_m w} + f(w)(vk + w) \tag{18}$$

To solve the equation 18, the process is addressed in another author's publications (Huang, 2009, Gao, 2014). Once U_r is determined, the tie and ballast contact force and deflection can be calculated right after using Equation 16 and 17.

3.2 Expression of 3D Finite Element Subgrade

The subgrade is modeled by 3D FEM. Green's function is used to describe the subgrade. Figure 26 shows a unit point load running directly on top of the soil at a given speed (Dieterman, 1997). Because the subgrade shows different dynamic properties at different train speeds, soil stiffness should have different values under different speed conditions (which means that the soil stiffness will decrease when the train speed increases). The subgrade deflection will increase when the train speed increases. At a given speed, the reciprocal of soil deflection under a unit load is given by the Green function of subgrade at specific speed. The Fourier transform is performed in the direction of train moving direction, and the transverse and vertical directions were discretized by plane stress quadrilateral finite elements.

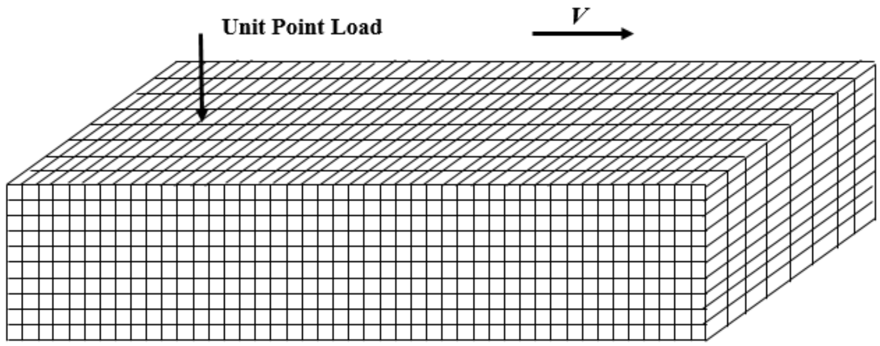

Figure 26. Schematic Plot for the Green's Function of Subgrade

The detailed derivation of the Green function begins with Equation 19. According to the stain-displacement relationship, the strain matrix is given by Equation 19 and the stress-displacement relationship gives the elastic matrix in Equation 20:

$$
[\mathbf{B}] = \begin{bmatrix} -i\lambda & 0 & 0 \\ 0 & \dfrac{\partial}{\partial \xi} & 0 \\ 0 & 0 & \dfrac{\partial}{\partial \eta} \\ \dfrac{\partial}{\partial \xi} & -i\lambda & 0 \\ 0 & \dfrac{\partial}{\partial \eta} & \dfrac{\partial}{\partial \xi} \\ \dfrac{\partial}{\partial \eta} & 0 & -i\lambda \end{bmatrix} \tag{19}
$$

$$
[\mathbf{C}] = \begin{bmatrix} C_{11} & C_{12} & C_{13} & 0 & 0 & 0 \\ & C_{22} & C_{23} & 0 & 0 & 0 \\ & & C_{33} & 0 & 0 & 0 \\ & & & C_{44} & 0 & 0 \\ & sym & & & C_{55} & 0 \\ & & & & & C_{66} \end{bmatrix} \tag{20}
$$

Where,

$C_{11} = E_1 \left(1 - \nu_{23}\nu_{32}\right)\gamma \qquad C_{22} = E_2 \left(1 - \nu_{13}\nu_{31}\right)\gamma \qquad C_{33} = E_3 \left(1 - \nu_{12}\nu_{21}\right)\gamma$

$C_{12} = E_1 \left(\nu_{21} - \nu_{31}\nu_{23}\right)\gamma = E_2 \left(\nu_{12} - \nu_{32}\nu_{13}\right)\gamma$

$C_{13} = E_1 \left(\nu_{31} - \nu_{21}\nu_{32}\right)\gamma = E_3 \left(\nu_{13} - \nu_{12}\nu_{23}\right)\gamma$

$C_{23} = E_2 \left(\nu_{32} - \nu_{12}\nu_{31}\right)\gamma = E_3 \left(\nu_{23} - \nu_{21}\nu_{13}\right)\gamma$

$$C_{44} = \mu_{23} \qquad C_{55} = \mu_{13} \qquad C_{66} = \mu_{12}$$

$$\gamma = \frac{1}{1 - \nu_{12}\nu_{21} - \nu_{23}\nu_{32} - \nu_{31}\nu_{13} - 2\nu_{21}\nu_{32}\nu_{13}}$$

$$\mu_{23} = E_3 / \left[2 \times (1 + \nu_{32})\right] \qquad \mu_{13} = E_1 / \left[2 \times (1 + \nu_{31})\right] \qquad \mu_{12} = E_2 / \left[2 \times (1 + \nu_{21})\right]$$

Where, ν is the Poisson's ratio and μ is the shear modulus of subgrade.

The adopted shape function is presented:

$$\mathbf{[N]} = \begin{bmatrix} N_1 & 0 & 0 & N_2 & 0 & 0 & N_3 & 0 & 0 & N_4 & 0 & 0 \\ 0 & N_1 & 0 & 0 & N_2 & 0 & 0 & N_3 & 0 & 0 & N_4 & 0 \\ 0 & 0 & N_1 & 0 & 0 & N_2 & 0 & 0 & N_3 & 0 & 0 & N_4 \end{bmatrix} \tag{21}$$

Where N_1, N_2, N_3, N_4 are parameters based on quadrilateral elements described by Equation 22.

$$N_i\left(\xi, \eta\right) = \frac{1}{4}(1 + \xi\xi_i)(1 + \eta\eta_i) \tag{22}$$

Where, i=1,2,3,4,

ξ, η are variables in the local coordinate system

$$N_1 = \frac{1}{4}(1-\xi)(1-\eta) \quad N_2 = \frac{1}{4}(1+\xi)(1-\eta) \quad N_3 = \frac{1}{4}(1+\xi)(1+\eta) \quad N_4 = \frac{1}{4}(1-\xi)(1+\eta)$$

Equations 19 and 20 combine with Equations 21 and 22 to provide the mass matrix (M) and stiffness matrix (K), as shown in Equations 22 and 23.

Mass matrix:

$$\mathbf{[M]} = \sum_e \rho \int_{-1}^{1}\int_{-1}^{1} \mathbf{N}^T \mathbf{N} \,|\, \mathbf{J} \,|\, d\xi d\eta \tag{23}$$

Stiffness matrix:

$$\mathbf{[K]} = \sum_e \int_{-1}^{1}\int_{-1}^{1} \left(\mathbf{B}^* \mathbf{N}\right)^{\mathsf{T}} \mathbf{C}\left(\mathbf{BN}\right) | \mathbf{J} | \, d\xi d\eta \tag{24}$$

where, 'e' represents element-wise integration.

The equivalent nodal force vector is given in Equation 25.

$$\mathbf{[F^{xt}]} = \sum_e \int_{-1}^{1}\int_{-1}^{1} \mathbf{N}^{\mathsf{T}} \mathbf{f} \,|\, \mathbf{J} | \, d\eta d\zeta \tag{25}$$

Equation 26 gives the expression of Jacobian Matrix [J].

$$[\mathbf{J}] = \begin{bmatrix} \sum_{i=1}^{4} \frac{\partial N_i}{\partial \xi} y_i & \sum_{i=1}^{4} \frac{\partial N_i}{\partial \xi} z_i \\ \sum_{i=1}^{4} \frac{\partial N_i}{\partial \eta} y_i & \sum_{i=1}^{4} \frac{\partial N_i}{\partial \eta} z_i \end{bmatrix} \tag{26}$$

The corresponding determinant, |J|=det[J].

Equation 27 is obtained from the derived equations above, and is used to calculate the ground surface displacement.

$$([\mathrm{K}] - (\omega - \lambda v)^2 * [\mathrm{M}]) * [\,\overline{\mathrm{dS}}\,] = [\bar{\mathrm{F}}] \tag{27}$$

The 3D finite element subgrade has two major advantages that enable it to simulate different tracks accurately. The first advantage is that the model can account for profile changes in the track cross section. Therefore, it is possible to simulate any landforms, such as a tunnel or slope (see Figure 27). The cross section is modeled by solid elements with 3D motions. Then, in the longitudinal direction, the domain is expanded by wavenumber through Fourier transform in a two-dimensional domain as the track cross section change is considered in the model.

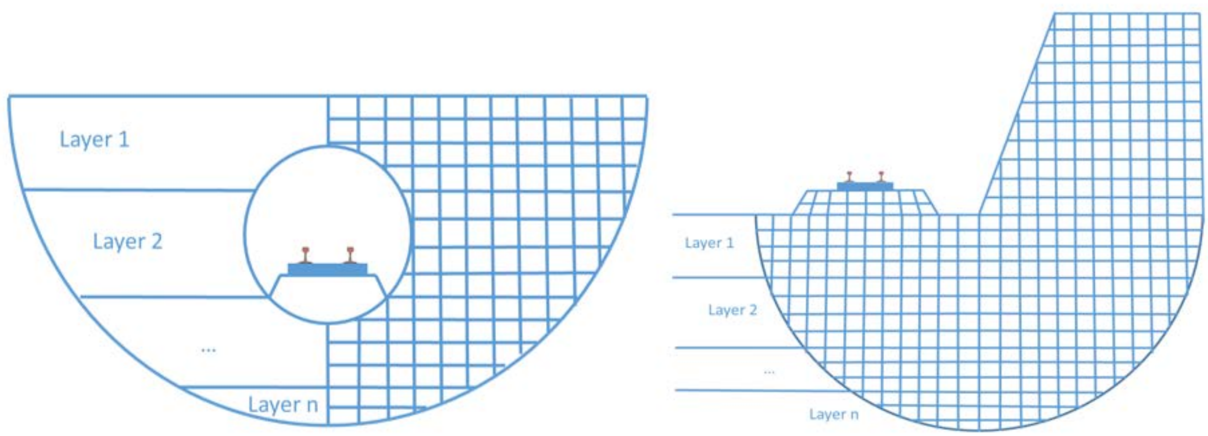

Figure 27. Different Profiles of Track Cross Section

The second advantage is that the 3D subgrade arrangement can of model the dynamic amplification of the soil. As the speed increases, the soil deflection will increase (Dieterman, 1997) (Dieterman, 1997). Therefore, the soil stiffness decreases when the train speed increases. As a result, the stiffness and damping of the soil have to be obtained by a numerical method. To obtain the soil properties, a unit load has been applied on top of the subgrade to generate the numerical stiffness and damping of the subgrade at different speeds. The values of the numerical stiffness and damping of the subgrade has been shown as a complex modulus (“H_s”) for the subgrade at different train speeds. “Hs” has different values when the speed of train changes. This is the Green’s function of subgrade used to account for the train speed effect. The real part of “Hs” is the value of stiffness (Ks) of the subgrade. The imaginary part of “Hs” is the damping ratio (Ds) of the subgrade.

3.3 Model Sensitivity Analysis

To show how sensitive the subgrade performance is to the speed of the train, the team performed a model sensitivity analysis. The key parameters of track components and subgrade in the model are listed in Table 7.

Table 7. Key Parameters Considered in the Proposed Model

Parameter	**Unit**
Train Load (f)	(kg)
Speed (v)	(km/hr)
Rail Mass per Unit Length (Mr)	(kg/m)
Moment of Inertia of Rail (I)	(m^4)
Tie Mass (Mt)	(kg)
Pad Stiffness (Kp)	(MN/m)
Pad Damping (Dp)	(MN*sec/m)
Ballast Stiffness (Kb)	(MN/m)
Ballast Damping (Db)	(MN*sec/m)
Subgrade Density	(kg/m^3)
Subgrade Modulus	(MN/m^2)
Subgrade Poisson's Ratio	N/A

Figure 28(a) shows that at low train speeds (v = 18 km/hr), the ground surface deflection is symmetrical to the track. The displacement field moves with the train (at position 0 in Figure 28), with a displacement pattern that resembles the static response of track under static train loading. As the train speed increases to 290 km/hr, the displacement field propagates to the surrounding area. When the train speed reaches critical speed, which is 300 km/hr in this example, both the influence area and the mode of the vibrations become fully cone-shaped responses. The area of the influenced region is much larger than that for the low speed condition. The soil response deviates from the static condition and has a cone-shaped displacement field.

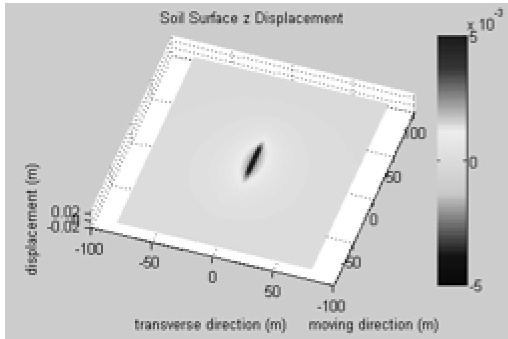

(a) v = 18 km/hr

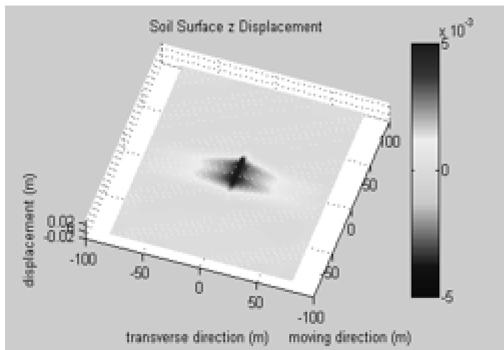

(b) v = 290 km/hr

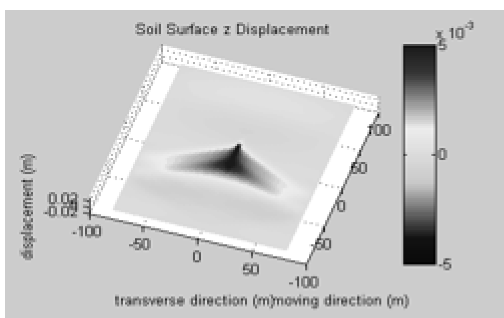

(c) v = 300 km/hr

Figure 28. Contour of Soil Surface Vertical Displacement Under Different Train Speeds

The results of rail surface vertical displacement, as varied with train velocities, are plotted in Figure 29. When a train is running at relatively lower speeds (5, 10, 20, 30, 40, 50, 60 and 70 m/s), the displacements of both the soil and rail surface change slightly. However, as train speed increases, vertical displacement rises exponentially. The results show that the track vibration level will grow to a theoretically infinite value when the train runs at critical speed.

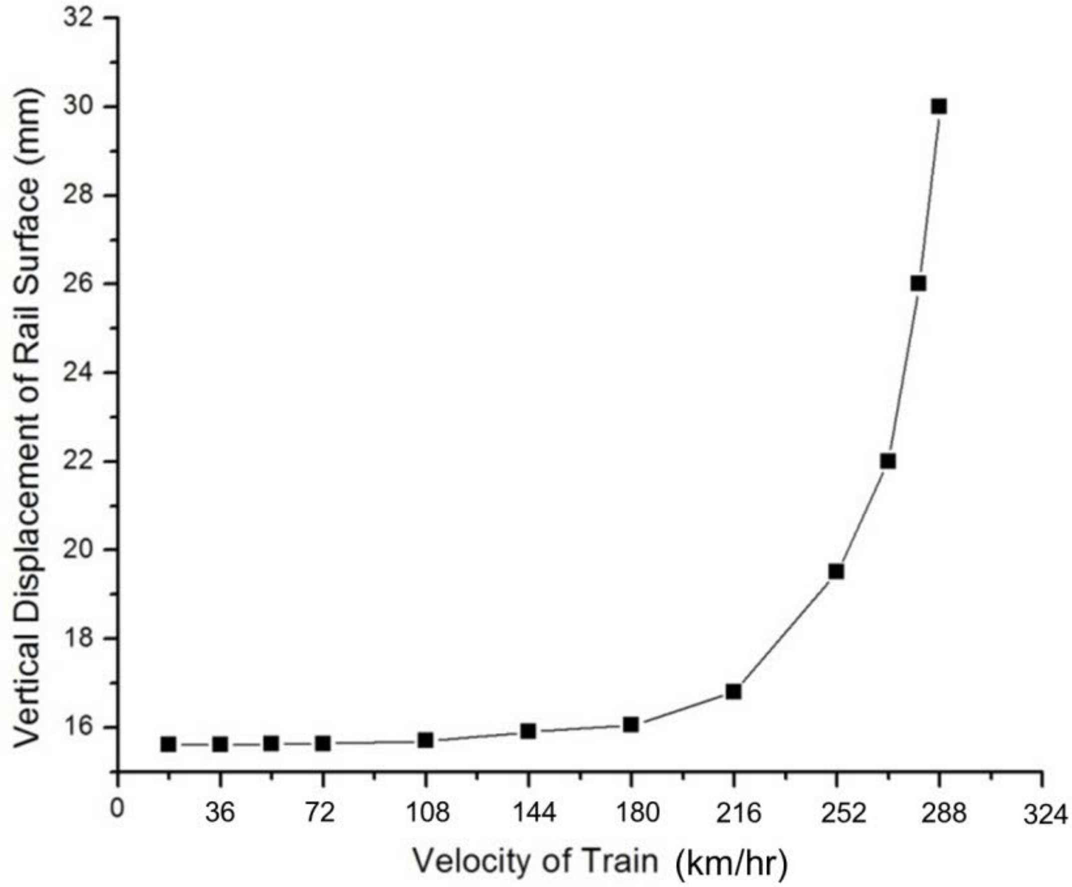

Figure 29. Maximum Modeled Rail Surface Vertical Displacement vs Velocity

3.4 Field Validation

Figure 30 shows the match of rail deflection between the field tests and model simulation for three different Acela Trains at different speeds. In the simulation, the maximum track deflections with train speeds of 193 km/hr, 222 km/hr and 240 km/hr are 2.3 mm, 2.4 mm and 2.8 mm, respectively. The maximum track deflections in field test are 2.2 mm, 2.3 mm and 2.7 mm respectively. The field data match the model very well throughout each test. Figure 31 shows the match of rail deflection for regional train running at 125 km/hr.

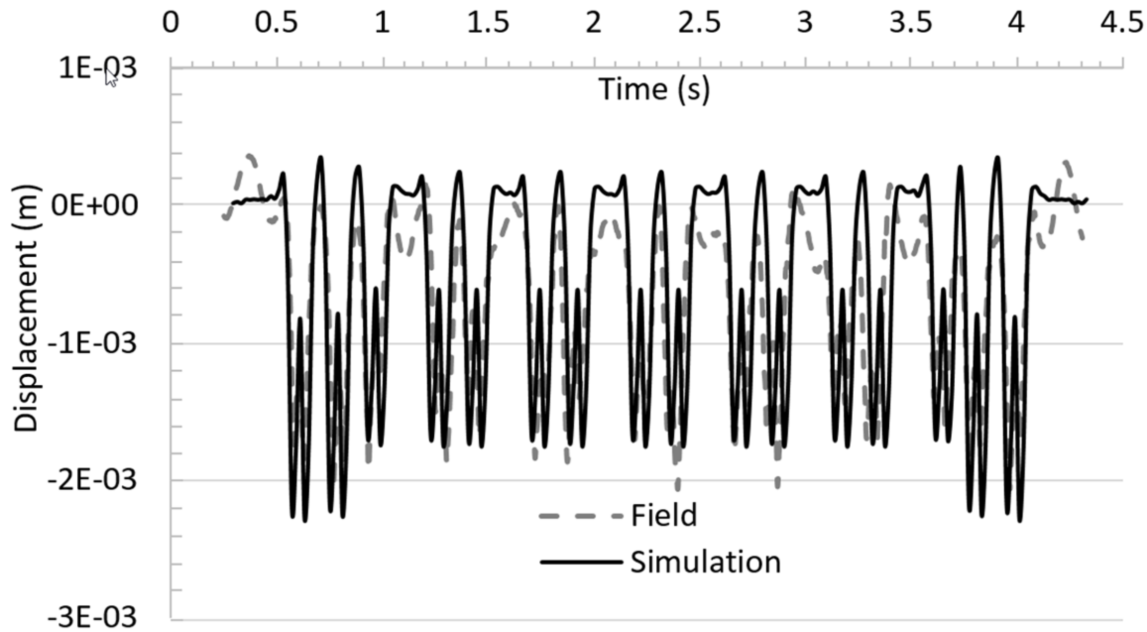

(a) v = 193 km/hr (November 18, 2013, Acela; Site 1)

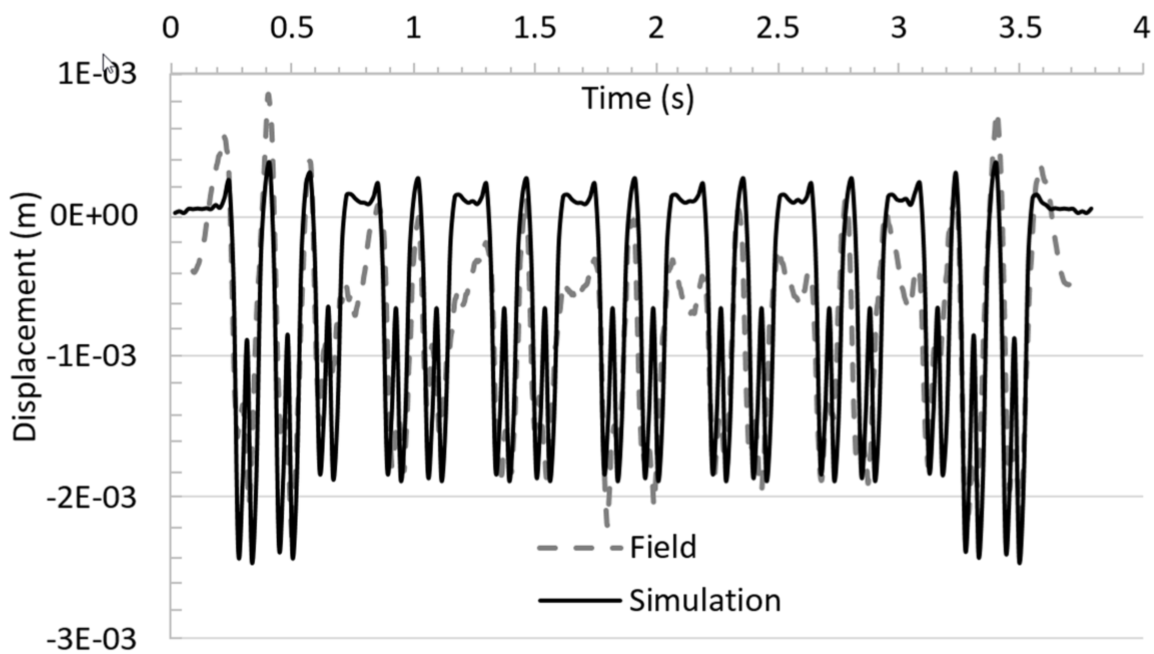

(b) v = 222 km/hr (December 19, 2013, Acela; Site 1)

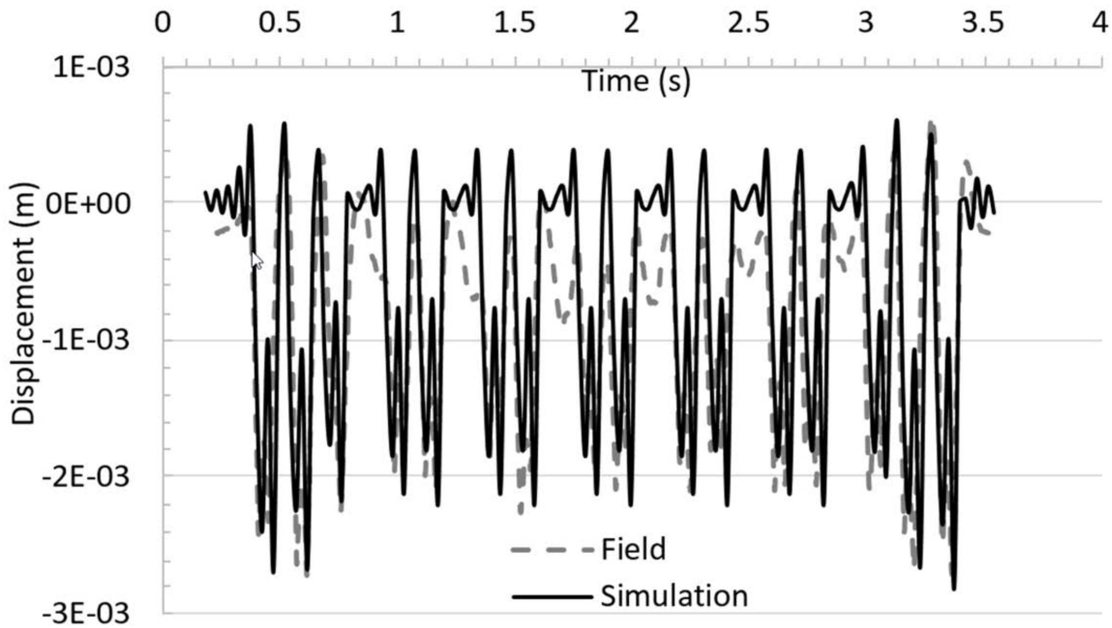

(c) v = 240 km/hr (March 18, 2014, Acela; Site 1)

Figure 30. Field Measurement and Simulation of Deflection of Rail at Different Acela Train Speeds

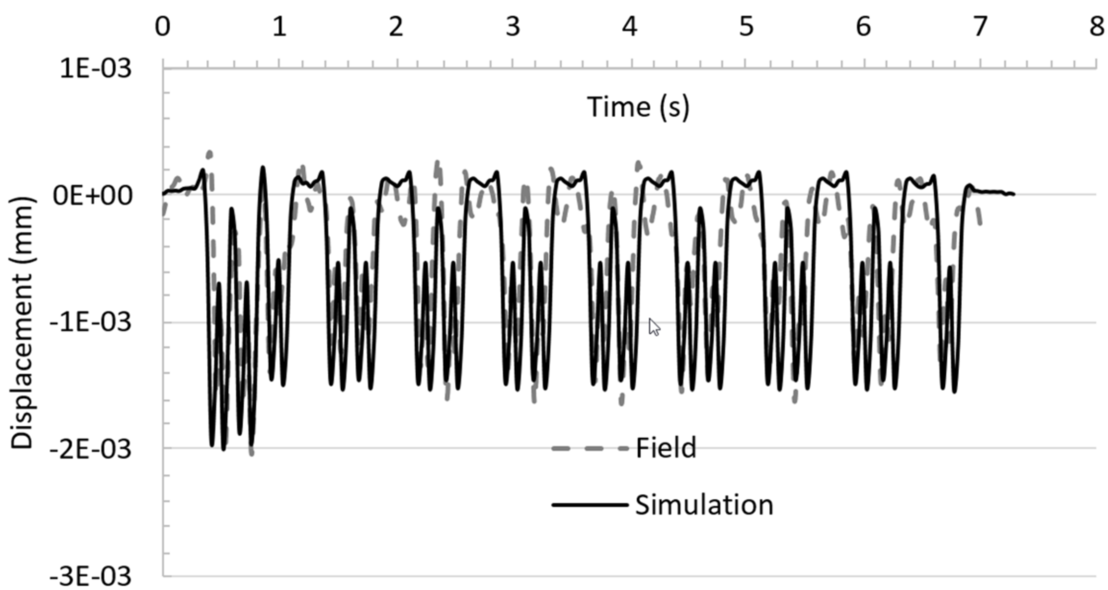

(d) v = 125 km/hr (March 18, 2014, Acela; Site 1)

Figure 31. Field Measurement and Simulation of Deflection of Rail for Regional Trains

3.5 Lac La Biche Field Verification

The model was used at the Lac La Biche (LLB) site in Canada to provide additional evidence that it can predict rail deflection. This site is very similar to the Kingston site, though freight is transported at lower speeds. Four locations within 1000 m were selected to test the model because they fit the criteria listed in Section 1.1 and were close to an area where samples had been collected. Data were available for the properties of the soil and track that were needed to use the model. This includes samples collected in the track using an Automatic Ballast Sampler (ABS), soil layers from GPR, cross detections from terrestrial laser scanning, and surficial geology. The rail size was much smaller than the Kingston site (41kg per m), and has inertia values twice as small.

The soil modulus was back-calculated using GEOTRACK with the loading conditions of the FWD test (Adegoke, 1980). This was done by forcing layer deflections to match, as closely as possible, the results of the FWD tests with realistic modulus values. The layers were based on the layers from GPR and the samples that were collected. Figure 32 shows all this information for one of the four sites. Once the results of the individual layer deflections were satisfactory, the sites were analyzed under MRail conditions to ensure that the ballast's properties, the fastener stiffness, and other track properties matched the deflections available from the MRail tests. Figure 33 shows a plot of the GPR, ground surface, geometry, MRail, and FWD data from the LLB Site.

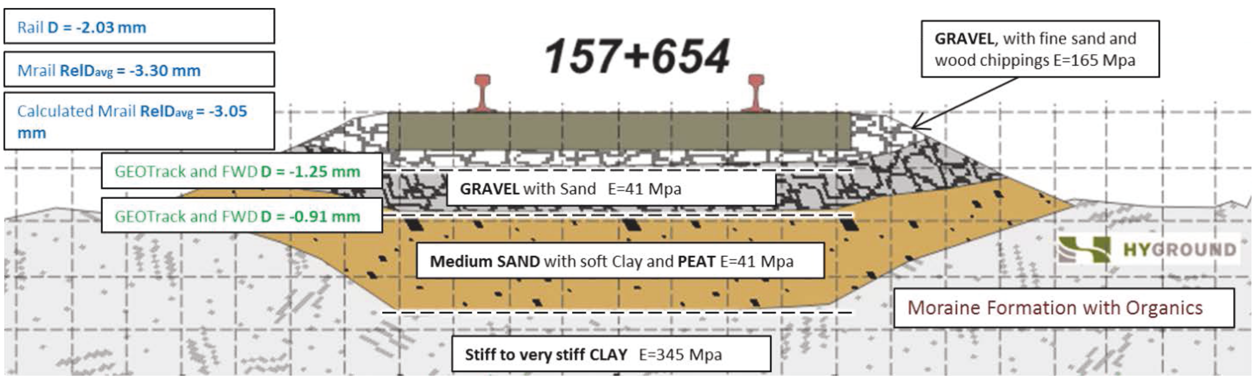

Figure 32. Subgrade Properties of the LLB Site and GEOTRACK Results at 157 + 654

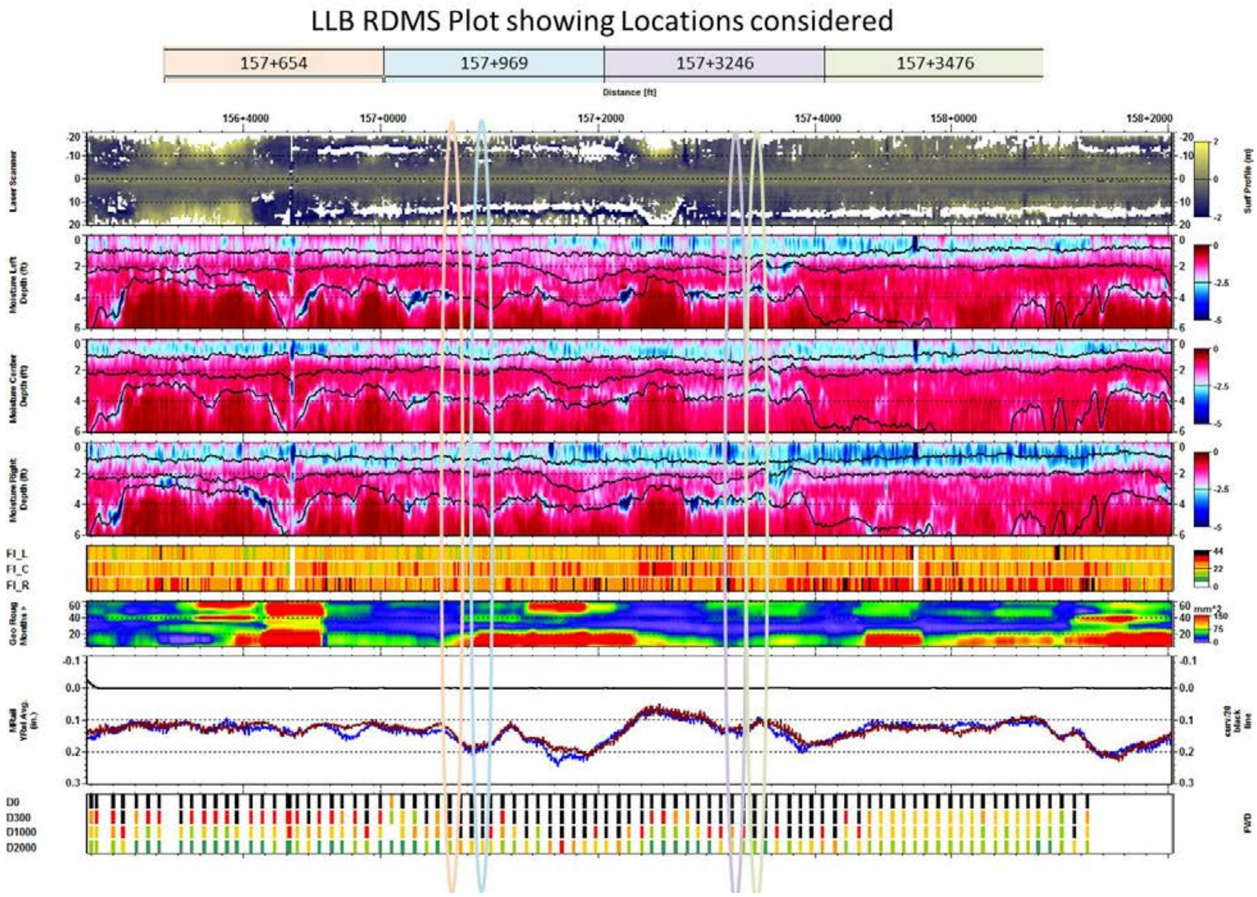

Figure 33. Lac La Biche GPR, Ground Surface, Geometry, FWD, and MRail Data

The MRail system has been developed by Shane Farritor at the University of Nebraska–Lincoln. It is an autonomous system that is capable of measuring vertical rail deflection from a rail car by using a laser. GEOTRACK was used with the loading conditions of the MRail test (see Figure 34). This provides the rail deflections under 10 ties so interpolations of the deflections in this figure give the equivalent MRail values. Once the results were satisfactory, the modulus values shown in Table 8 were trusted and the original model was used to predict the deflection to further verify it. The ABS data that was used is shown in Figure 35.

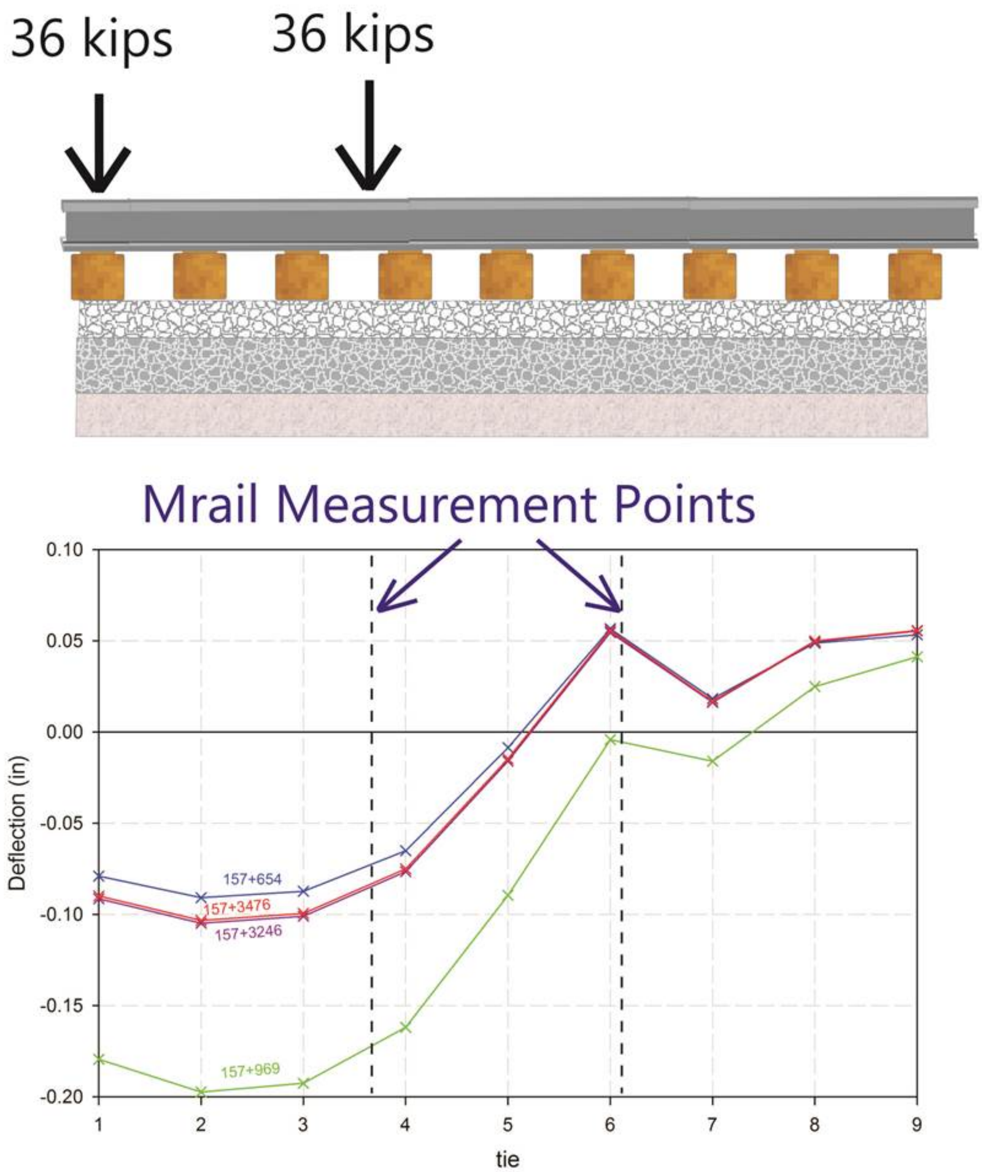

Figure 34. MRail Measurement Setup

Table 8. Lac La Biche Track Substructure Properties

Milepost	**157+654**			**157+969**			**157+3246**			**157+3476**		
Surficial Geology	**Moraine**			**Moraine**			**Organics**			**Organics**		
	L Depth From TOT (m)	C Depth From TOT (m)	R Depth From TOT (m)	L Depth From TOT (m)	C Depth From TOT (m)	R Depth From TOT (m)	L Depth From TOT (m)	C Depth From TOT (m)	R Depth From TOT (m)	L Depth From TOT (m)	C Depth From TOT (m)	R Depth From TOT (m)
Ballast	0.32	0.30	0.27	0.40	0.37	0.34	0.41	0.41	0.41	0.40	0.40	0.40
Sub-Ballast	0.55	0.60	0.55	0.63	0.63	0.65	0.73	0.73	0.72	0.61	0.63	0.61
Embankment	1.16	1.14	1.10	1.34	1.24	1.24	1.12	1.07	1.06	1.03	0.98	1.02

Milepost	**157+654**			**157+969**			**157+3246**			**157+3476**		
U (MPa)	**51.3**			**24.1**			**44.6**			**45.5**		
Depth (ft)	E (MPa)	depth from TOT* (m)	D (cm)	E (MPa)	depth from TOT (m)	D (cm)	E (MPa)	depth from TOT (m)	D (cm)	E (MPa)	depth from TOT (m)	D (cm)
Z(1)	165			103			207			276		
Z(2) [d300 in FWD]	41	0.30	-0.126	25	0.38	-0.181	22	0.41	-0.154	28	0.41	-0.174
Z(3) [d1000 in FWD]	41	0.56	-0.092	25	0.64	-0.135	24	0.69	-0.100	21	0.69	-0.127
Z(4)	41	0.84	-0.061	25	0.94	-0.080	24	0.89	-0.064	14	0.89	-0.084
Z(5)	345	1.14		69	1.27		345	1.09		620	1.09	

*TOT: top of tie

Figure 35. ABS Data Used for Developing Subgrade Layers

The results of the prediction of the rail deflection, comparing the maximum displacement for field and simulation results, are shown in Table 9. From the table, the model prediction for LLB site is conservative but still has the same trend of changing. The difference could be due to uncertainty of site characterization and error of measurement system. The model prediction for this case is quantitatively correct and within a reasonable range of error.

Table 9. Lac La Biche Rail Deflection Predictions

	157+654	157+969	157+3246	157+3476
MRail	3.30 mm	4.82 mm	3.30 mm	3.30 mm
Model Prediction	4.06 mm	5.08 mm	4.06 mm	4.06 mm

4. Model Prediction and Analysis

One of the objectives of this research was to evaluate the track performance under different speed and loading conditions. Generally, higher speed induces higher vibration (rail deflections) and generates cone-shaped ground wave motion (Bian, 2008). As shown in Figure 36, the measured rail vertical deflection presents a nonlinear increase because dynamic speed effect is considered when rail deflection is calculated. However, the dynamic effect described by the conventional method (Talbot's Equation) is a linear portion which is not appropriate to predict the speed effect at Kingston. However, the prediction of the validated model has a good agreement with the measured rail deflection.

The conventional method presented by Talbot has suggested that the static load is increased by 1 percent over 5 mph as shown in Equation 28 (Hay, 1982):

$$P_v = P + 0.01P\,(V-5) \tag{28}$$

Where, P_v = dynamic load in pounds at train speed of V
V = speed in mile per hour
P = static load in pounds.

The maximum deflection can be calculated by:

$$Y_o = P / (64EIU_{tm}^3)^{1/4} \tag{29}$$

Where, Y_o = maximum deflection
U_{tm} = Track Modulus

Figure 36 shows the rail vertical downward deflection as generated by the conventional method, field measurements, and model predictions. The field measurement range is limited to the actual measurements gathered at the site. By using a paired t test, the two lines calculated by field measurement and the conventional method can be statistically proven to be two groups of data with a significant difference ($p=0.039<0.05$, p-value determines whether two samples differ from each other in a significant way). In the same manner, the paired t test is performed between simulation and field measurement results, the p value is 0.472 which statistically shows that some dependency exists between the two populations. Therefore, we can infer that the track dynamic behavior at the Kingston site is not only caused by the linear dynamic effect like the conventional method, but also excited by some other mechanisms.

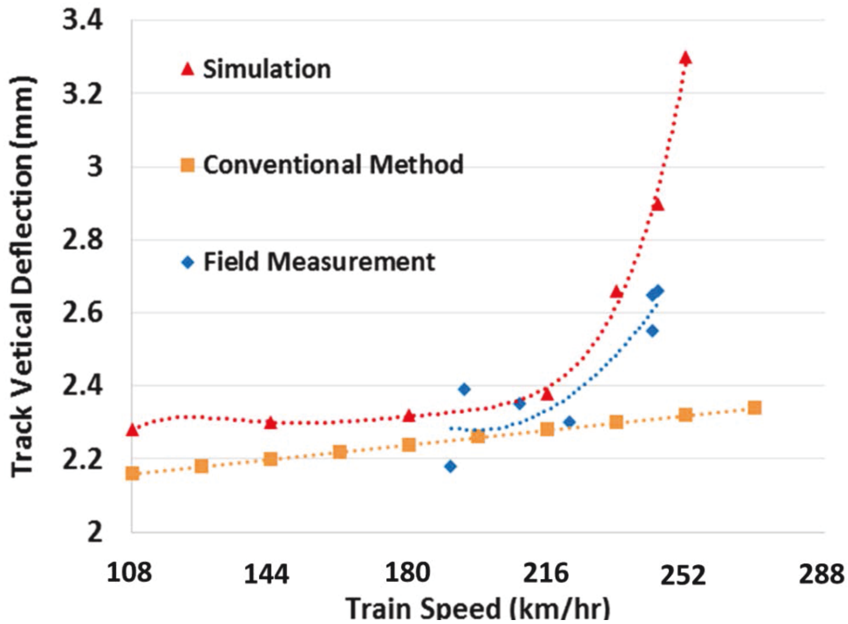

Figure 36. Comparison of the Track Vertical Downward Deflection

However, field measurements indicated that the rail deflection did not show significant increases at the current train speeds. The lower-than-expected rail deflection could be due to heavy rails and thick ballast. Therefore, the speed did not show any significant effects on rail deflection. Figure 37 shows the simulation of track vertical deflection of multiple model iterations over the full speed range 108–324 km/hr. The current maximum operational speed is shown by the circle at 66 m/s. However, if the train speed is increased to 300 km/hr, the track performance could fully enter the critical speed condition and the track deflection would substantially increase.

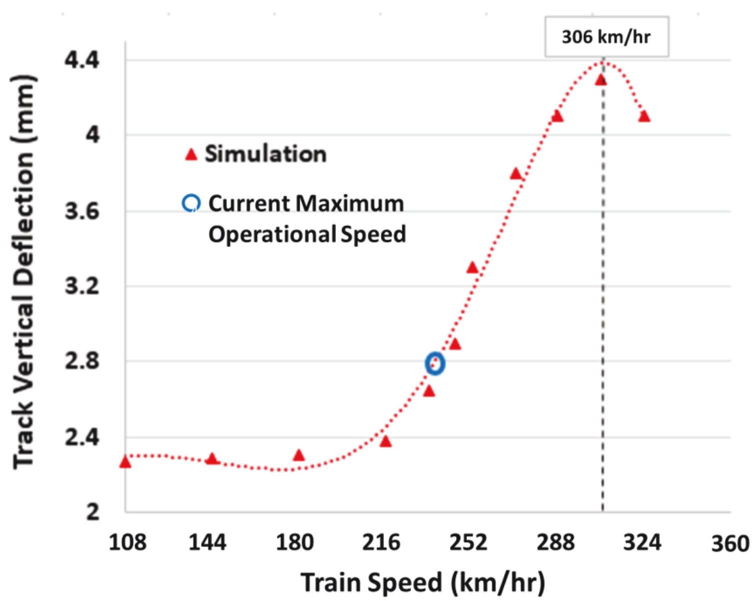

Figure 37. Simulation of Track Vertical Downward Deflection

4.1 Speed Effect on Ground Surface Wave Motion

The ground surface wave motion is one of the important phenomena that indicates critical speed. The surface wave motion at the ground surface was calculated with the data from the 3x3 array of accelerometers. The contour that represents the wave front arrival times (in seconds) relative to the arrival of the first axle of Acela train is shown in Figure 38(a). The shear wave velocity estimated by the arrival time contours (20 m/s) for the swamp soil is very similar to the shear wave velocity determined by the SASW (21.4 m/s) and bender element testing by Gnatek (2014) (24.6 m/s).

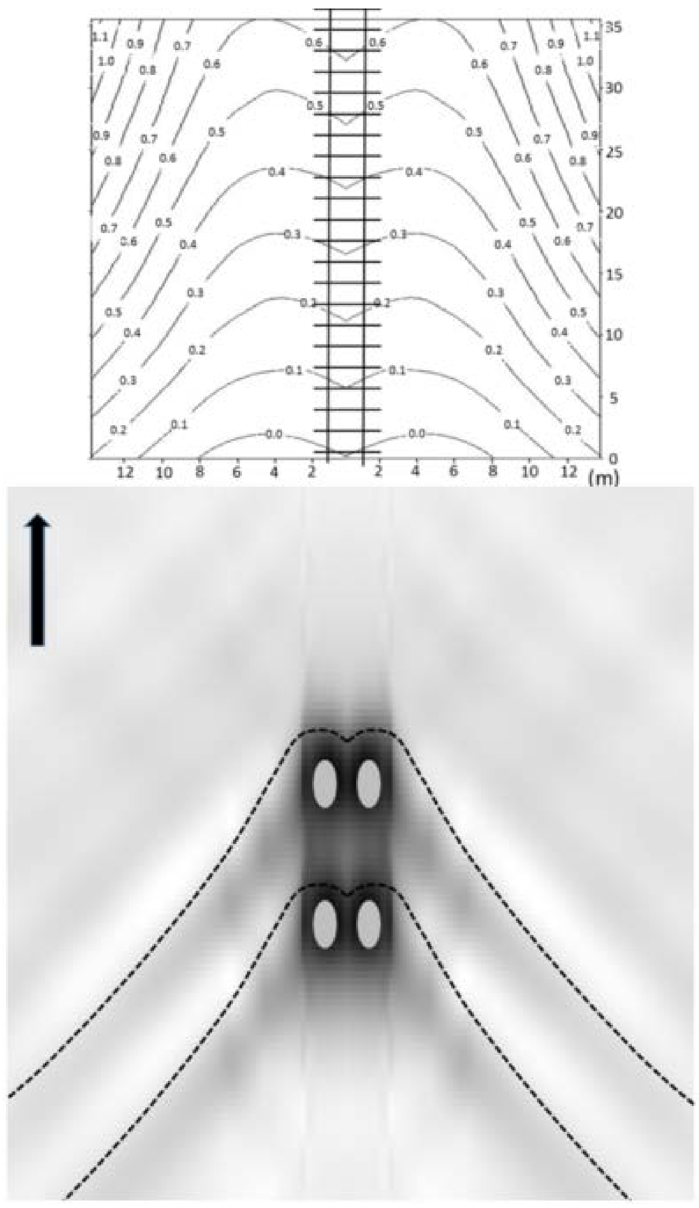

(a) **(b)**

Figure 38. Arrival Time of Shear Wave Front at 193 km/hr (Acela): (a) Field Measurement; (b) Simulation

The ground wave motion by simulation is compared with the field results in Figure 38(b). Both field measurement and model simulation have cone-shaped ground wave motion at the speed of 193 km/hr. This indicates that the surface wave motion was excited by the high-speed moving trains.

Figure 39 shows the ground wave motion by the regional train, which operates at a lower speed. The cone-shaped motion still existed but largely attenuated. This indicates that the subgrade soil at the Kingston site can be excited by the moving train even at lower speeds. It is possible because the shear wave velocity of the surface soil of the site is as low as 23 m/s.

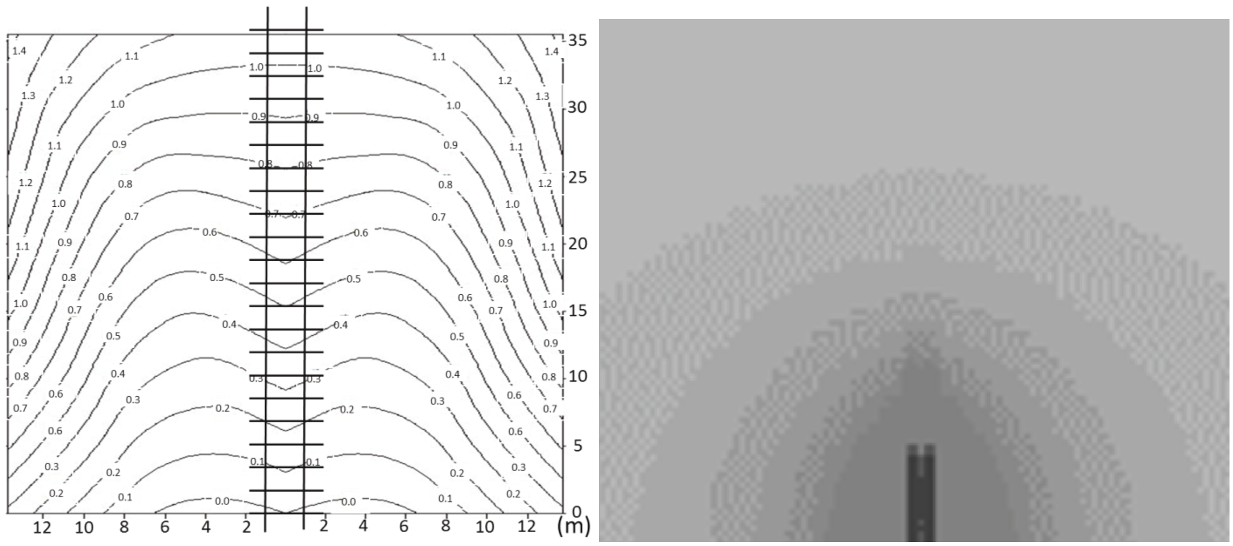

Figure 39. Arrival Time of Shear Wave Front at 125 km/hr (Regional): (a) Field Measurement; (b) Simulation

4.2 Speed Effect on Dynamic Stress Distribution in Ballast and Subgrade

In this section, the modeling techniques show the vertical displacement inside the subgrade. Figure 40 shows the displacement contour of cross section of subgrade at normal speed and critical speed respectively. The plotted regions are half domain, which means that half of the cross section is presented here. The plot shows the contour of displacement for each element in vertical direction under moving train loading. From the left to right, the displacement contour represents the train speed condition from 18 km/h up to 306 km/hr, respectively. Figure 40(a) shows the train running at low speed (18 km/hr in this case), which is much below the critical speed; Figure 40(b) presents the train speed when the cone-shaped ground wave motion starts to grow; Figure 40(c) has a larger area of influence, which denotes the condition of highest speed of Acela at Kingston site. Figure 40(d) presents the predicted critical condition, which is train running at 306 km/hr.

The influence region and magnitude of displacement increased slightly from (a) to (b), but increased significantly when the Acela reached 240 km/hr (approaching the highest current operational speed). Displacement will result in high stress in ballast and subgrade and eventually cause ballast breakage and high-rate deformation of subgrade. It may be the reason causing the higher maintenance requirements at this site. In addition, the deformed region is substantially enlarged when train is running at the critical speed (which is 306 km/hr in this area). In Figure

36, the track deflection in the prediction changes from 2.3 mm to 2.8 mm when the train speed increases from 125 km/hr to 240 km/hr. The change in track deflection is not that significant which may be due to heavy rails or the large amount of ballast, however, the prediction shows that the stress distribution in the subgrade is substantially increased. This is important since it could be a problem when increasing the operation speed. As a result, the next step of this research will be to investigate the subgrade performance.

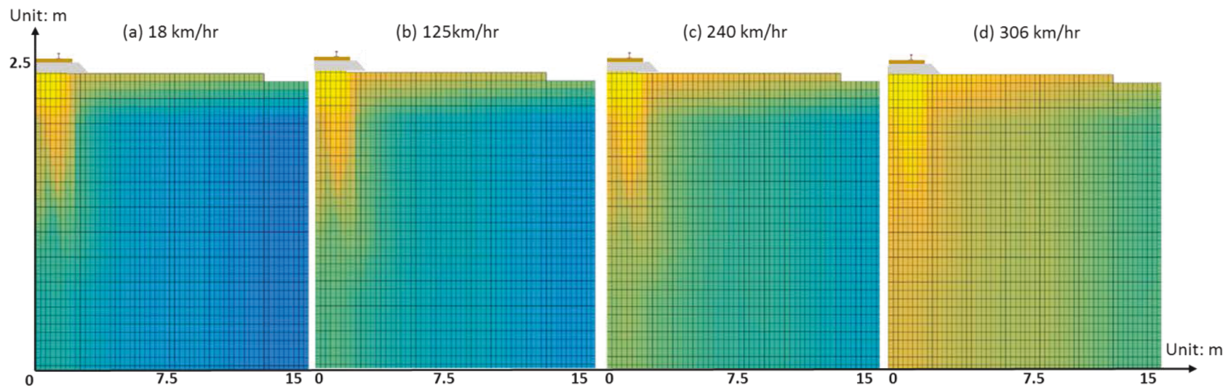

Figure 40. The Displacement Contour of Subgrade at Different Speed Conditions

4.3 Discussion of the Speed Effect at the Kingston Test Site

This section analyzes the critical speed effect at the Kingston test site based on the field measurements and model prediction. The Kingston site is known as the Great Swamp area and requires more frequent track maintenance. It was suspected that the critical speed condition might exist at this particular location. The conventional definition of the critical speed is the speed at which vibrations propagate within the track structure and subgrade at a speed close to the Rayleigh wave velocity of the subgrade soil. As trains travel at speeds approaching the critical speed, rail deflections are expected to present significant increases and soft ground surface should show cone-shaped wave motion.

According to the field tests at Kingston, the cone-shaped surface wave motion started at the speed as low as 90-120 km/hr. However, the relatively small measurements of rail/track deflections do not suggest that the critical velocity has been reached. In other words, the cone-shaped surface wave motion and the increase in rail deflection did not occur at the same time. Also, neither the surface wave motion nor the slightly increased rail deflection under the current operational speed can adequately explain the extra track maintenance required for the site. However, the model predicted that the stress level in the track substructure under current operational speed was significantly increased. The high-level stress rather than the excessive deflections could be causing the frequent maintenance, but the stress in the subgrade cannot be directly measured. Therefore, the current model is the most effective way to explore and evaluate the track performance.

The track performance at the Kingston site experienced three stages as the speed increases: 1) the appearance of the cone-shaped surface wave motion (around 90-120 km/hr); 2) the compressive stress increase in the subgrade (by modeling, around 240 km/hr); 3) the rail deflection increase (by modeling, over 300 km/hr).

- As shown in Figure 38 and Figure 39, the cone-shaped surface wave pattern coincided with the train speed reaching the Rayleigh wave velocity of the soil. In other words, the vibration caused by the train matched the natural frequency of the subgrade since train speed hits the Rayleigh wave velocity of that area. However, based on actual measurements of the rail displacements, the conventional criteria for the critical condition were not met.
- As the train speed increased to 240 km/hr, which was the highest recorded train speed at Kingston, the rail displacement was not significantly increased. However, the compressive stress contour presented a significant increase at this speed. The increased maintenance may be required due to the excessive stress instead of excessive deformation.
- The critical condition predicted by the model corresponds to train speeds of over 300 km/hr. The stress level and rail displacement will be substantially increased.

The summary of the speed effect on track performance is shown in Table 10.

Table 10. Analysis of the Speed Effect on the Track Performance at Kingston

	125 km/hr	**240 km/hr**	**306 km/hr**
Speed Category	Reach the RWV* of the swamp	Highest current operational speed	Predicted Critical Speed
Cone-shaped Surface Wave	Yes	Yes	Yes
Rail Vertical Displacement	Safe	Safe	Significantly increased
Stress Level in Subgrade	Slightly increased	May affect track maintenance	May affect track maintenance

* RWV: Rayleigh wave velocity

Therefore, the effect caused by the critical speed cannot be interpreted the same as the conventional definition, and a more appropriate and accurate interpretation needs to be provided for the Kingston site. Therefore, the authors believe that the critical speed could be defined in two levels for the Kingston site:

1. The current operational speed causing significant increase in stress intensity of the cross section, at which more frequent ballast maintenance is needed.
2. The predicted speed over 300 km/hr causing significant increase in rail deflection, at which derailment becomes a concern.

The high-level stress can explain the more frequent track maintenance and the predicted larger rail deflection could affect the operational safety. The main reasons causing the divided critical speed characteristics could be the complicated tie-ballast-soil system and the geometry of the cross section. If a train is running directly on soft and homogeneous subgrade, these two critical speeds coincide.

5. Conclusion

The field investigation was successfully performed at the Great Swamp National Wildlife Refuge in Kingston, RI (commonly known as the Great Swamp area). The site investigation included several geotechnical and geophysical field tests, including:

- Dynamic Cone Penetrometer (DCP)
- Spectral Analysis of Surface Wave (SASW)
- Ground Penetrating Radar (GPR)
- Light Detection and Ranging (LiDAR)

Through the investigation, the subgrade was proven to be soft and the stiffness to be as low as 1 to 3 MPa at the Great Swamp area. In addition, the track performance was measured by using a 3x3 array of accelerometers mounted on one side of the track at the Kingston site. The rail deflections were calculated by double integrating the accelerations of the trains running at several speeds.

A 3D dynamic track-subgrade interaction model was modified and validated to predict the track and soil dynamic responses under different train speeds. The model simulated the track structure with discrete ties, with designated spacing and ballast masses. The ballast/soil interface was described by a complex Green's function, which is derived from a 3D finite element method model considering speed effects on the subgrade. Also, the cross-section change was considered in the model, which enables the model to simulate any terrains in the longitudinal direction. In order to verify the accuracy of the proposed model, field validation was conducted at the Kingston site and the LLB site at a range of speeds.

Field measurements combined with the validated model were used to evaluate the track performance and determine whether the critical speed effect exists at the Kingston site. The track performance was evaluated in three aspects:

1) *Maximum rail vertical deflection.* The simulation results matched the field measurements very well for many speeds (125 km/hr to 240 km/hr). The paired t test analysis showed that there exists non-linear dependency in the field measurement and model prediction. The maximum rail deflection presented a non-linear increase in behavior as the train approaches critical speed. From the track deflection analysis, the conventional method (Talbot's Equation) was not able to thoroughly predict the track behavior at the critical speed. Therefore, the non-linear increase in track deflection was not only caused by the linear dynamic effect described by the conventional method, but also by some other mechanisms. However, even though the rail deflection increased in a nonlinear manner, the magnitude of the increase was not significant at these speeds.
2) *Ground surface wave propagation.* The ground surface wave propagation had been detected with a cone-shaped mode in the field and modeling, even without any significant increase in rail deflection. The cone-shaped wave motion started to grow at a much lower speed than the speed causing large rail deflection. In other words, the cone-shaped surface wave motion and the increase in rail deflection did not occur at the same time, which does not agree with the conventional criteria for a critical speed condition.

3) *Stress level in track structure.* The stress level predicted by the model in the track substructure under current operational speeds was significantly increased. The high stress level, rather than the excessive deflections, could be the reason for the frequent maintenance at the Kington site. Further, based on model predictions, increasing the train speed to over 300 km/hr (higher than current operational speeds) will significantly increase track stress and rail deflection.

This report provides a more appropriate and accurate interpretation of track dynamic behavior near the critical speed. The high level of stress on the track structure can explain the more frequent maintenance required, and the predicted larger rail deflection could affect the operational safety. For the Kingston site, authors define critical speed in two ways: 1) The current operational speed causing a significant increase in the stress intensity of the track, requiring increased track maintenance; and 2) the predicted speed over 300 km/hr causing significant increase in rail deflection, at which derailment becomes a concern.

The numeric model was not only an effective and efficient tool to predict the track and subgrade performance at different train speeds, but it can be useful for designing new tracks and evaluating track maintenance requirements for high-speed rail on soft subgrade.

Additional research is recommended to quantify ballast particle movement under these conditions. These results will help to confirm the relationship between train speeds, soil characteristics, and the need for increased track maintenance.

6. References

Adegoke, C. W., Chang, C. S., and Selig, E. T. (1980, November). "GEOTRACK Model for Railroad Track Performance." *Journal of the Geotechnical Engineering Division*, *106*(11), 1201–1218.

Barbour, L., Hendry, M., and Hughes, D. A. (2010). "Track displacement and energy loss in a railway embankment." *Proceedings of the Institute of Civil Engineers - Geotechnical Engineering*, *163*(1), 3–12.

Berggren, E., and Smekal, A. (2002). "Mitigation of Track Vibration at Ledsgard Sweden, Field Measurements Before and After Soil Improvement." *European Association of Structural Dynamics.* Fifth International Conference, 491–496. EURODYN2002: Munich, Germany.

Bian, X., Chen, Y., and Hu, T. (2008). "Numerical simulation of high-speed train induced ground vibrations using 2.5D finite element approach." *Science in China Series G: Physics, Mechanics and Astronomy* (pp.632–650). SP Science in China Press.

Chrismer, S., Gnatek, D. E., Ho, C. L., Huang, H., and Hysip, J. P. (2013). "Field Measurement of Ground Accelerations Resulting from High Speed Trains on Soft Soil." Proceedings for Transportation Research Board 93rd Annual Meeting. Transportation Research Board.

DeBeer., M. de Franca, V. M. P., Lockwood, D., and Ringwood, B. (1992). "Analysis and Classification of DCP Survey Data." Technology and Information Management Programme, CSIR Transportek: Pretoria, South Africa.

Dieterman, H. A., and Metrikine, A. V. (1997). "Steady-state displacements of a beam on an elastic half-space due to a uniformly moving constant load." *European Journal of Mechanics*, A/Solids, *16*(2), 295–306. Available at: http://homepage.tudelft.nl/v5u5c/My%20journal%20papers%20in%20pdf/21_Steady%20state%20displacements%20of%20a%20beam%20on%20an%20elastic%20half%20space%20due%20to%20a%20uniformly%20moving%20load_European%20Journal%20of%20Mechanics%20A_Solids_1997.pdf.

Dieterman, H.A., and Metrikine, A. V. (1997). Three-Dimensional Vibrations of a Beam on an Elastic Half-Space: Resonance Interaction of Vertical-Longitudinal and Lateral Beam Waves. *Journal of Applied Mechanics*, *64*(4), 951–956.

Dominguez, J., and Galvin, P. (2009). "Experimental and numerical analyses of vibrations induced by high-speed trains on the Cordoba-Malaga line." *Soil Dynamics and Earthquake Engineering*, *29*(4), 641–657. Elsevier Ltd.

Gao, Y., Huang, H., and Stoffels, S. (2014). "Fully Couple Three-Dimensional Train-Track-Soil Model for High Speed Rail." *Transportation Research Record: Journal of the Transportation Research Board*, *2448*, 87–93.

Hay, W. (1982). *Railroad Engineering*. Second Edition: John Wiley & Sons.

Huang, H., Shen, S., and Tutumluer, E. (2009, December). "Sandwich Model to Evaluate Railroad Asphalt Trackbed Performance Under Moving Loads." *Transportation Research Record Journal of the Transportation Research Record Board*, *2117*, 57–65.

Research Board 93rd Annual Meeting Compendium of Papers: Washington, DC.

Abbreviations and Acronyms

3D	Three-Dimensional
ABS	Automatic Ballast Sampler
BOEF	Beam-on-Elastic-Foundation
DCP	Dynamic Cone Penetrometer
FEM	Finite Element Method
FWD	Falling Weight Deflectometer
GPR	Ground Penetrating Radar
HSR	High-Speed Rail
LiDAR	Light Detection and Ranging
LLB	Lac La Biche
NEC	Northeast Corridor
SASW	Spectral Analysis of Surface Wave

Appendix A.
Field Equipment

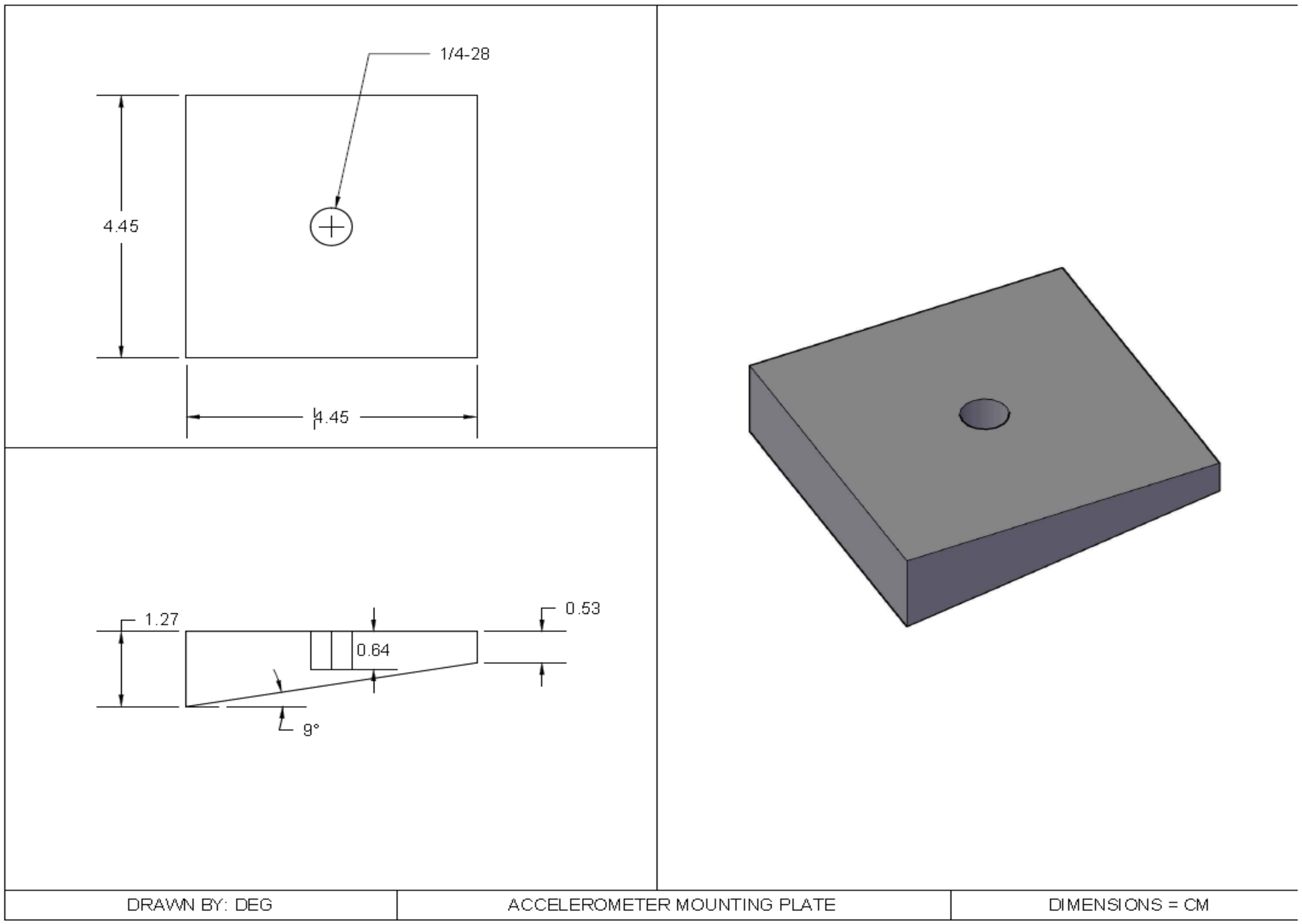

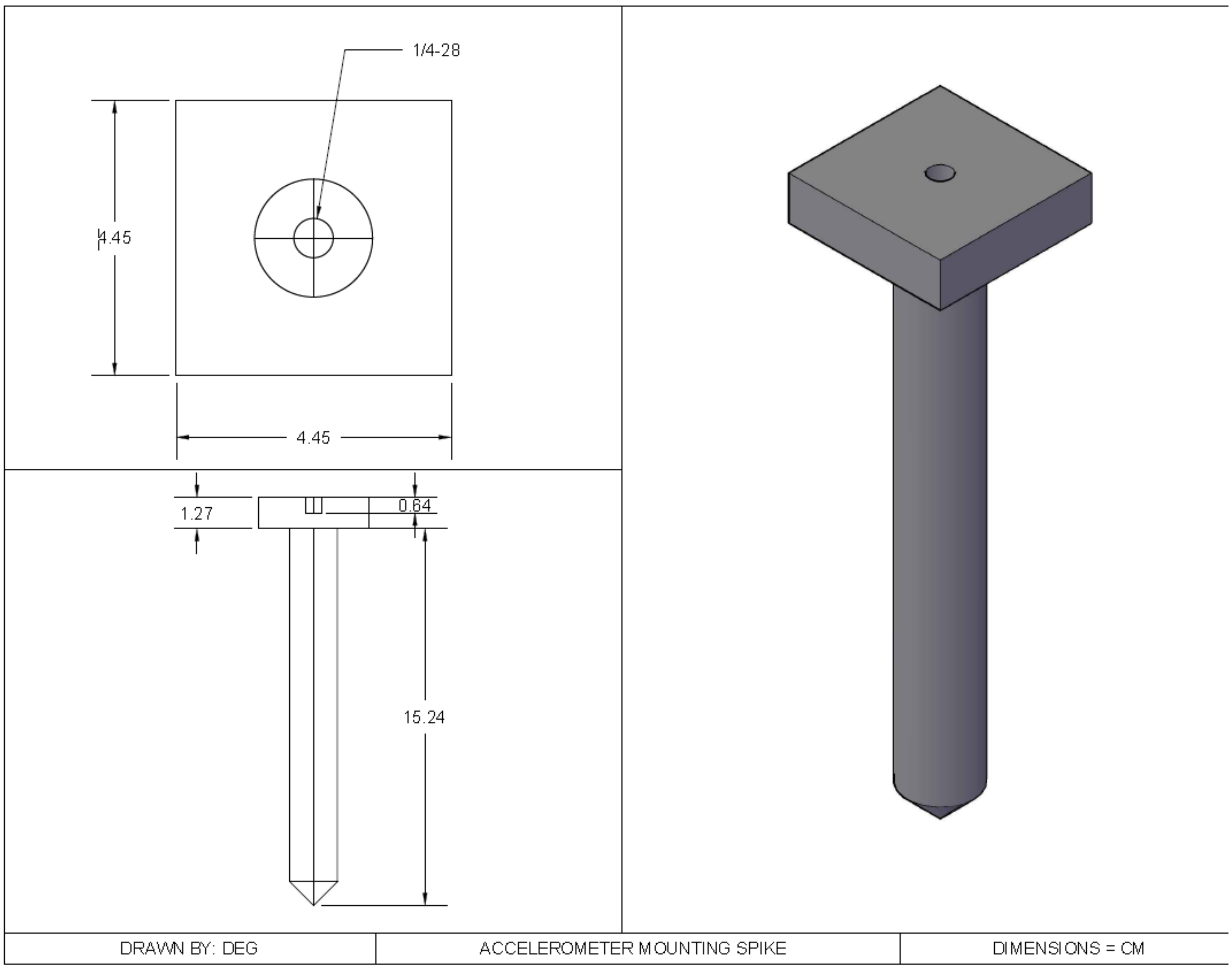
1/4-28
4.45
4.45
1.27
0.64
15.24
DRAWN BY: DEG
ACCELEROMETER MOUNTING SPIKE
DIMENSIONS = CM

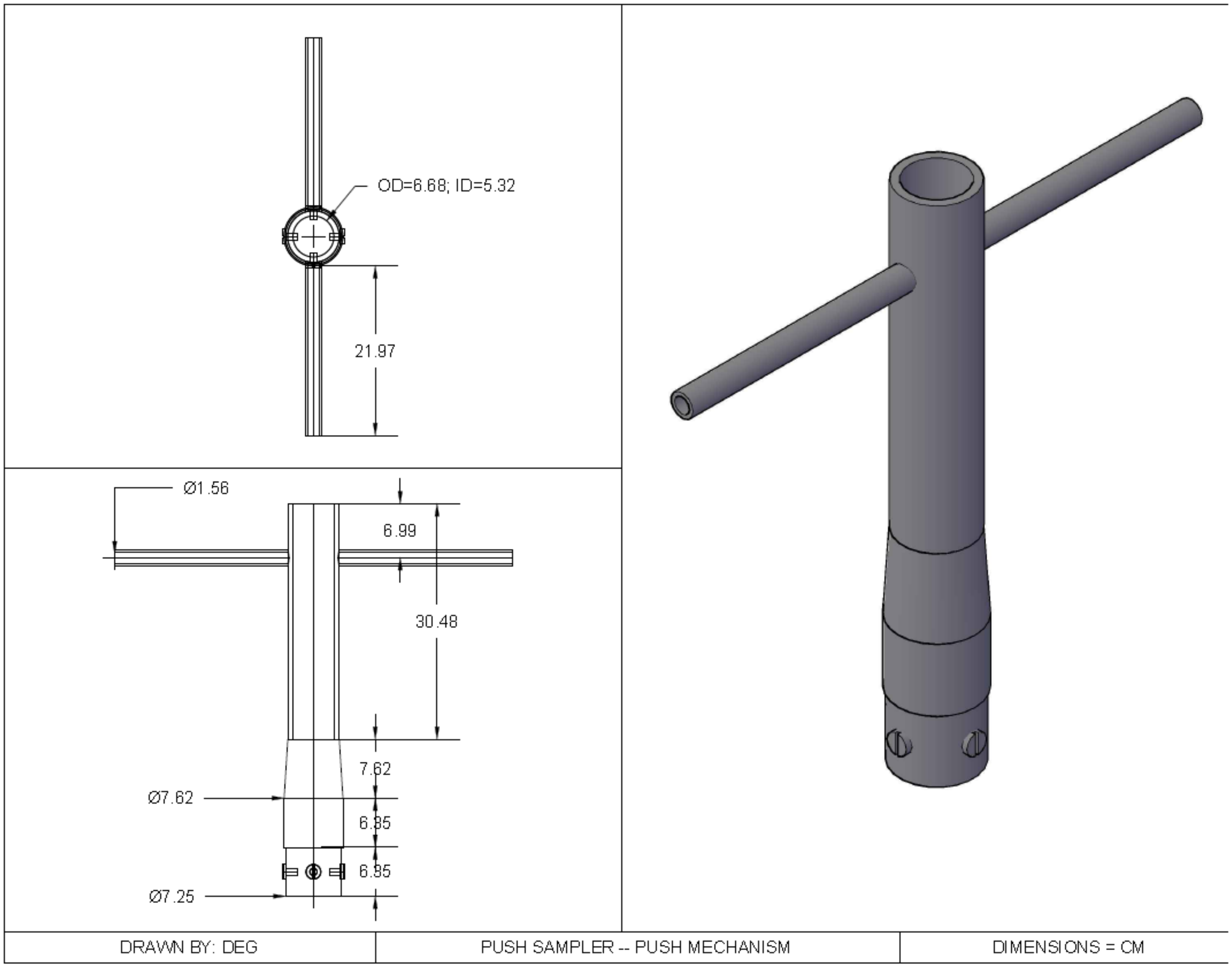
OD=6.68; ID=5.32
21.97
Ø1.56
6.99
30.48
7.62
Ø7.62
6.35
6.35
Ø7.25
DRAWN BY: DEG
PUSH SAMPLER -- PUSH MECHANISM
DIMENSIONS = CM

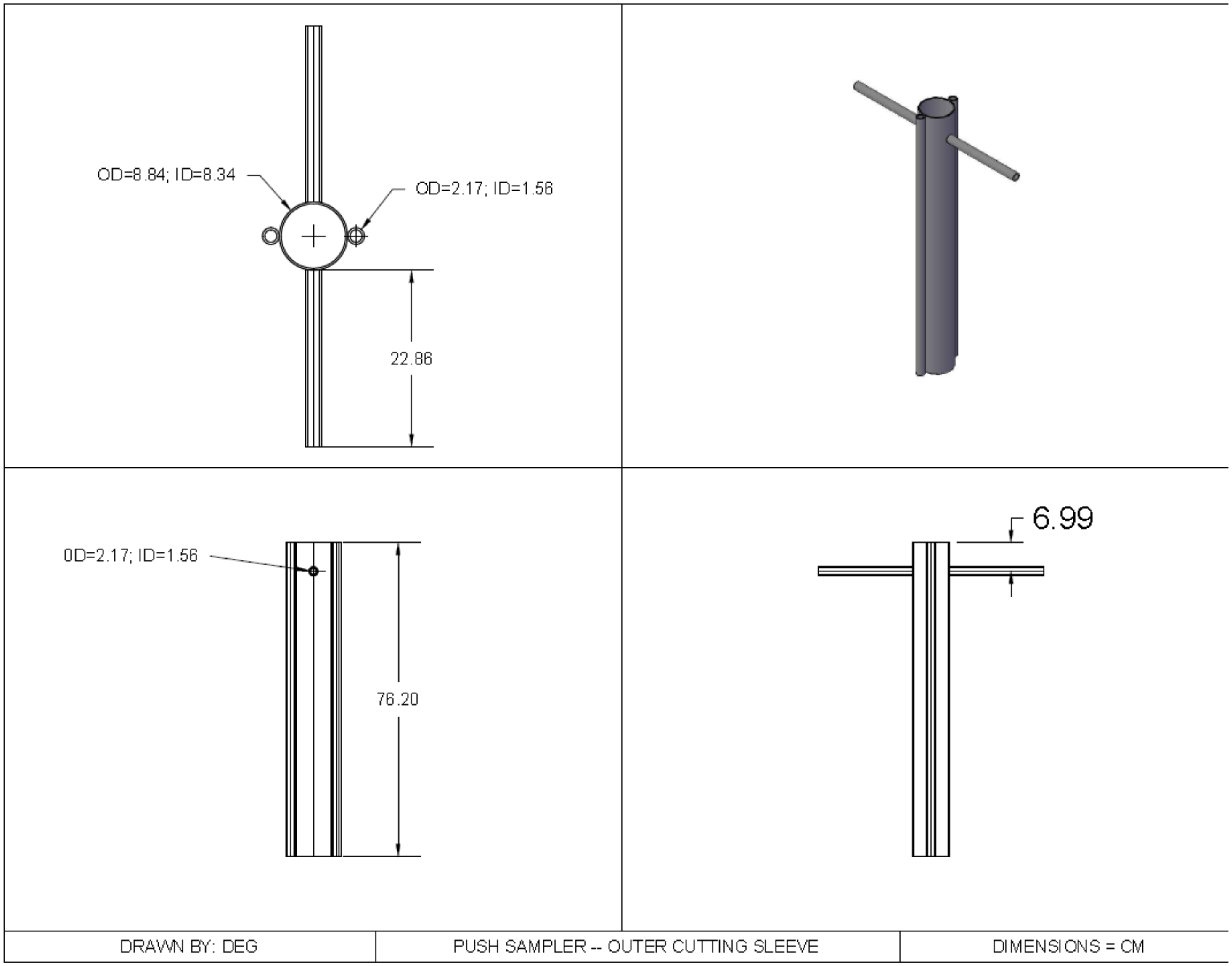
OD=8.84; ID=8.34
OD=2.17; ID=1.56
22.86
0D=2.17; ID=1.56
76.20
6.99
DRAWN BY: DEG
PUSH SAMPLER -- OUTER CUTTING SLEEVE
DIMENSIONS = CM

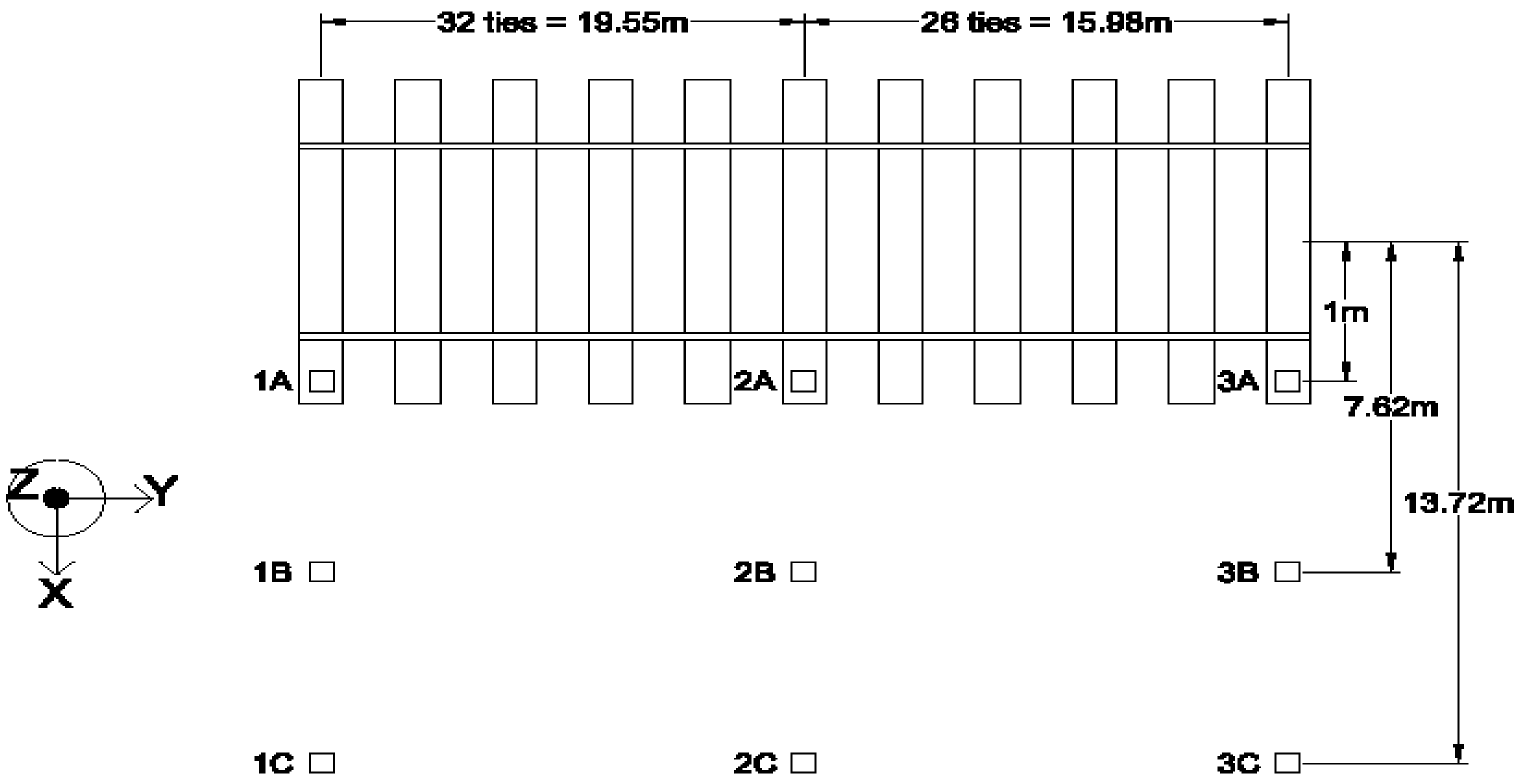

November 18, 2013, MP 156-23 (Site 1) Accelerometer Array

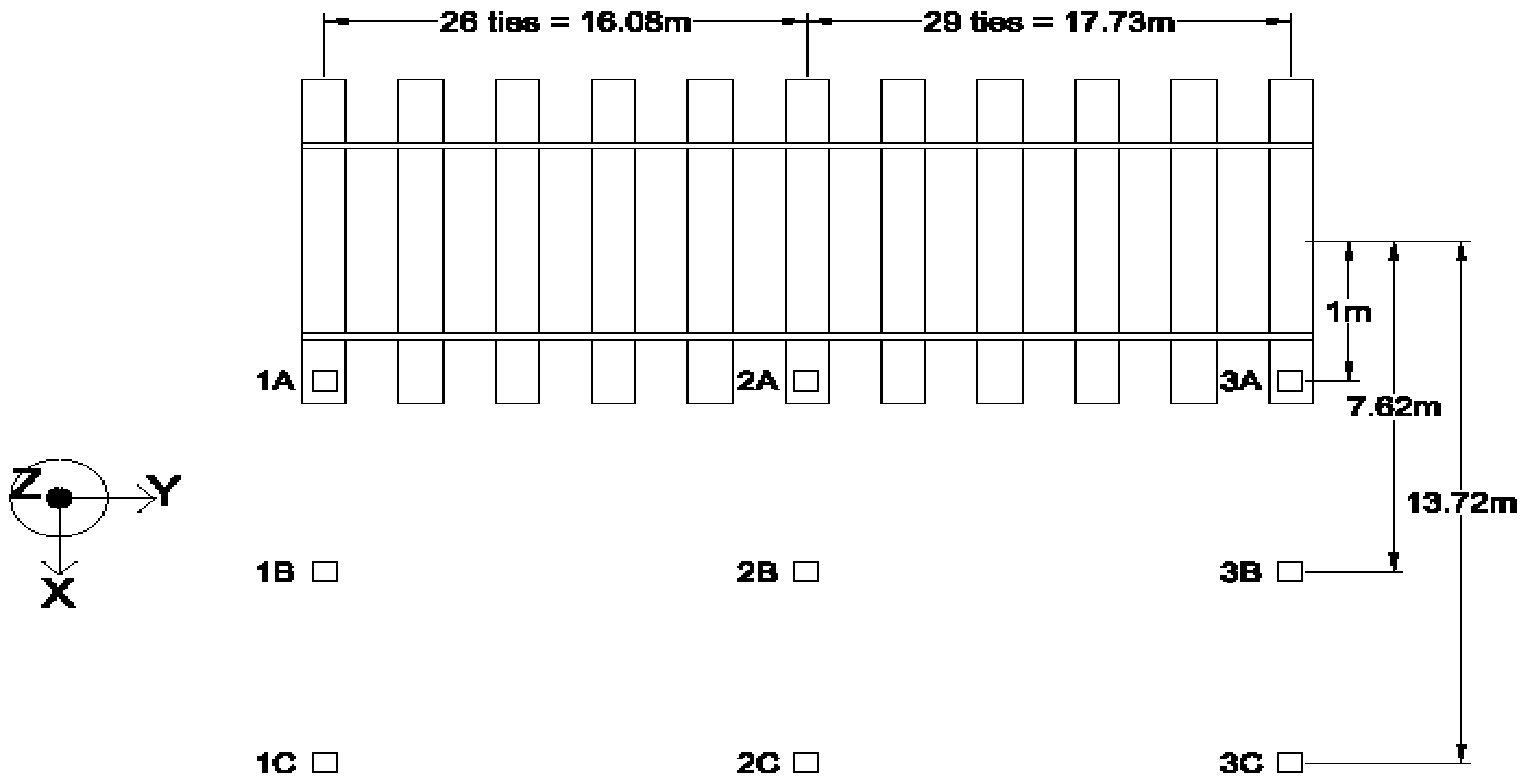

November 18, 2013, MP 155-41 (Site 2) Accelerometer Array

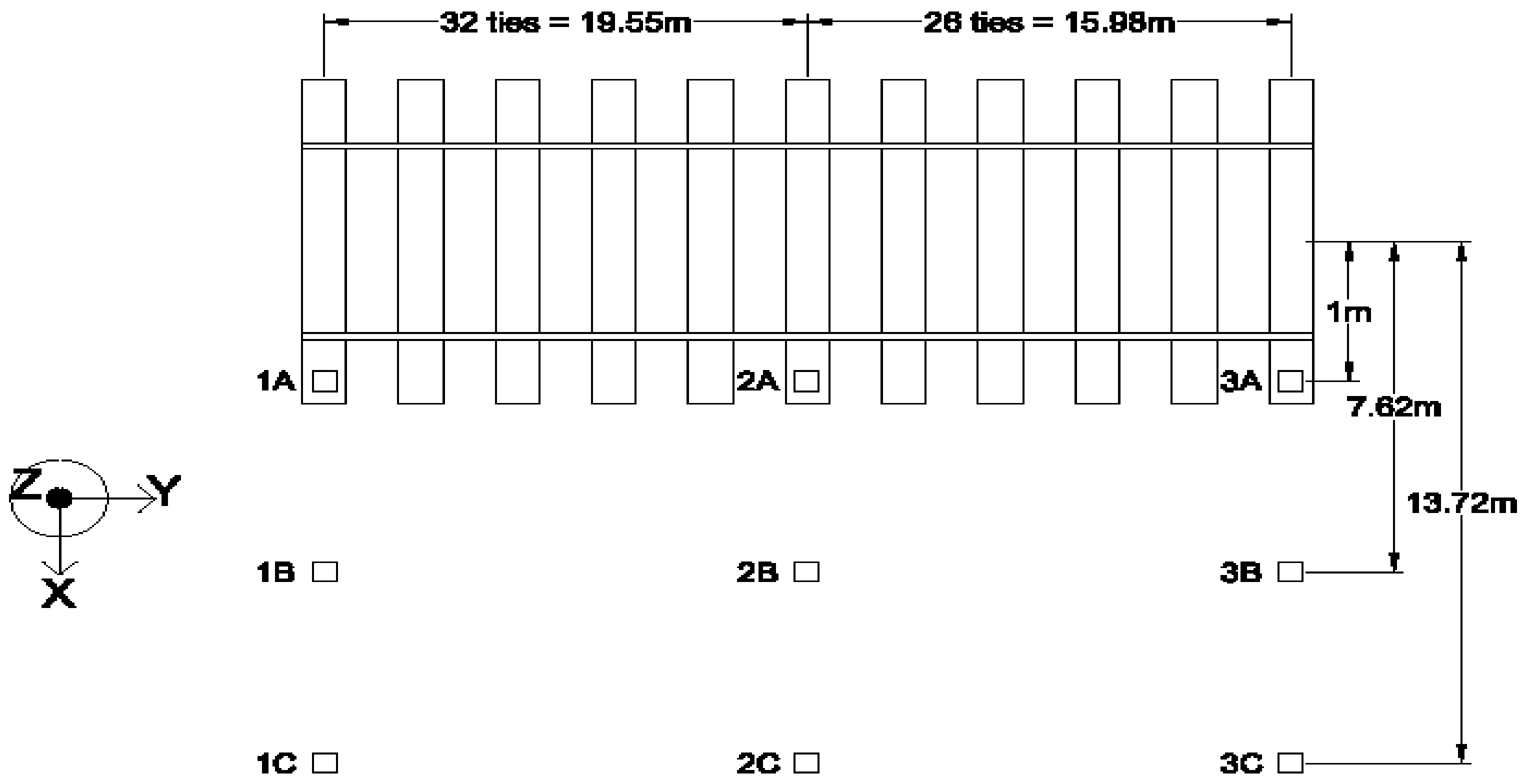

December 19, 2013, MP 156-23 (Site 1) Accelerometer Array

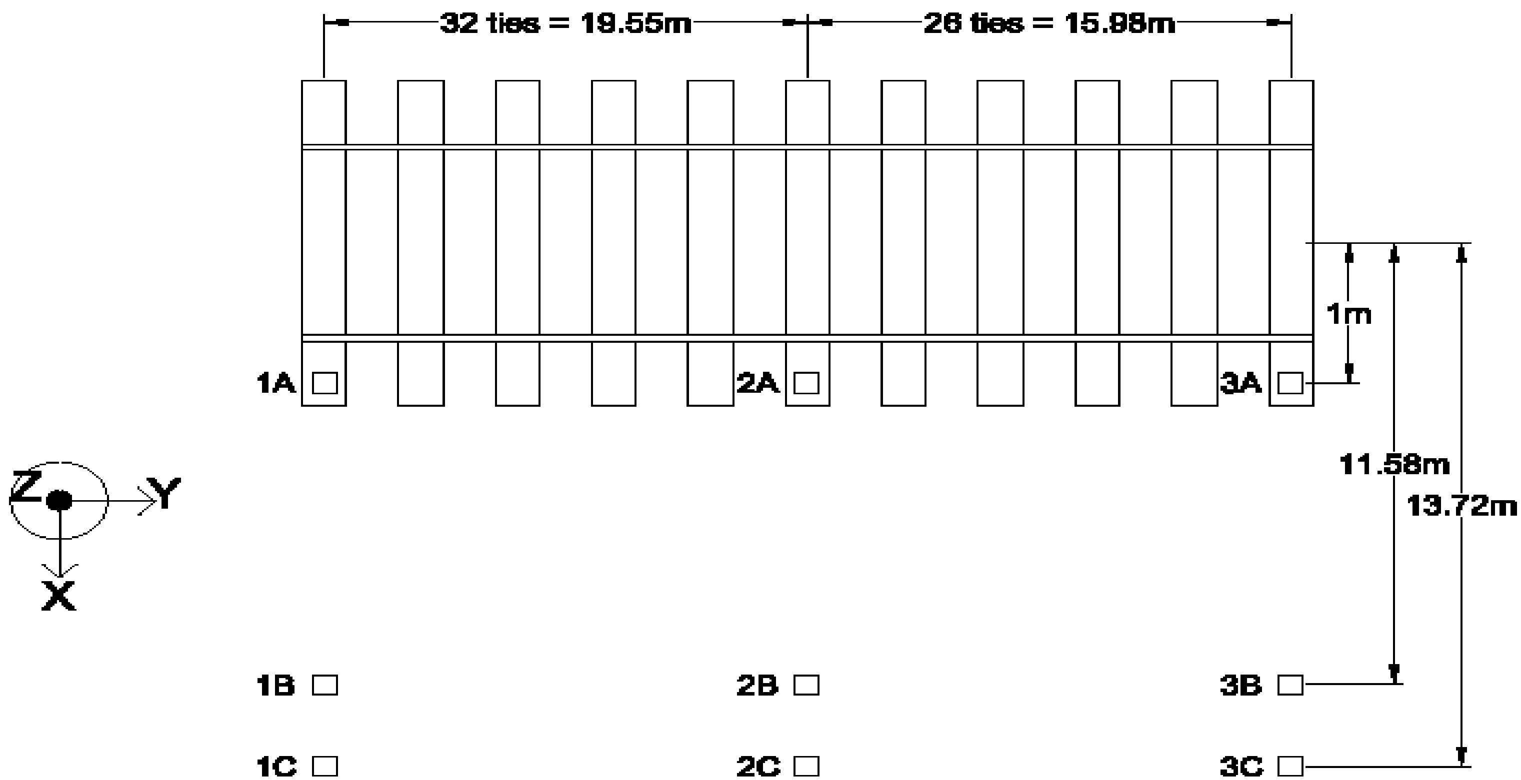

March 18, 2014, MP 156-23 (Site 1) Accelerometer Array

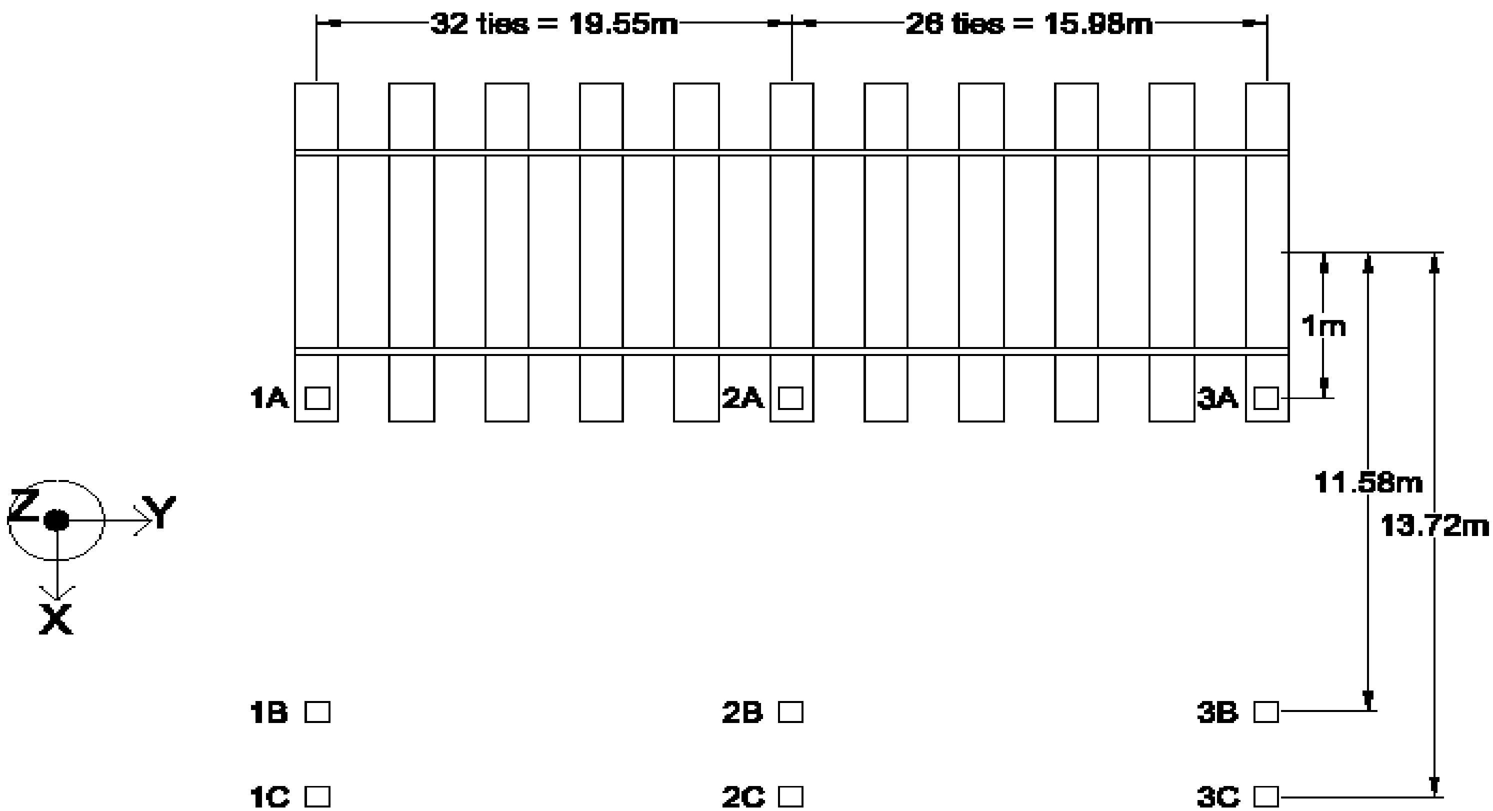

April 9, 2014, MP 156-23 (Site 1) Accelerometer Array

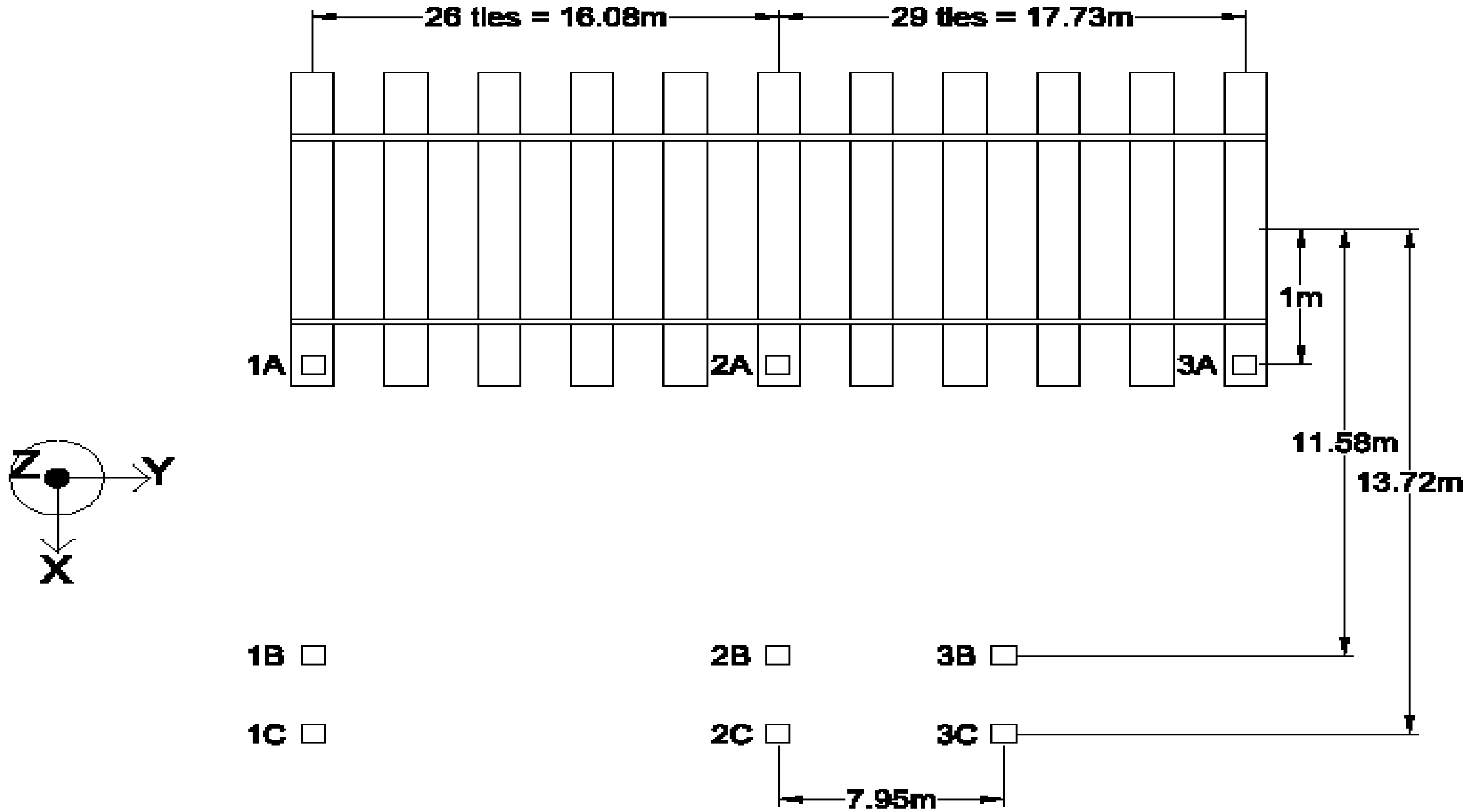

April 10, 2014, MP 155-41 (Site 2) Accelerometer Array

Appendix B.
Weather Data

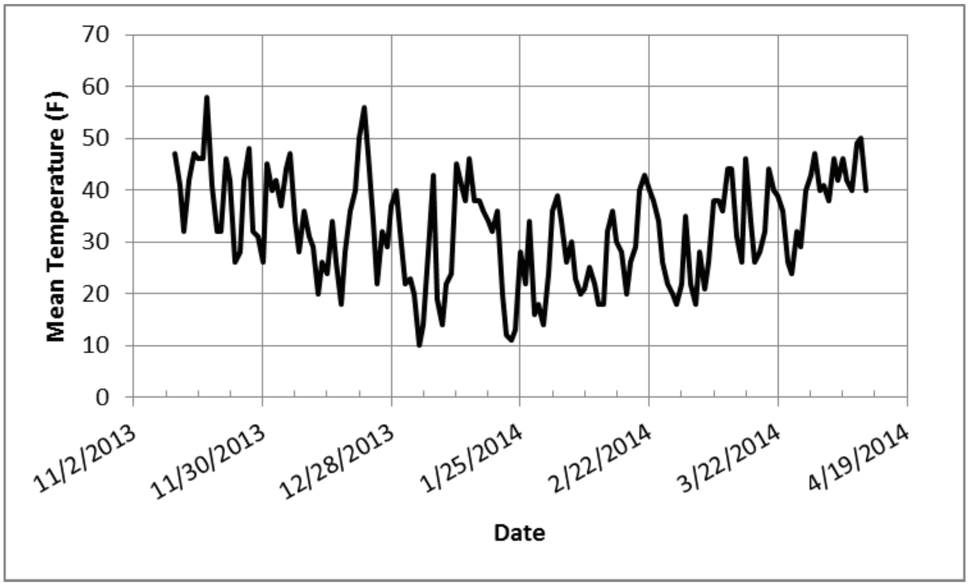

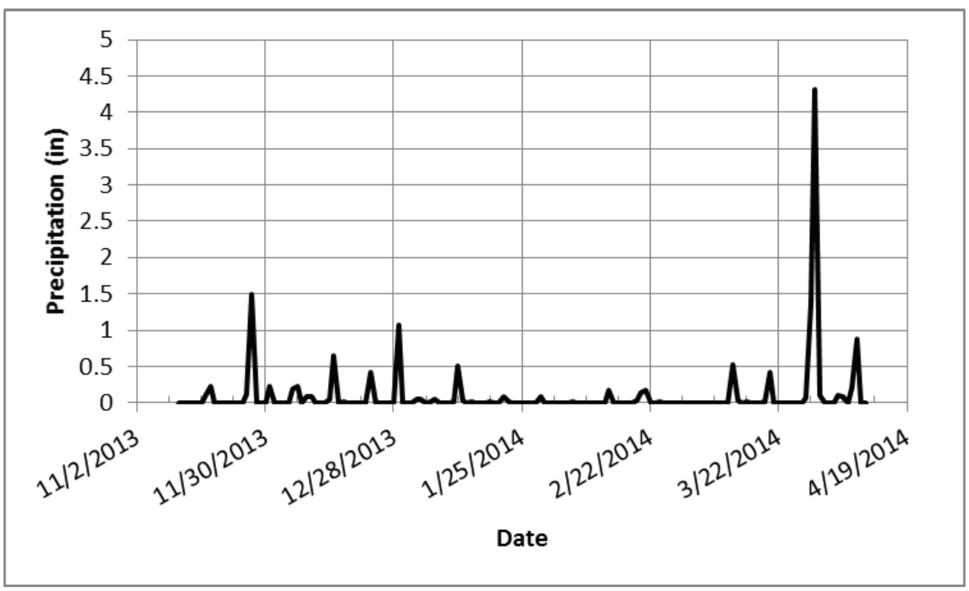

EDT	Max Temp. (F)	Mean Temp. (F)	Min Temp. (F)	Precip. (in)	Events
11/11/2013	53	47	41	0	
11/12/2013	52	41	28	0	Rain-Snow
11/13/2013	37	32	26	0	
11/14/2013	50	42	33	0	
11/15/2013	55	47	39	0	
11/16/2013	55	46	35	0	
11/17/2013	59	46	34	0.11	Fog-Rain
11/18/2013	61	58	50	0.22	Fog-Rain

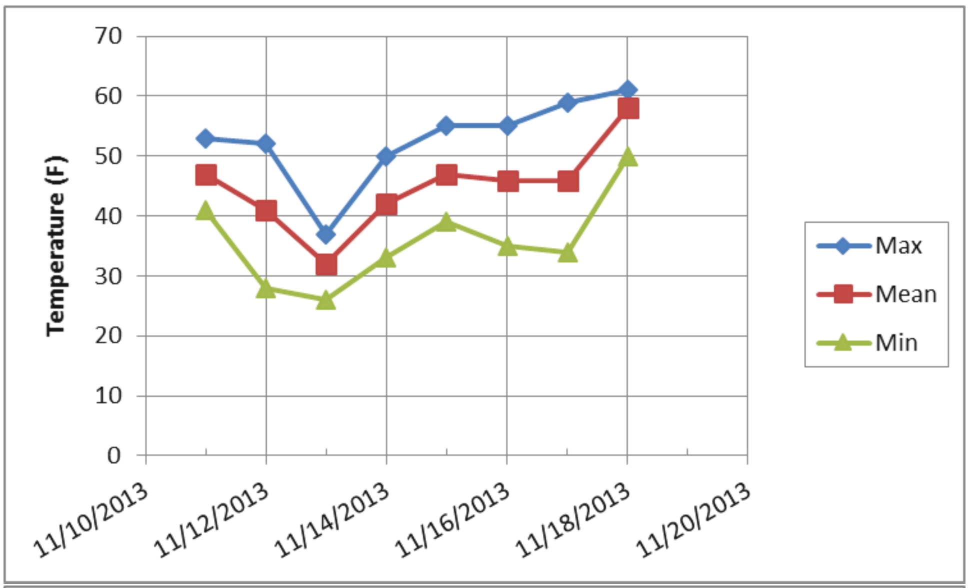

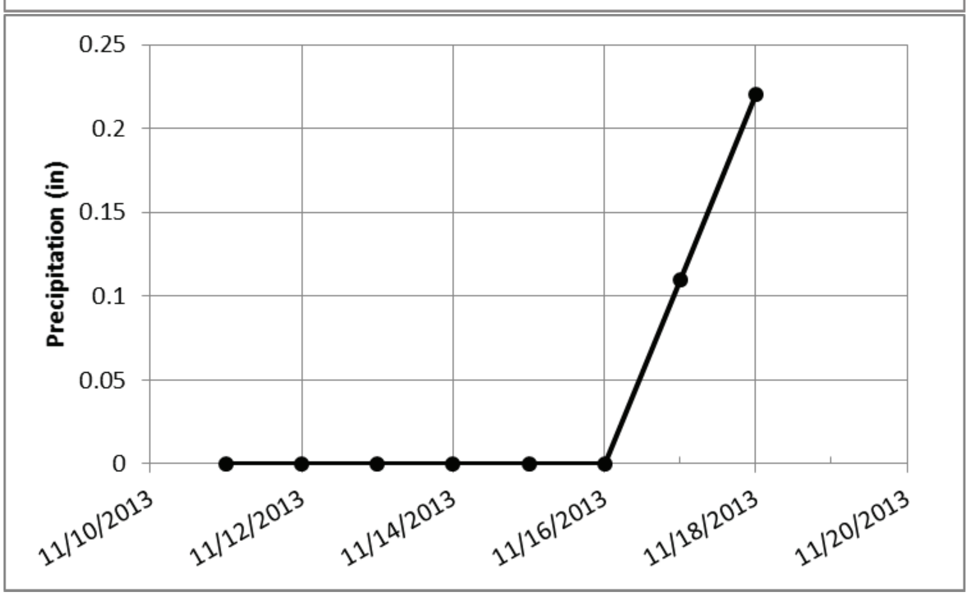

EDT	Max Temp. (F)	Mean Temp. (F)	Min Temp. (F)	Precip. (in)	Events
12/12/2013	28	20	12	0	
12/13/2013	32	26	19	0	
12/14/2013	34	24	15	0.04	Fog-Snow
12/15/2013	39	34	30	0.65	Rain
12/16/2013	32	26	17	0	
12/17/2013	25	18	12	0.01	Fog-Rain-Snow
12/18/2013	35	28	21	0	
12/19/2013	45	36	28	0	

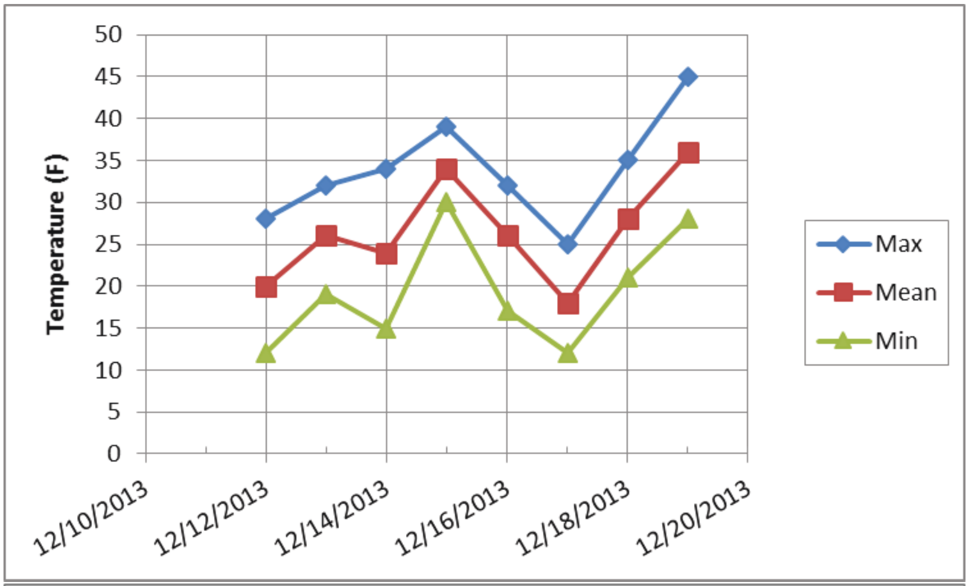

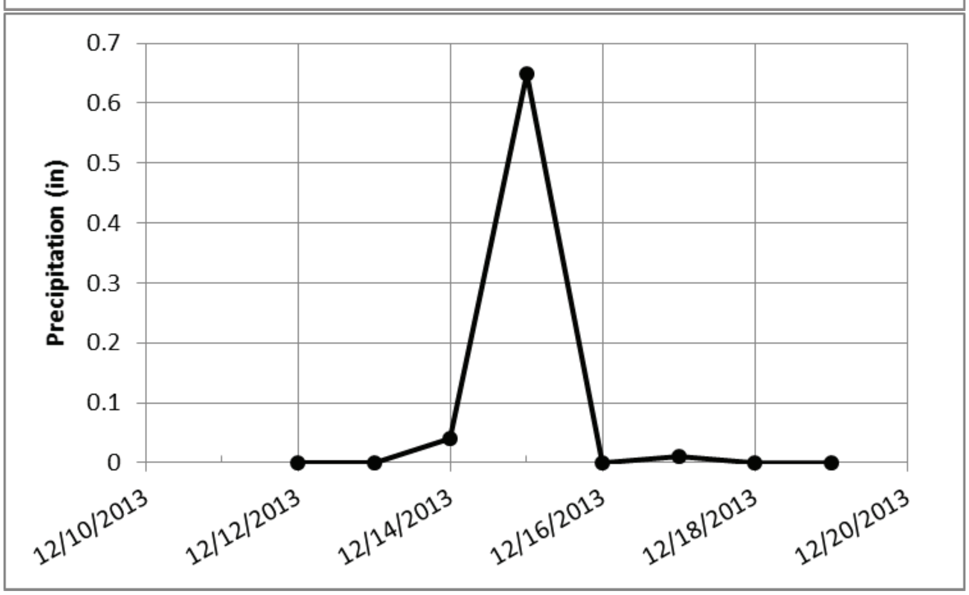

EDT	Max Temp. (F)	Mean Temp. (F)	Min Temp. (F)	Precip. (in)	Events
3/11/2014	53	44	36	0	
3/12/2014	52	44	37	0.53	Rain
3/13/2014	46	31	16	0.03	Rain-Snow
3/14/2014	39	26	16	0	
3/15/2014	55	46	39	0.01	Rain
3/16/2014	39	34	28	0	
3/17/2014	33	26	19	0	
3/18/2014	39	28	17	0	

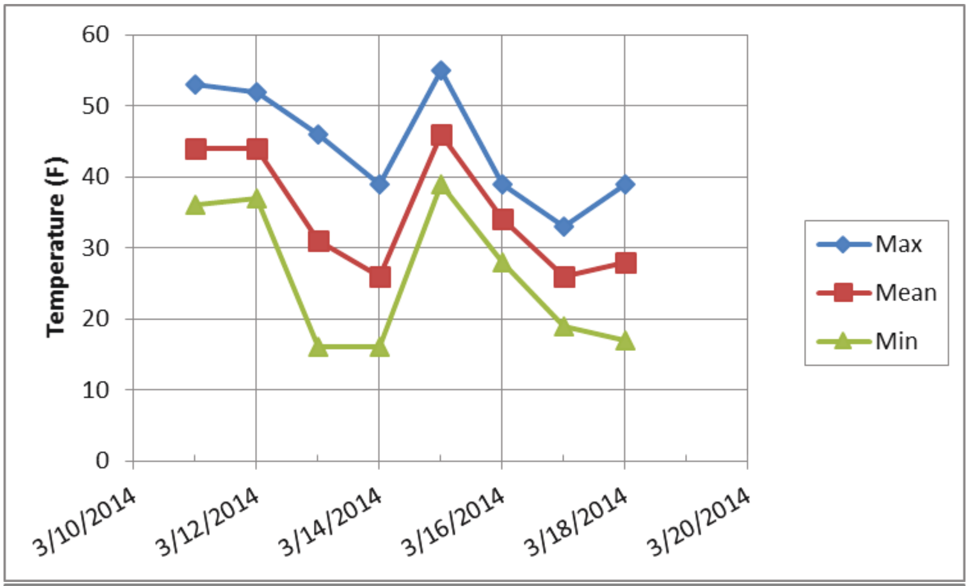

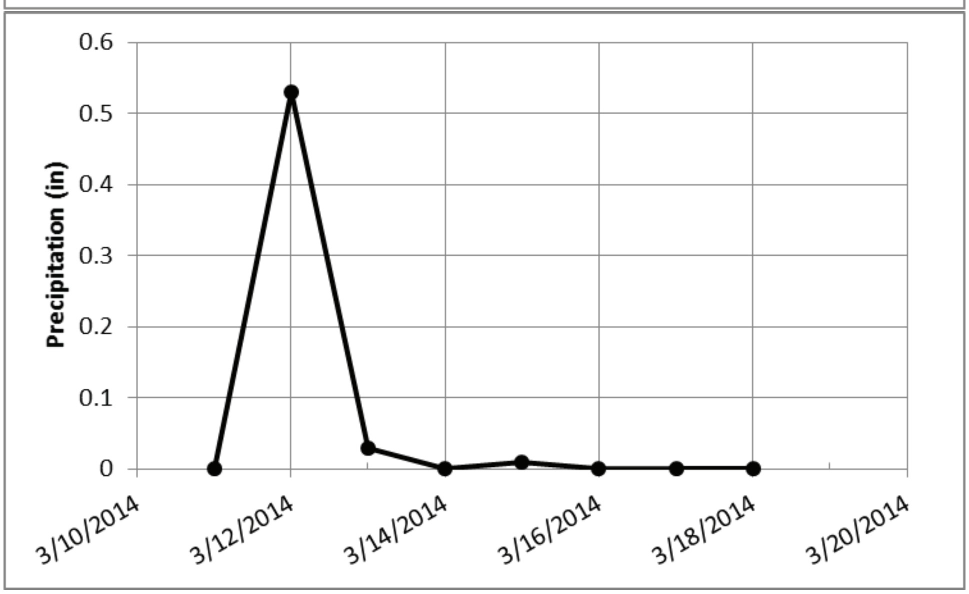

EDT	Max Temp. (F)	Mean Temp. (F)	Min Temp. (F)	Precip. (in)	Events
4/2/2014	48	38	30	0	
4/3/2014	61	46	30	0	
4/4/2014	48	42	39	0.11	Rain
4/5/2014	54	46	39	0.09	Rain
4/6/2014	51	42	34	0	
4/7/2014	48	40	32	0.21	Rain
4/8/2014	54	49	45	0.88	Fog-Rain
4/9/2014	60	50	39	0	

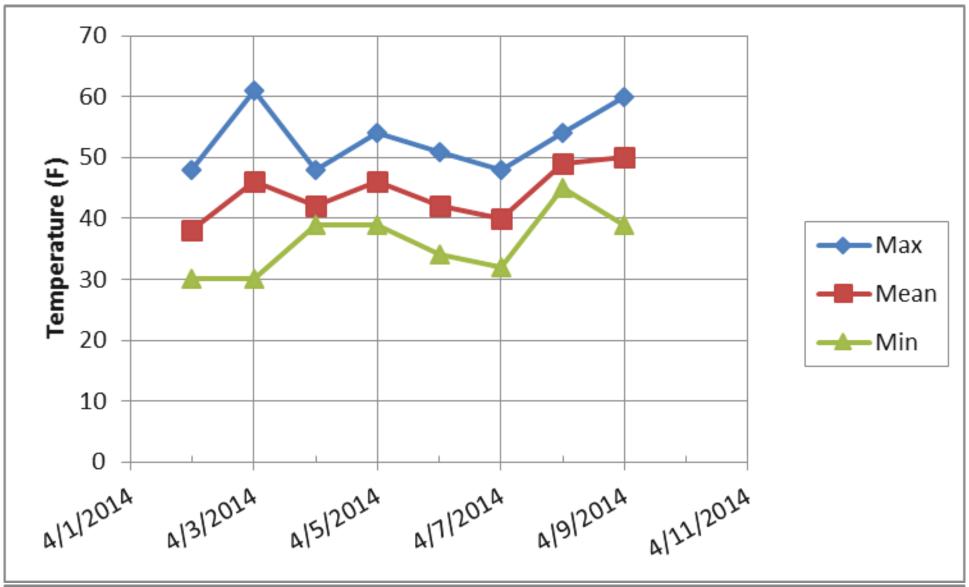

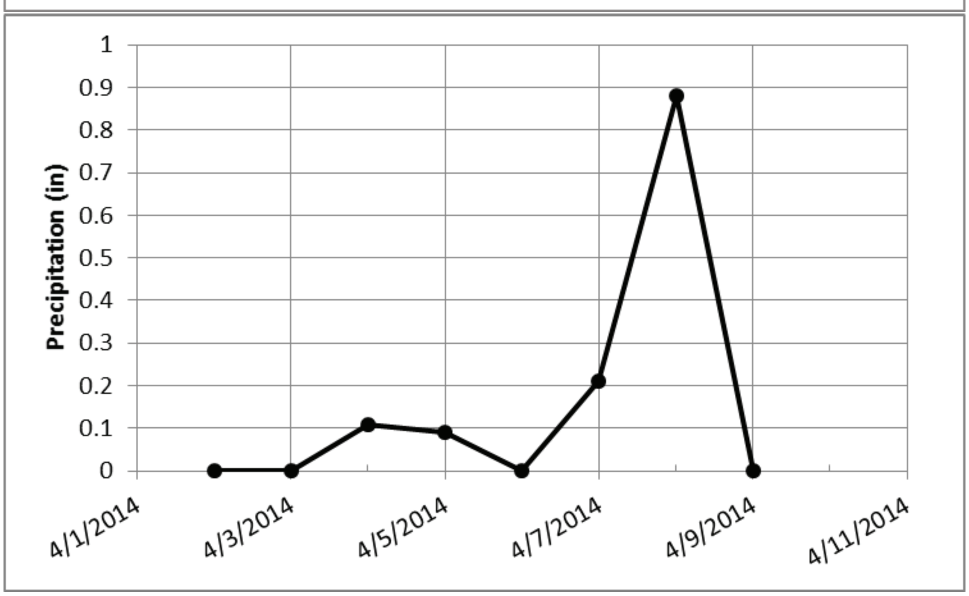

EDT	Max Temp. (F)	Mean Temp. (F)	Min Temp. (F)	Precip. (in)	Events
4/3/2014	61	46	30	0	
4/4/2014	48	42	39	0.11	Rain
4/5/2014	54	46	39	0.09	Rain
4/6/2014	51	42	34	0	
4/7/2014	48	40	32	0.21	Rain
4/8/2014	54	49	45	0.88	Fog-Rain
4/9/2014	60	50	39	0	
4/10/2014	50	40	30	0	

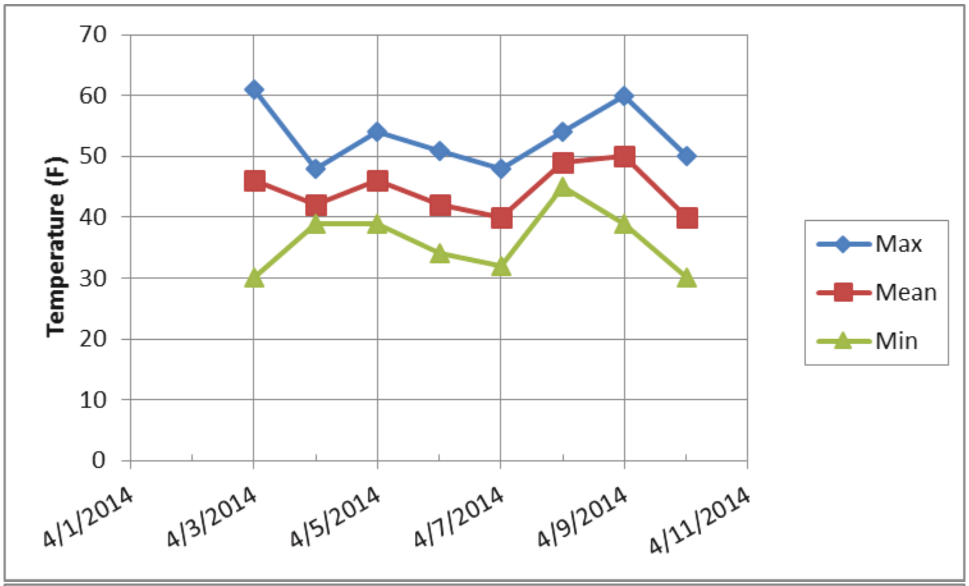

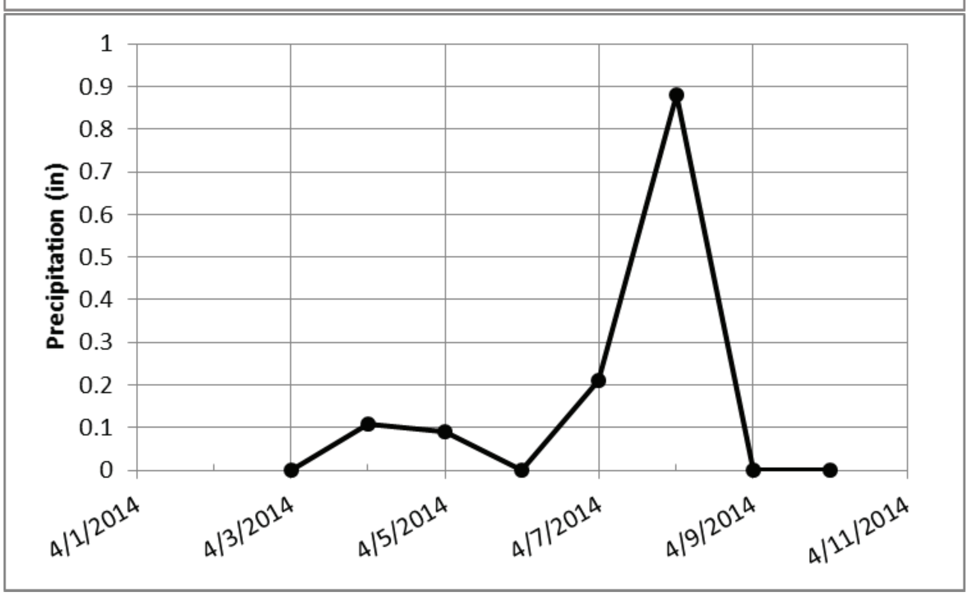

Appendix C.
DCP Analysis

DCP 1
MP 155-41 (Site 2)
Centerline

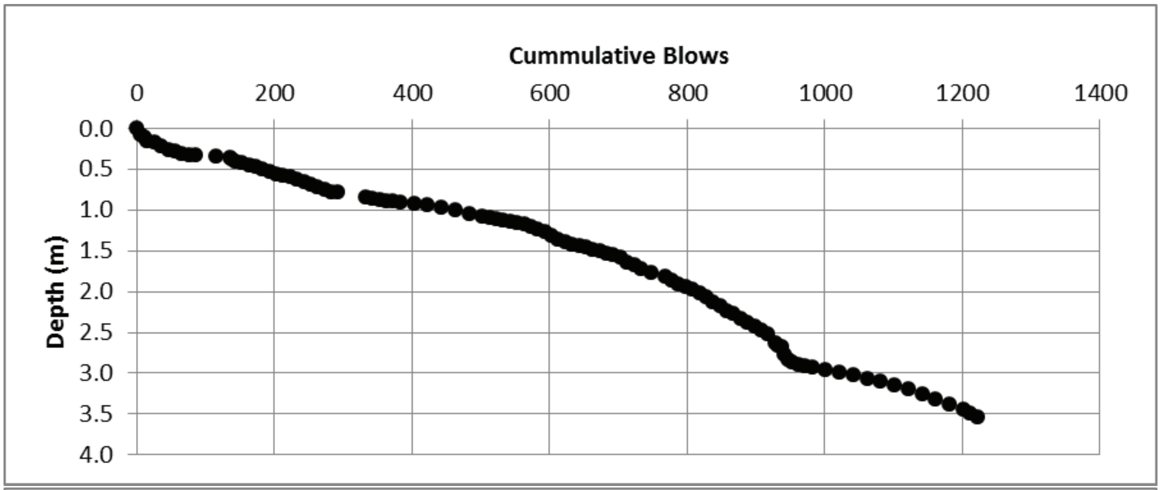

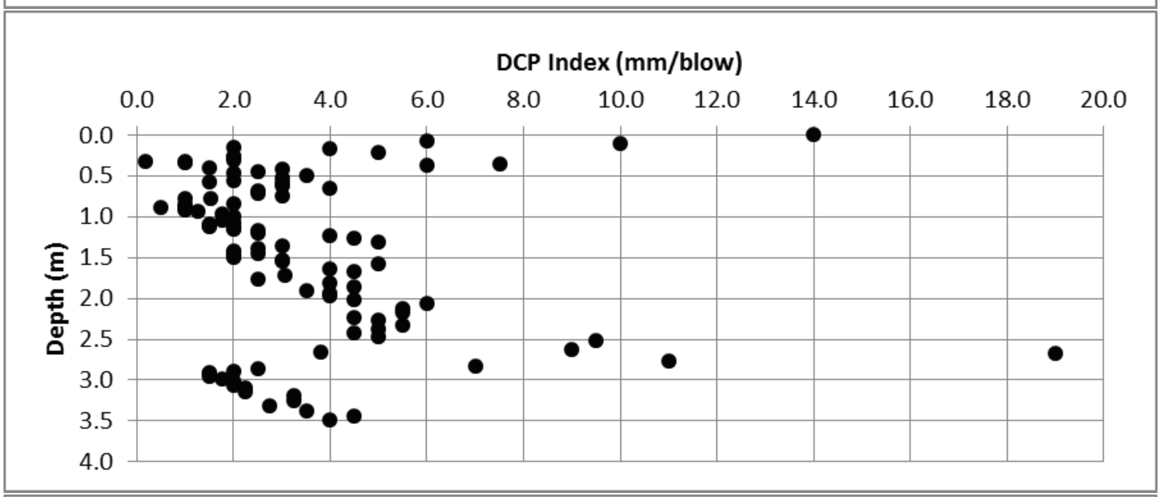

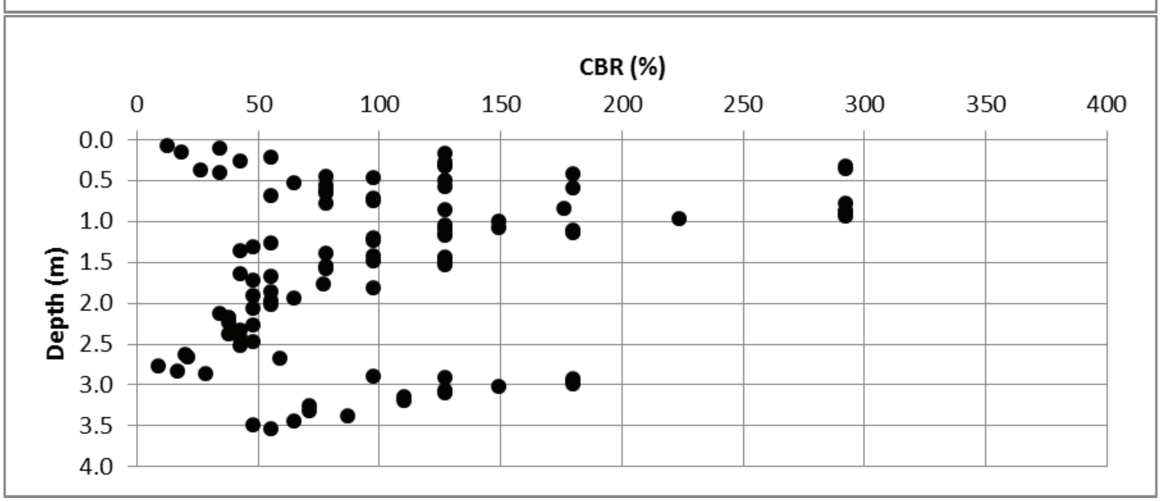

DCP 2
MP 155-41 (Site 2)
Embankment

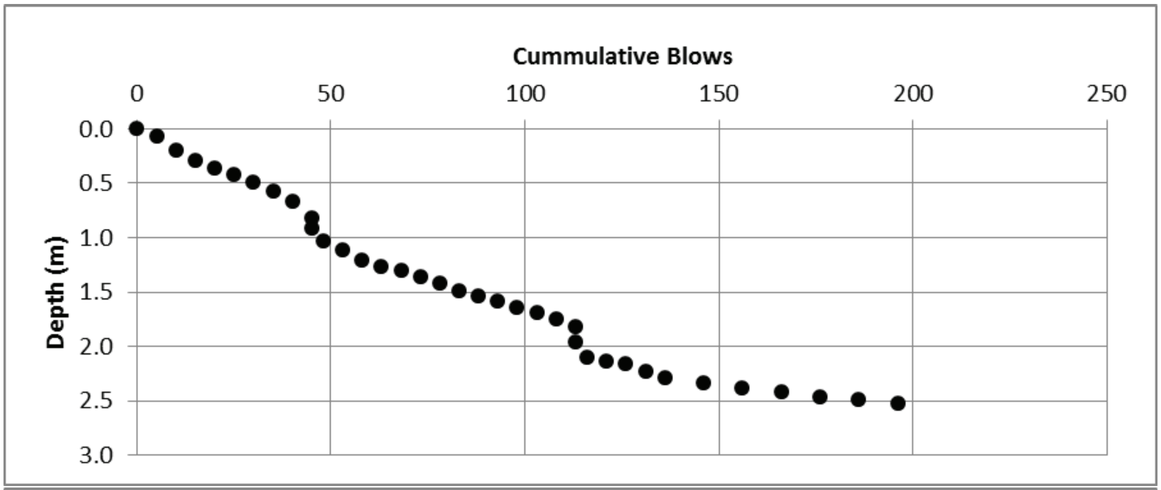

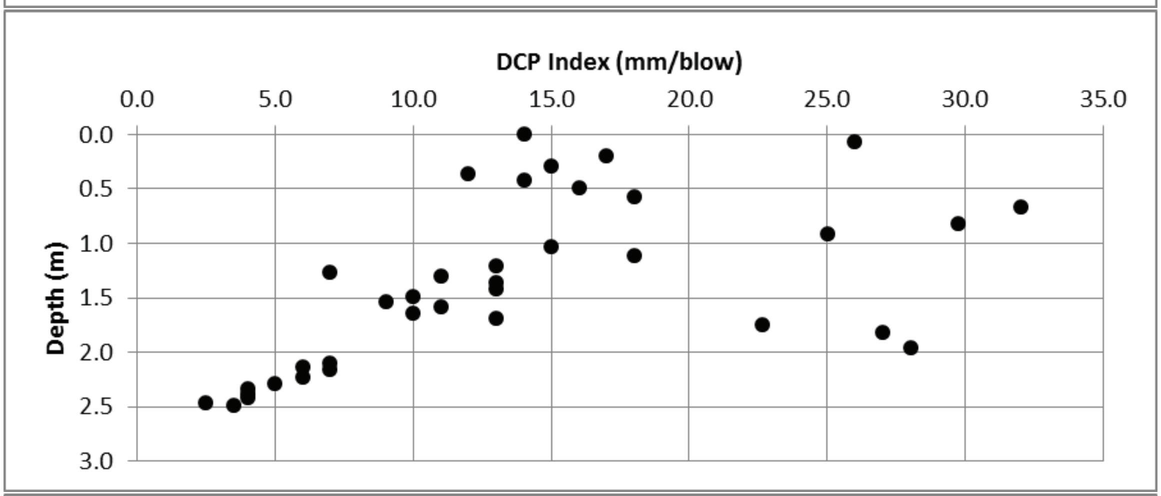

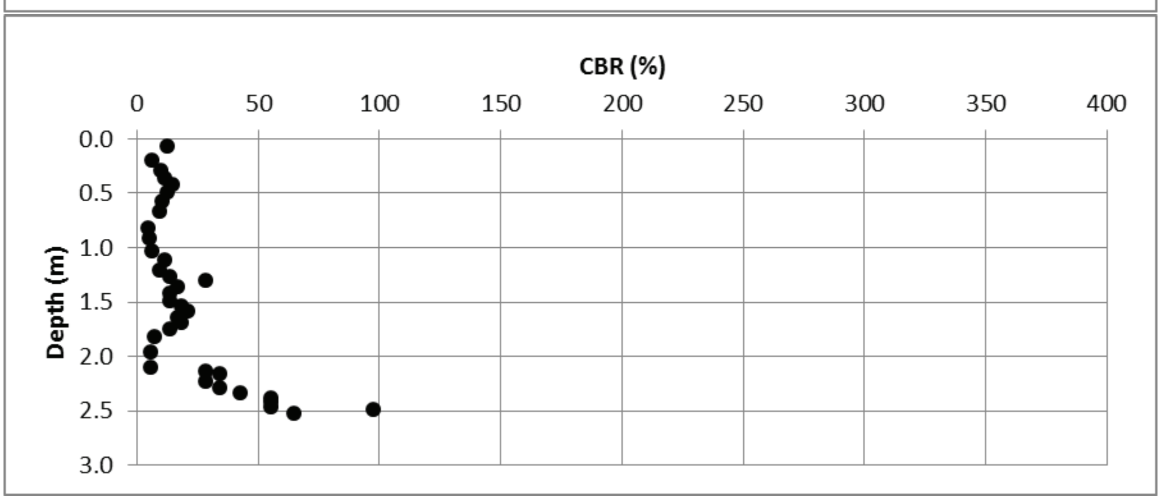

DCP 3
MP 155-41 (Site 2)
Swamp

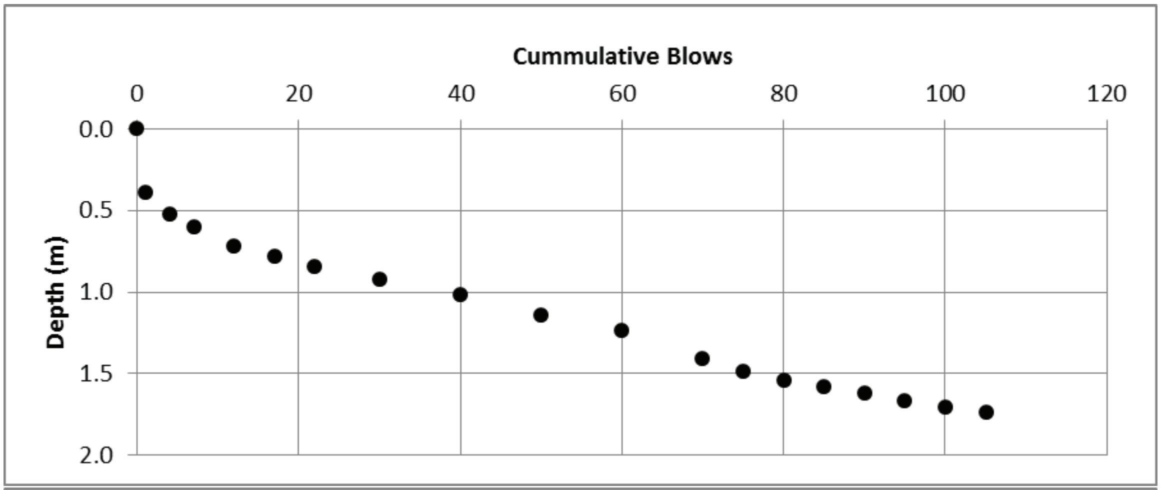

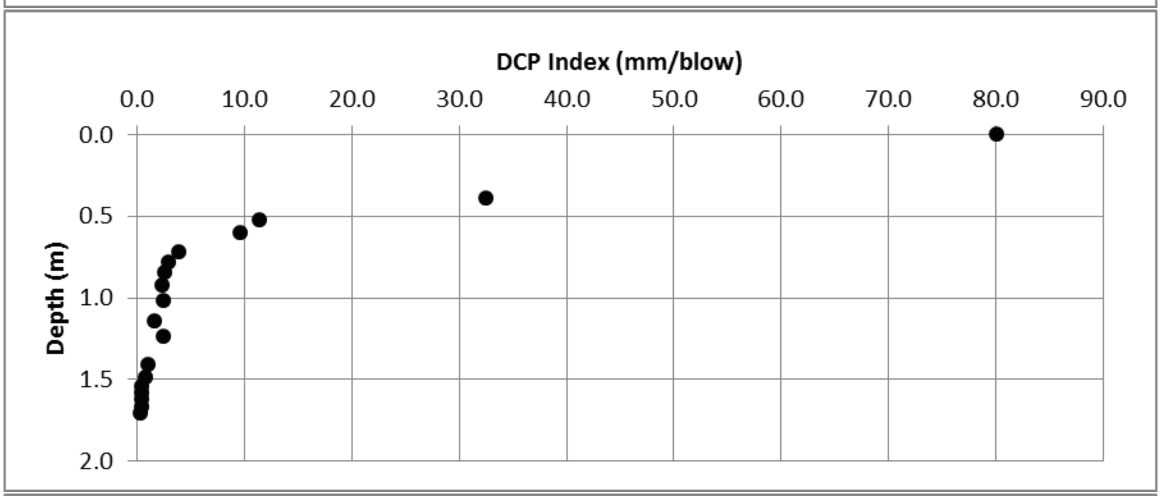

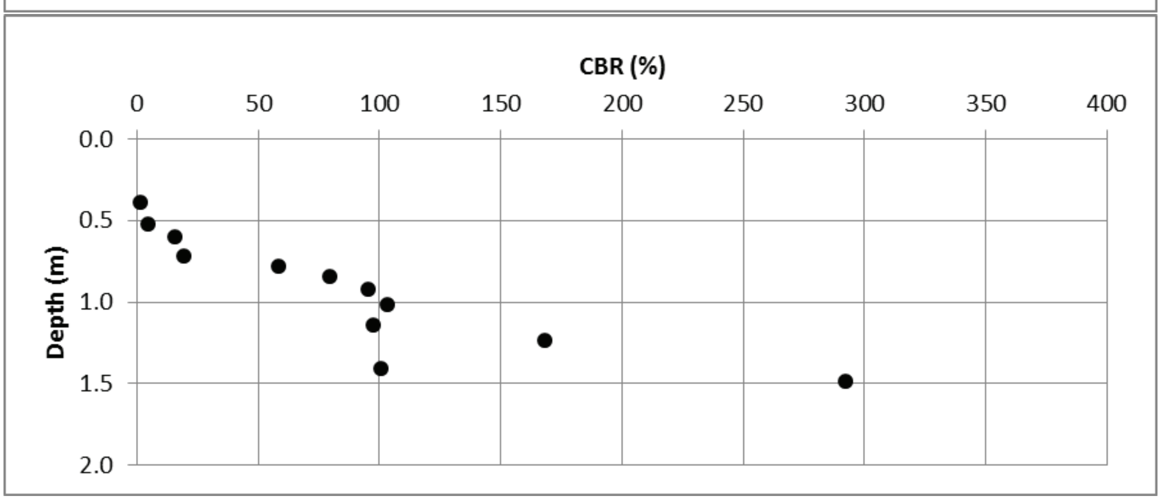

DCP 4
MP 156-23 (Site 1)
Centerline

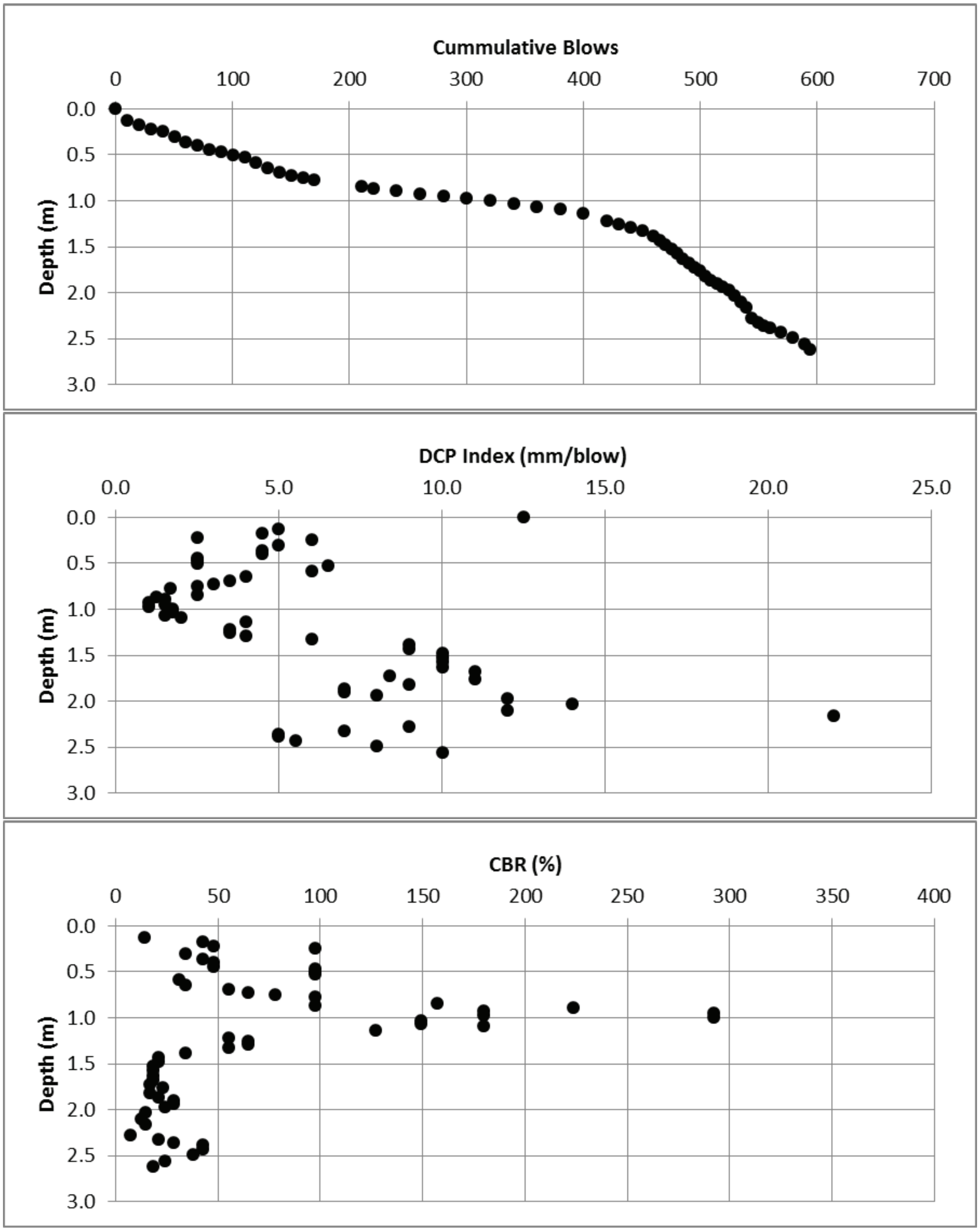

DCP 5
MP 156-23 (Site 1)
Embankment

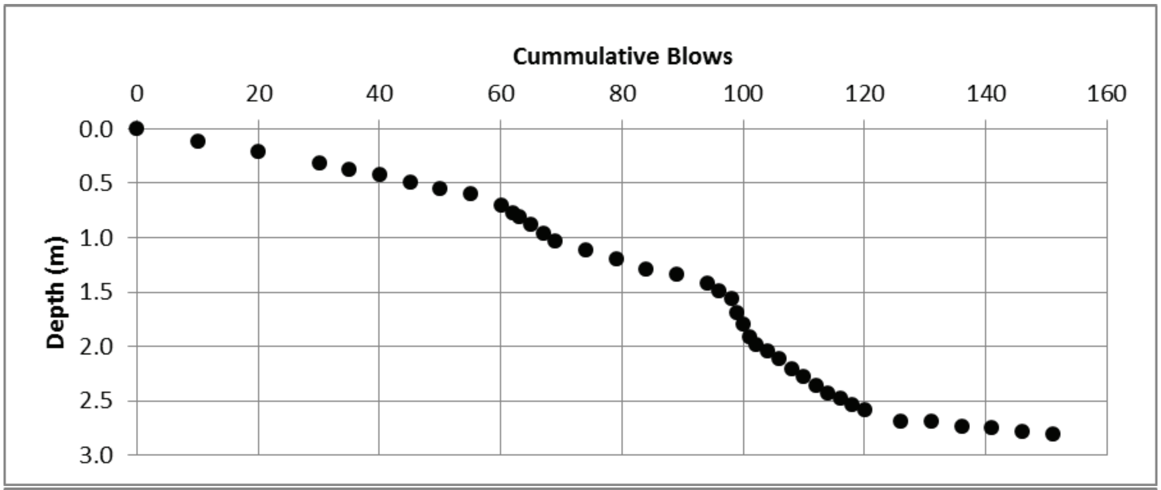

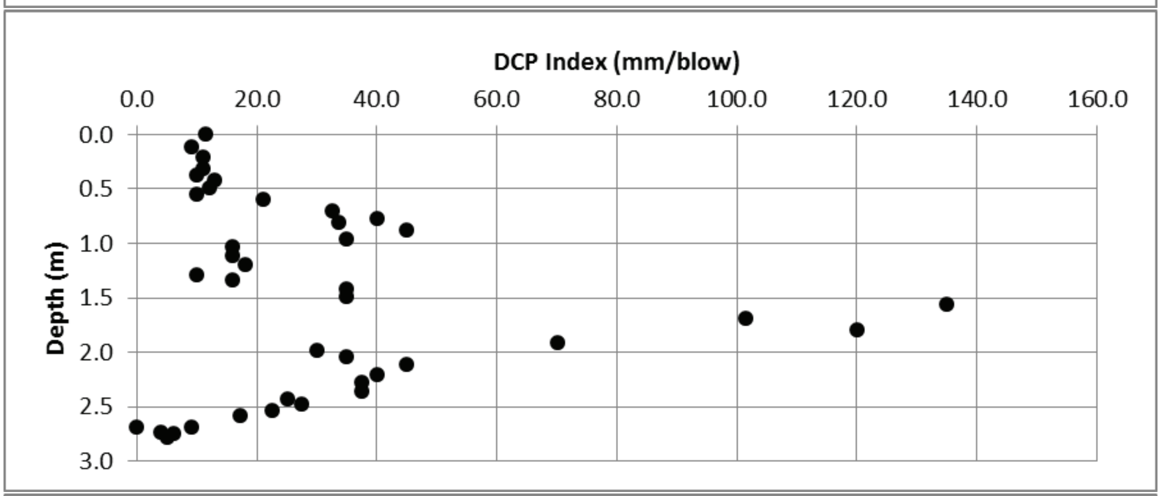

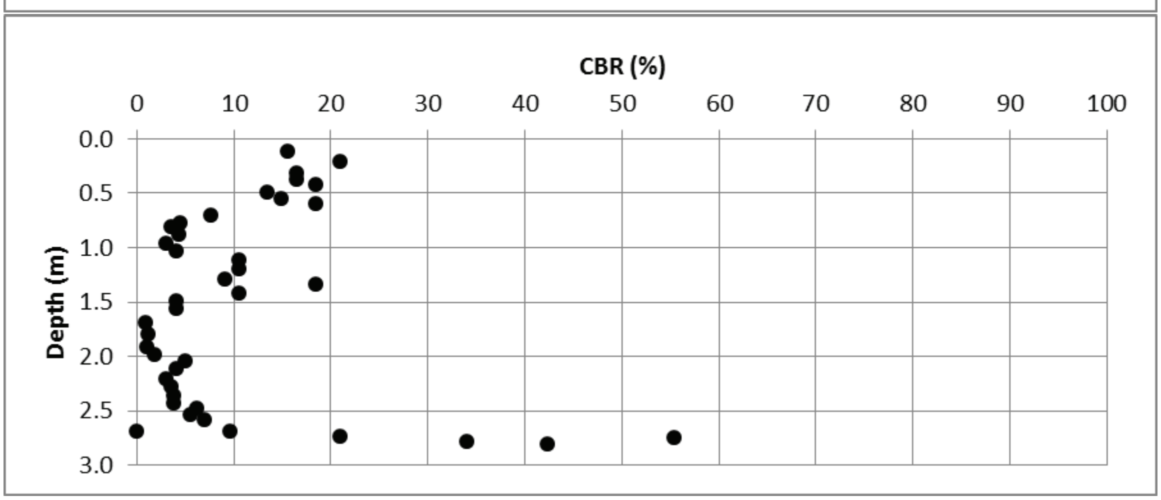

DCP 6
MP 156-23 (Site 1)
Swamp

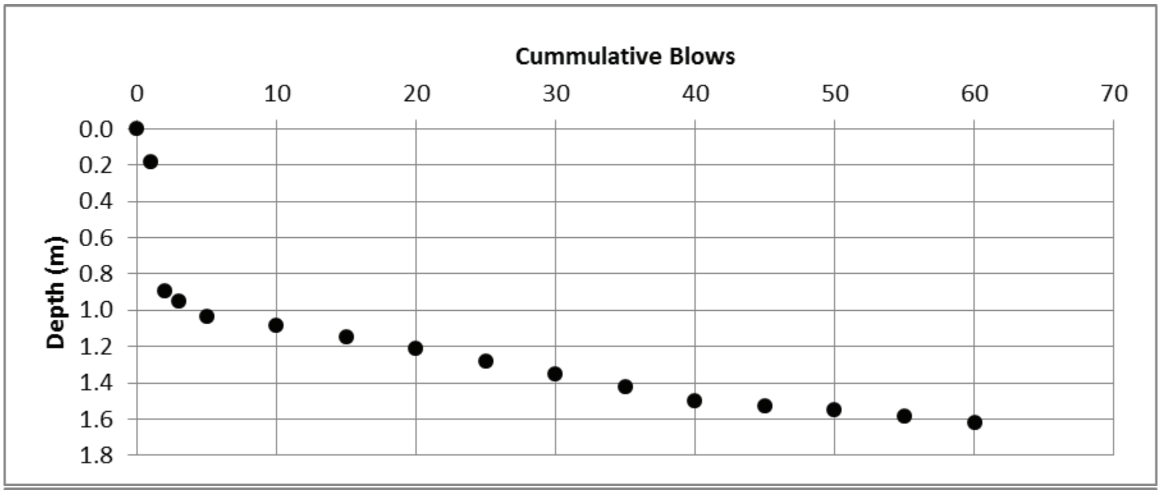

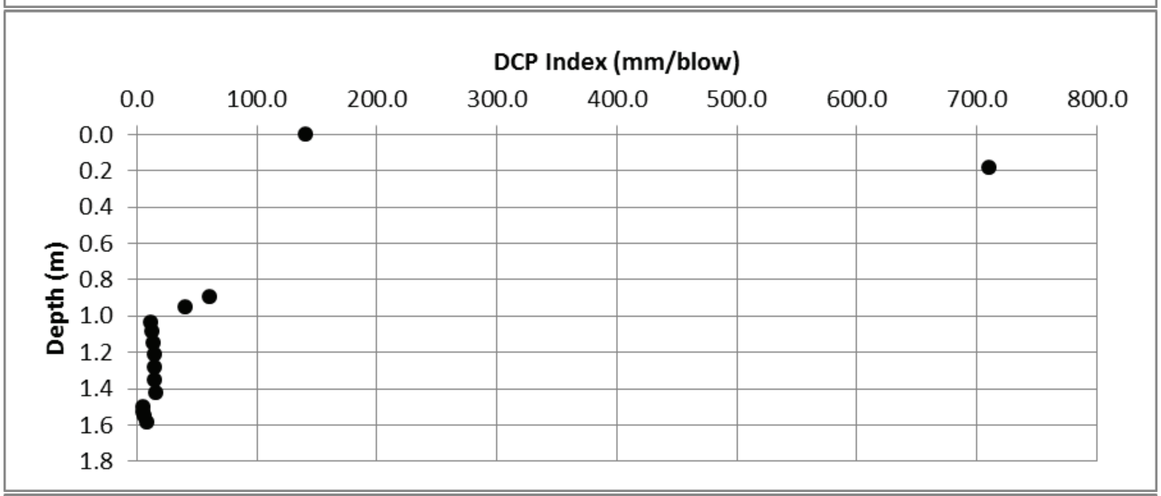

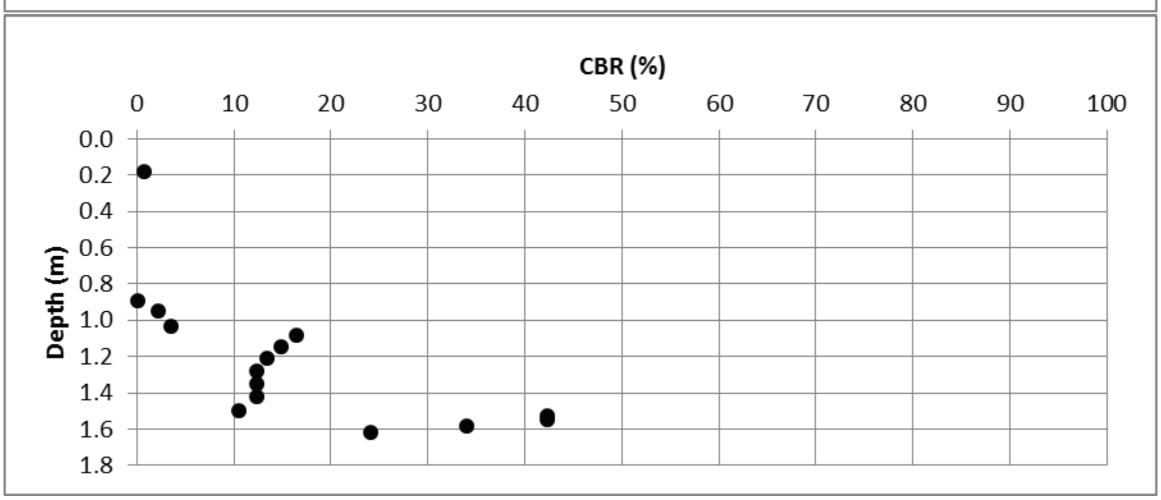

DCP 7
MP 156-23 (Site 1)
Embankment

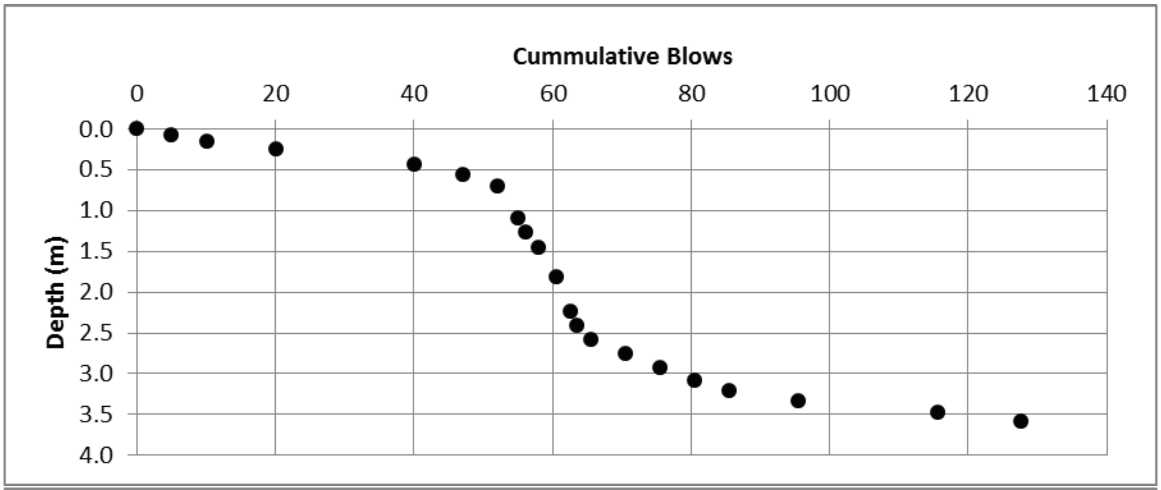

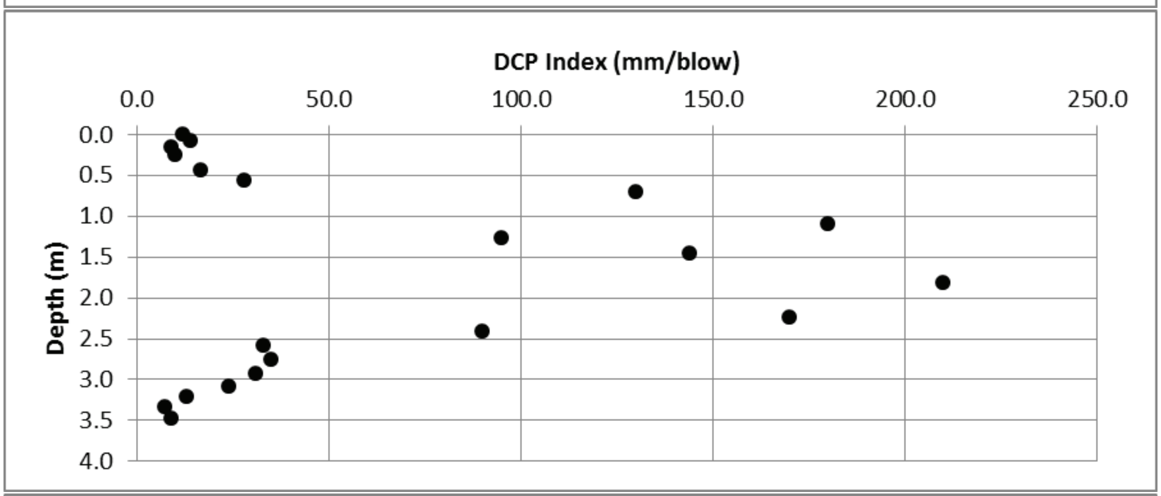

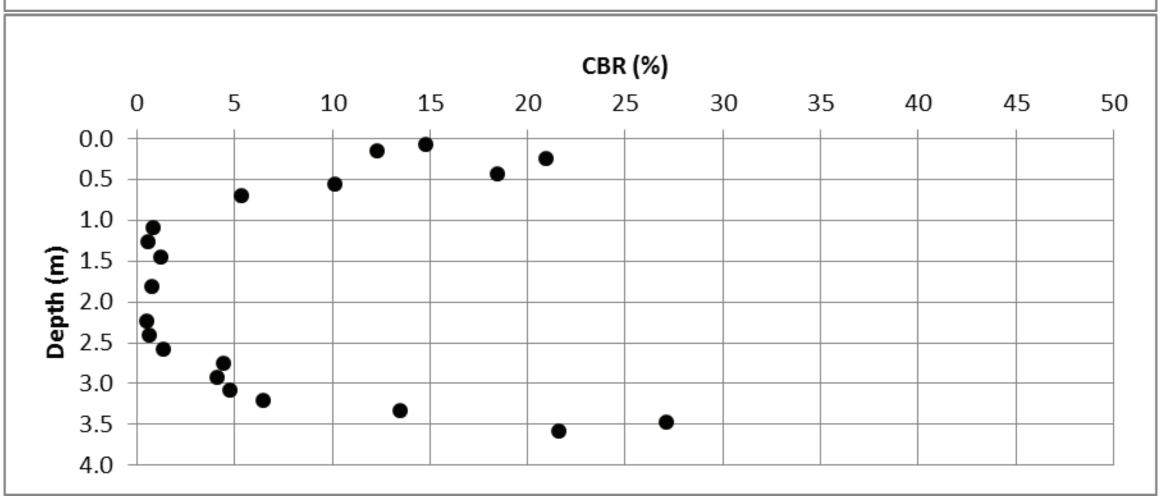

DCP 8
MP 156-23 (Site 1)
Swamp

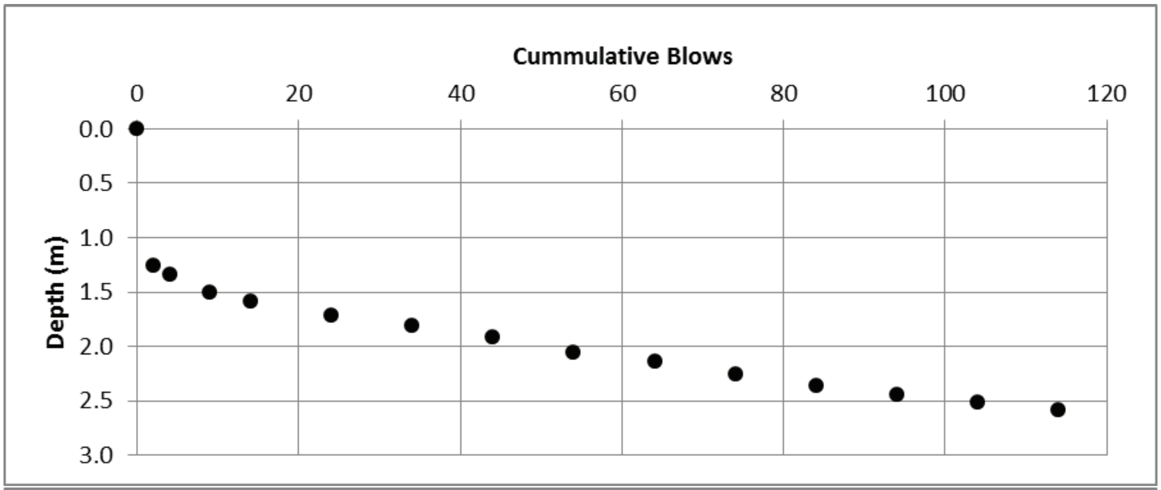

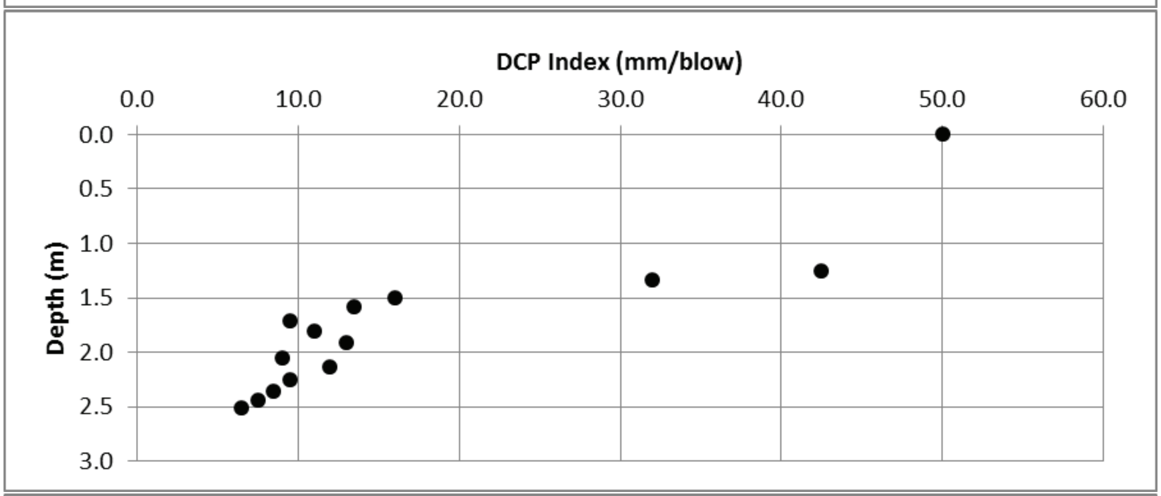

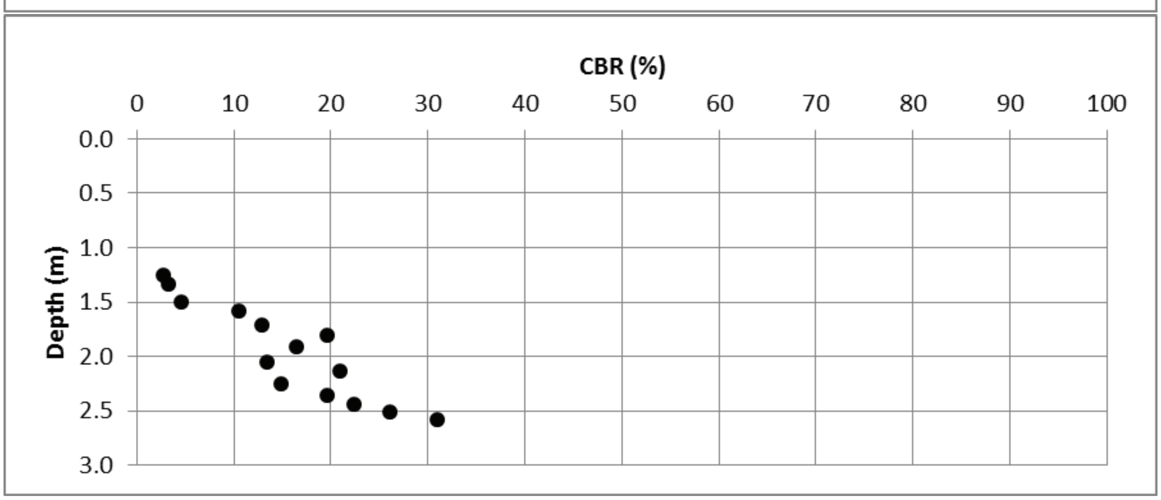

DCP 9
MP 155-41 (Site 2)
Embankment

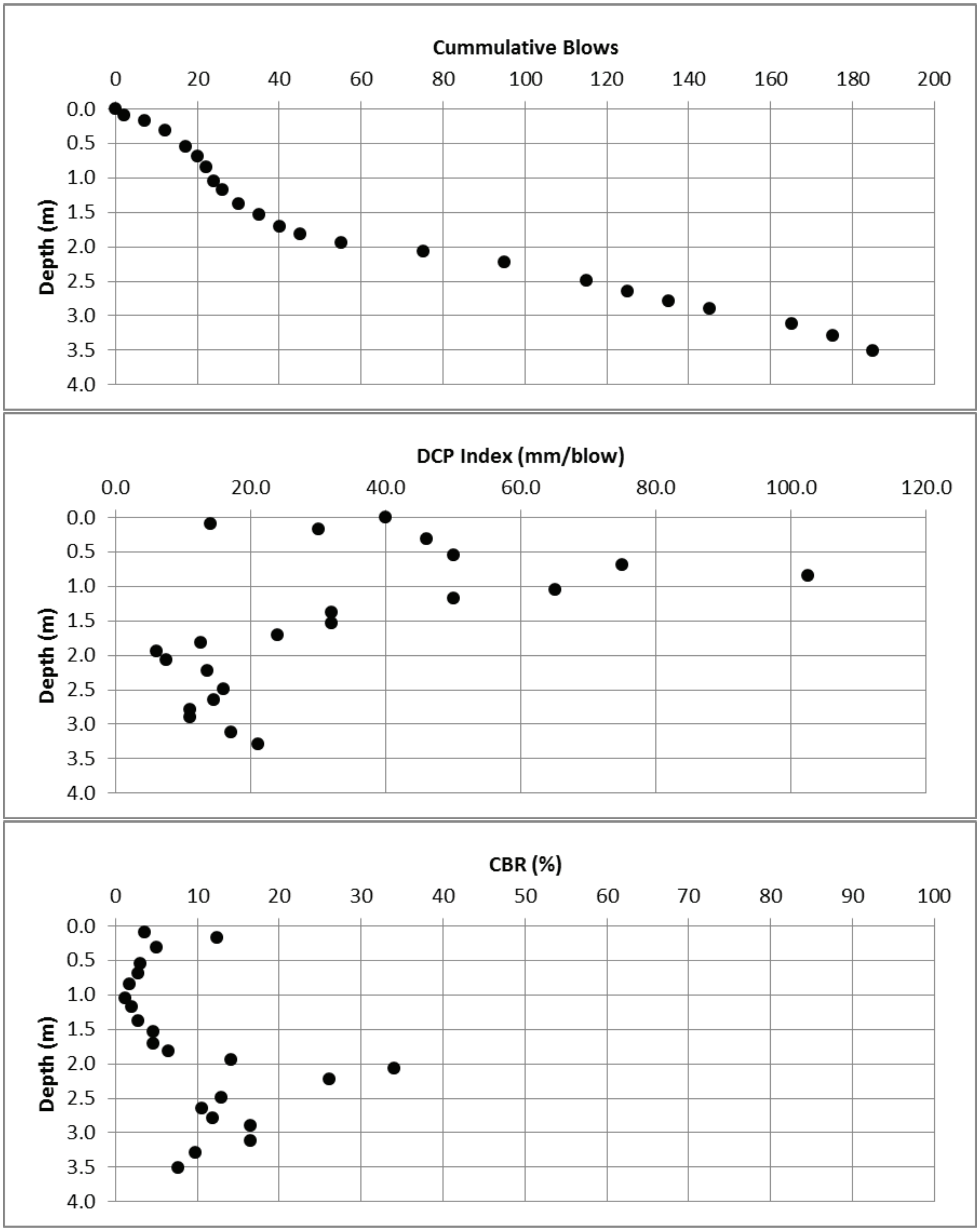

DCP 10
MP 155-41 (Site 2)
Swamp

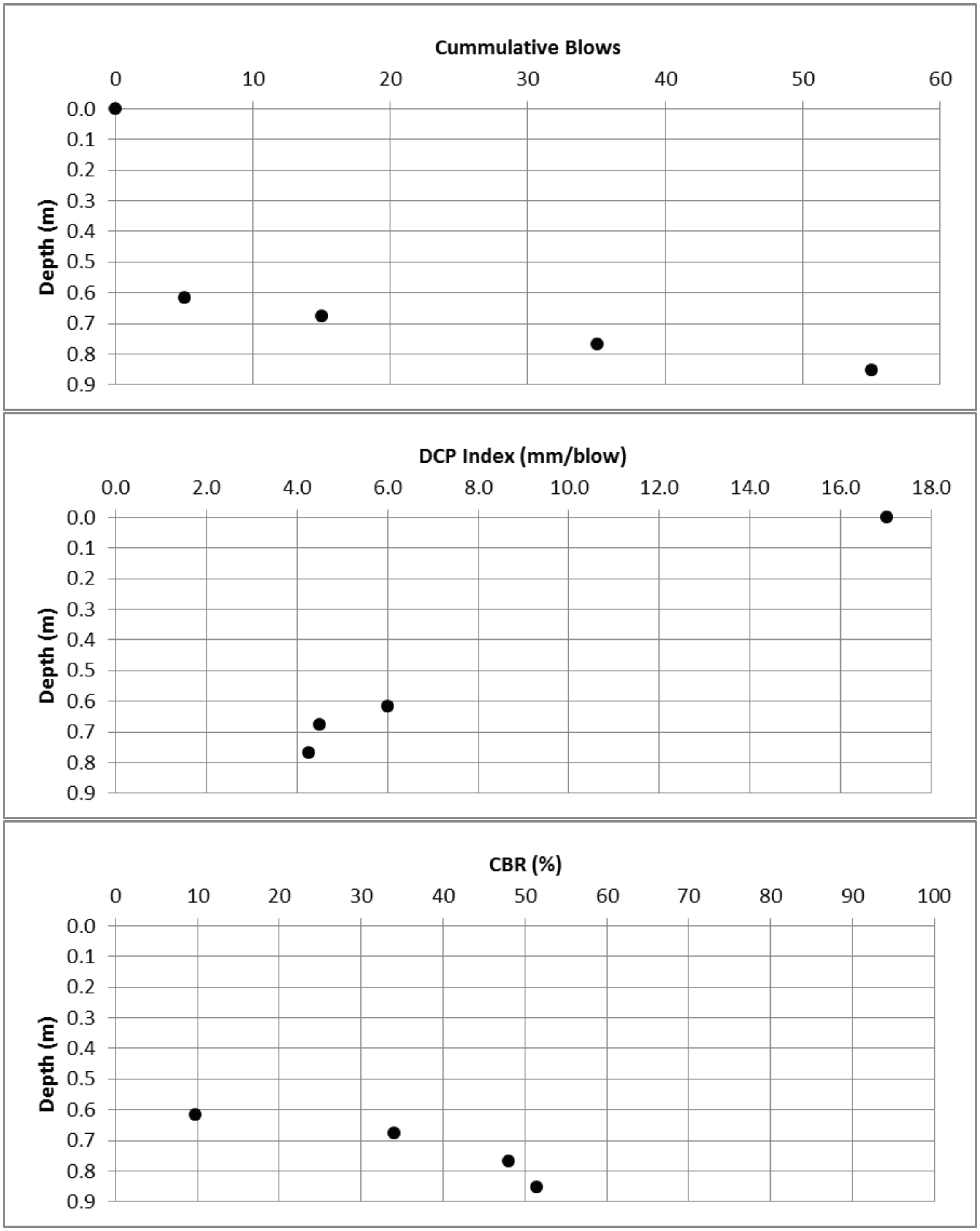

DCP 11
MP 155-41 (Site 2)
Swamp

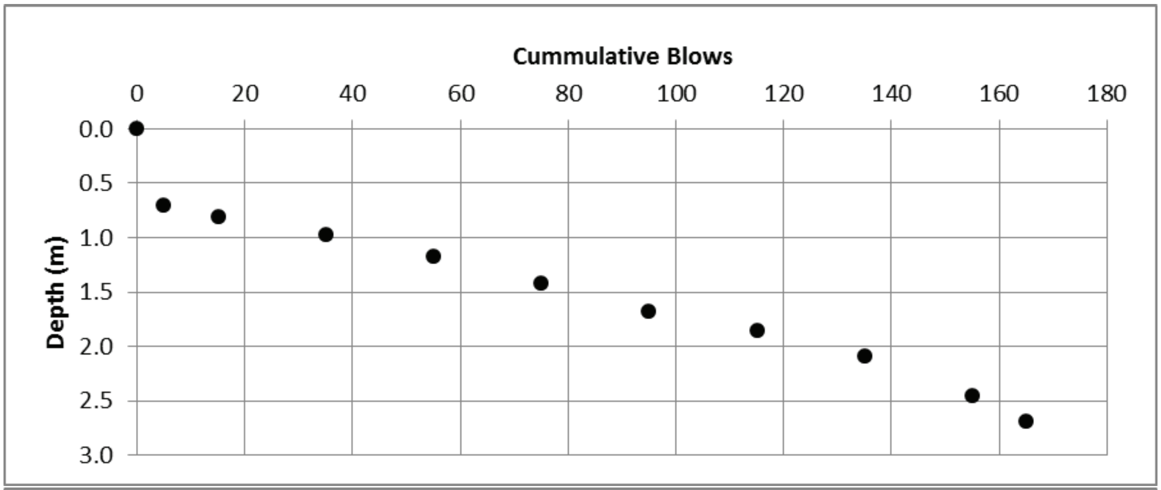

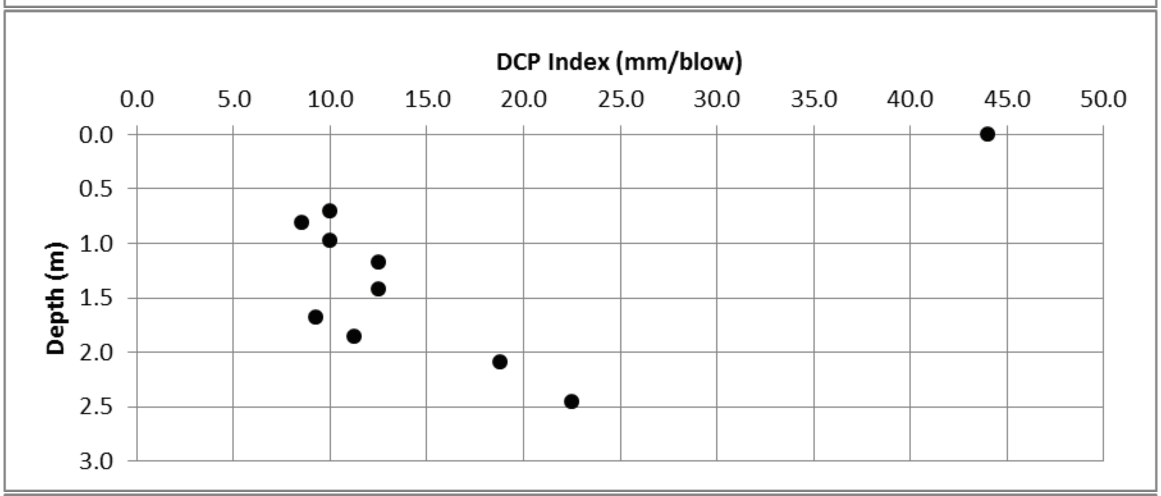

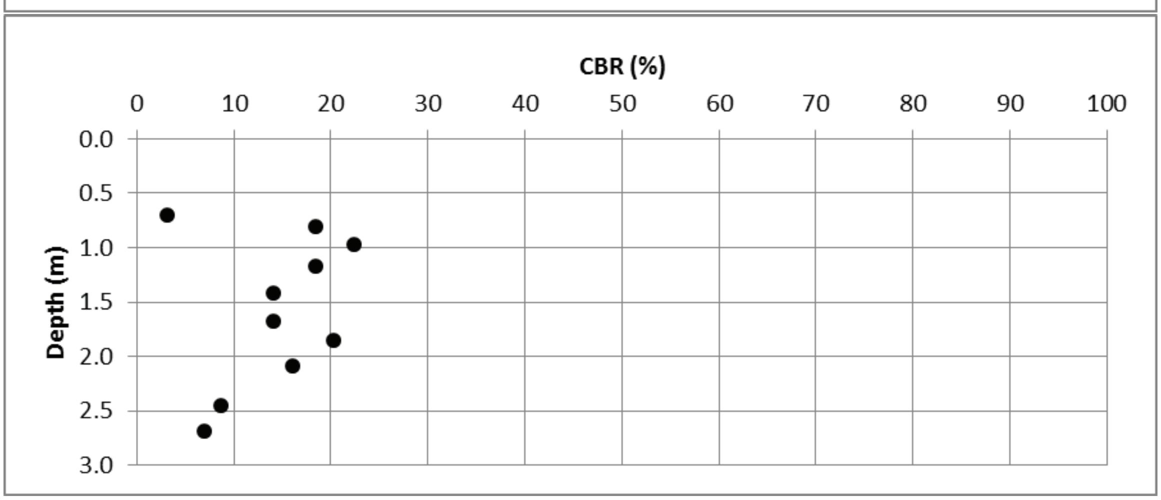

Appendix D.
Laboratory Test Results

Tube No.	Sample Depth	**ρ**	v_s	G_{max}	**E**	**w**	S_u	S_u
(-)	(m)	(g/cm^3)	(m/s)	(kPa)	(kPa)	(%)	(kPa)	(kPa)
1-3	0.05-0.13	1.20	29.4	1037	3008	384	4.0	5.6
1-3	0.13-0.21	1.13	28.2	899	2606	204	5.7	6.2
1-3	0.21-0.29	1.02	21.5	471	1367	215	6.1	13.9
1-4	0.23-0.30	1.07	24.2	627	1817	405	4.2	7.1
1-5	0.08-0.15	1.42	27.7	1090	3160	70	5.6	9.2
1-5	0.18-0.25	1.30	24.4	774	2245	161	4.9	4.8
1-6	0.08-0.15	1.23	31.7	1236	3584	131	5.7	14.5
1-6	0.15-0.23	1.06	25.1	668	1937	376	5.2	11.4
1-6	0.23-0.30	1.06	17.1	310	899	487	4.4	11.9

Date:						
Tube No:	1-3					
Sample Depth:	0.05-0.13 m					
	Wt. Tube+Sample (g):	578.65	Tube Dia. (cm):		7.270	
	Wt. Tube (g):	217.35	Tube Length (cm):		7.699	
	Wt. Sample (g):	361.30	Volume (cm^3):		319.6	
	ρ (g/cm^3):	1.13	ν (Assumed):		0.45	

ΔL	f	Δt	L_{tt}/λ	v_s	G_{max}	E
(mm)	(Hz)	(ms)	(-)	(m/s)	(kPa)	(kPa)
51.88	500	2.139	1.1	24.3	665	1928
51.88	750	1.897	1.4	27.3	845	2452
51.88	1000	1.827	1.8	28.4	912	2643
51.88	1500	1.706	2.6	30.4	1045	3032
36.4	750	1.385	1.0	26.3	781	2264
36.4	1000	1.139	1.1	32.0	1154	3348
36.4	1500	1.297	1.9	28.1	890	2582
36.4	2000	1.26	2.5	28.9	943	2736
			Average:	28.2	905	2623

Pennetration	Cone Mass	Cone Angle	k	S_u
(mm)	(g)	(deg)	(-)	(kPa)
4.56	60	60	0.27	7.64
5.81	60	60	0.27	4.71
4.53	60	60	0.27	7.74
7.08	60	60	0.27	3.17
5.94	60	60	0.27	4.50
4.16	60	60	0.27	9.18
			Average:	6.2

Vane	q_u read.	q_u	q_u	S_u
(-)	(kg/cm2)	(kg/cm2)	(kPa)	(kPa)
0.2	0.60	0.12	11.8	5.9
0.2	0.57	0.11	11.2	5.6
			Average:	5.7

Test	FC-1	FC-2	TV-1	TV-2
Soil+Tare (g)	27.88	11.03	11.43	16.80
DrySoil+Tare (g)	9.82	4.38	4.37	5.97
Wt. Water (g)	18.06	6.65	7.06	10.83
Wt. Tare (g)	1.31	1.17	1.12	1.15
Wt. DrySoil (g)	8.51	3.21	3.25	4.82
w (%)	212.2	207.2	217.2	224.7

Date:	
Tube No:	1-3
Sample Depth:	0.13-0.20 m

Wt. Tube+Sample (g):	571.61	Tube Dia. (cm):	7.270
Wt. Tube (g):	222.62	Tube Length (cm):	7.040
Wt. Sample (g):	348.99	Volume (cm^3):	292.2
ρ (g/cm^3):	1.19	ν (Assumed):	0.45

ΔL	**f**	**Δt**	**L_{tt}/λ**	**v_s**	**G_{max}**	**E**
(mm)	(Hz)	(ms)	(-)	(m/s)	(kPa)	(kPa)
56.97	750	1.737	1.3	32.8	1285	3725
56.97	1000	1.728	1.7	33.0	1298	3764
56.97	1500	1.663	2.5	34.3	1401	4064
47.19	500	2.155	1.1	21.9	573	1661
47.19	750	1.904	1.4	24.8	734	2127
47.19	1000	1.782	1.8	26.5	837	2429
47.19	1500	1.655	2.5	28.5	971	2816
			Average:	28.8	1014	2941

Pennetration	**Cone Mass**	**Cone Angle**	**k**	**S_u**
(mm)	(g)	(deg)	(-)	(kPa)
4.03	60	60	0.27	9.79
6.51	60	60	0.27	3.75
5.77	60	60	0.27	4.77
5.34	60	60	0.27	5.57
2.51	60	60	0.27	25.23
3.24	60	60	0.27	15.14
5.41	60	60	0.27	5.43
5.37	60	60	0.27	5.51
			Average:	9.4

Vane	**q_u read.**	**q_u**	**q_u**	**S_u**
(-)	(kg/cm2)	(kg/cm2)	(kPa)	(kPa)
0.2	0.44	0.09	8.6	4.3
0.2	0.38	0.08	7.5	3.7
			Average:	4.0

Test	FC-1	FC-2	TV-1	TV-2
Wt. Soil+Tare (g)	9.54	12.53	18.92	16.30
Wt. DrySoil+Tare (g)	3.54	3.26	5.82	3.84
Wt. Water (g)	6	9.27	13.1	12.46
Wt. Tare (g)	1.33	1.33	1.32	1.32
Wt. DrySoil (g)	2.21	1.93	4.5	2.52
w (%)	271.5	480.3	291.1	494.4

Date:	6/5/2014					
Tube No:	1-3					
Sample Depth:	0.20-0.28 m					

	Wt. Tube+Sample (g):	535.83	Tube Dia. (cm):		7.280	
	Wt. Tube (g):	214.02	Tube Length (cm):		7.570	
	Wt. Sample (g):	321.81	Volume (cm^3):		315.1	
	ρ (g/cm^3):	1.02	ν (Assumed):		0.45	

ΔL	**f**	**Δt**	**L_{tt}/λ**	**v_s**	**G_{max}**	**E**
(mm)	(Hz)	(ms)	(-)	(m/s)	(kPa)	(kPa)
54.75	400	2.787	1.1	19.6	394	1143
54.75	500	2.684	1.3	20.4	425	1232
54.75	600	2.48	1.5	22.1	498	1443
54.75	750	2.164	1.6	25.3	654	1896
54.75	1000	2.656	2.7	20.6	434	1259
42.32	500	2.155	1.1	19.6	394	1142
42.32	750	2.063	1.5	20.5	430	1246
42.32	1000	1.97	2.0	21.5	471	1367
42.32	1250	1.905	2.4	22.2	504	1462
42.32	1500	1.849	2.8	22.9	535	1552
			Average:	21.5	473.9	1374.2

Pennetration	**Cone Mass**	**Cone Angle**	**k**	**S_u**
(mm)	(g)	(deg)	(-)	(kPa)
3.01	60	60	0.27	17.54
2.71	60	60	0.27	21.64
3.7	60	60	0.27	11.61
4.27	60	60	0.27	8.72
3.51	60	60	0.27	12.90
3.79	60	60	0.27	11.06
			Average:	13.9

Vane	**q_u read.**	**q_u**	**q_u**	**S_u**
(-)	(kg/cm2)	(kg/cm2)	(kPa)	(kPa)
0.2	0.57	0.11	11.2	5.6
0.2	0.67	0.13	13.1	6.6
			Average:	6.1

Test	FC-1	FC-2	TV-1	TV-2
Wt. Soil+Tare (g)	27.88	11.03	11.43	16.80
Wt. DrySoil+Tare (g)	9.82	4.38	4.37	5.97
Wt. Water (g)	18.06	6.65	7.06	10.83
Wt. Tare (g)	1.31	1.17	1.12	1.15
Wt. DrySoil (g)	8.51	3.21	3.25	4.82

Date:	4/1/2014
Tube No:	1-4
Sample Depth:	0.05-0.13 m

Wt. Tube+Sample (g):	573.33	Tube Dia. (cm):	7.286
Wt. Tube (g):	220.93	Tube Length (cm):	7.888
Wt. Sample (g):	352.40	Volume (cm^3):	328.9
ρ (g/cm^3):	1.07	ν (Assumed):	0.45

ΔL	**f**	**Δt**	**L_{tt}/λ**	**v_s**	**G_{max}**	**E**
(mm)	(Hz)	(ms)	(-)	(m/s)	(kPa)	(kPa)
59.44	400	2.677	1.1	22.2	528	1532
59.44	500	2.573	1.3	23.1	572	1658
59.44	600	2.639	1.6	22.5	544	1576
59.44	700	2.677	1.9	22.2	528	1532
59.44	750	2.499	1.9	23.8	606	1758
44.13	400	2.678	1.1	16.5	291	844
44.13	500	2.482	1.2	17.8	339	982
44.13	600	2.385	1.4	18.5	367	1064
44.13	750	2.269	1.7	19.4	405	1175
44.13	1000	2.037	2.0	21.7	503	1458
44.13	1500	1.827	2.7	24.2	625	1813
			Average:	20.8	468.3	1358.1

Pennetration	**Cone Mass**	**Cone Angle**	**k**	**S_u**
(mm)	(g)	(deg)	(-)	(kPa)
5.11	60	60	0.27	6.09
4.3	60	60	0.27	8.60
5.59	60	60	0.27	5.09
5.53	60	60	0.27	5.20
5	60	60	0.27	6.36
4.34	60	60	0.27	8.44
5.1	60	60	0.27	6.11
3.82	60	60	0.27	10.89
			Average:	7.1

Vane	**q_u read.**	**q_u**	**q_u**	**S_u**
(-)	(kg/cm2)	(kg/cm2)	(kPa)	(kPa)
0.2	0.44	0.09	8.6	4.3
0.2	0.41	0.08	8.0	4.0
			Average:	4.2

Test	FC-1	FC-2	TV-1	TV-2
Wt. Soil+Tare (g)	12.74	12.56	14.69	20.53
Wt. DrySoil+Tare (g)	3.96	3.35	4.11	4.83

Date:	6/4/2014					
Tube No:	1-5					
Sample Depth:	0.08-0.15 m					
	Wt. Tube+Sample (g):	710.79		Tube Dia. (cm):	7.284	
	Wt. Tube (g):	229.97		Tube Length (cm):	8.115	
	Wt. Sample (g):	480.82		Volume (cm^3):	338.1	
	ρ (g/cm^3):	1.42		ν (Assumed):	0.45	

ΔL	f	Δt	L_{tt}/λ	v_s	G_{max}	E
(mm)	(Hz)	(ms)	(-)	(m/s)	(kPa)	(kPa)
61.9	400	2.657	1.1	23.3	772	2238
61.9	500	2.536	1.3	24.4	847	2457
61.9	600	2.397	1.4	25.8	948	2750
61.9	750	2.165	1.6	28.6	1162	3371
61.9	1000	1.951	2.0	31.7	1431	4151
33.68	750	1.338	1.0	25.2	901	2613
33.68	1000	1.199	1.2	28.1	1122	3254
33.68	1250	1.171	1.5	28.8	1176	3412
33.68	1500	1.134	1.7	29.7	1254	3638
33.68	1750	1.097	1.9	30.7	1340	3887
			Average:	27.6	1095.6	3177.2

Pennetration	Cone Mass	Cone Angle	k	S_u
(mm)	(g)	(deg)	(-)	(kPa)
7.37	60	60	0.27	2.93
7.18	60	60	0.27	3.08
5.25	60	60	0.27	5.77
3	60	60	0.27	17.66
3.83	60	60	0.27	10.83
3.25	60	60	0.27	15.05
			Average:	9.2

Vane	q_u read.	q_u	q_u	S_u
(-)	(kg/cm2)	(kg/cm2)	(kPa)	(kPa)
0.2	0.55	0.11	10.8	5.4
0.2	0.58	0.12	11.4	5.7
			Average:	5.5

Test	FC-1	FC-2	TV-1	TV-2
Wt. Soil+Tare (g)	21.04	27.35	14.63	20.85
Wt. DrySoil+Tare (g)	12.49	18.6	8.17	13.67
Wt. Water (g)	8.55	8.75	6.46	7.18
Wt. Tare (g)	1.29	1.16	1.29	1.28
Wt. DrySoil (g)	11.2	17.44	6.88	12.39

Date:	3/26/2014					
Tube No:	1-5					
Sample Depth:	0.18-0.25 m					
	Wt. Tube+Sample (g):	628.54	Tube Dia. (cm):		7.297	
	Wt. Tube (g):	215.43	Tube Length (cm):		7.613	
	Wt. Sample (g):	413.11	Volume (cm^3):		318.4	
	ρ (g/cm^3):	1.30	ν (Assumed):		0.45	

ΔL	**f**	**Δt**	**L_{tt}/λ**	**v_s**	**G_{max}**	**E**
(mm)	(Hz)	(ms)	(-)	(m/s)	(kPa)	(kPa)
55.52	500	2.881	1.4	19.3	482	1398
55.52	750	2.726	2.0	20.4	538	1561
55.52	1000	2.631	2.6	21.1	578	1676
55.52	1250	2.543	3.2	21.8	619	1794
39.5	750	1.926	1.4	20.5	546	1583
39.5	1000	1.499	1.5	26.4	901	2613
39.5	1250	1.438	1.8	27.5	979	2839
39.5	1500	1.401	2.1	28.2	1032	2991
39.5	2000	1.354	2.7	29.2	1104	3203
39.5	2500	1.322	3.3	29.9	1158	3360
			Average:	24.4	793.7	2301.7

Pennetration	**Cone Mass**	**Cone Angle**	**k**	**S_u**
(mm)	(g)	(deg)	(-)	(kPa)
5.71	60	60	0.27	4.87
5.05	60	60	0.27	6.23
7.26	60	60	0.27	3.02
6.19	60	60	0.27	4.15
7.55	60	60	0.27	2.79
4.13	60	60	0.27	9.32
6.06	60	60	0.27	4.33
6.52	60	60	0.27	3.74
			Average:	4.8

Vane	**q_u read.**	**q_u**	**q_u**	**S_u**
(-)	(kg/cm2)	(kg/cm2)	(kPa)	(kPa)
0.2	0.54	0.11	10.6	5.3
0.2	0.46	0.09	9.0	4.5
			Average:	4.9

Test	FC-1	FC-2	TV-1	TV-2
Wt. Soil+Tare (g)	9.88	14.55	19.02	18.44
Wt. DrySoil+Tare (g)	4.04	7.21	7.04	8
Wt. Water (g)	5.84	7.34	11.98	10.44

Date:	6/6/2014					
Tube No:	1-6					
Sample Depth:	0.08-0.15 m					
	Wt. Tube+Sample (g):	603.78	Tube Dia. (cm):		7.261	
	Wt. Tube (g):	215.75	Tube Length (cm):		7.593	
	Wt. Sample (g):	388.03	Volume (cm^3):		314.4	
	ρ (g/cm^3):	1.23	ν (Assumed):		0.45	
ΔL	**f**	**Δt**	**L_{tt}/λ**	**v_s**	**G_{max}**	**E**
(mm)	(Hz)	(ms)	(-)	(m/s)	(kPa)	(kPa)
53.82	600	1.811	1.1	29.7	1090	3161
53.82	800	1.746	1.4	30.8	1173	3401
53.82	1000	1.709	1.7	31.5	1224	3549
53.82	1250	1.681	2.1	32.0	1265	3669
53.82	1500	1.672	2.5	32.2	1279	3708
30.12	900	1.091	1.0	27.6	941	2728
30.12	1000	1.044	1.0	28.9	1027	2979
30.12	1250	0.951	1.2	31.7	1238	3590
30.12	1500	0.866	1.3	34.8	1493	4329
30.12	1750	0.801	1.4	37.6	1745	5060
			Average:	31.7	1247.4	3617.4
Pennetration	**Cone Mass**	**Cone Angle**	**k**	**S_u**		
(mm)	(g)	(deg)	(-)	(kPa)		
2.57	60	60	0.27	24.06		
2.29	60	60	0.27	30.30		
3.99	60	60	0.27	9.98		
5.45	60	60	0.27	5.35		
3.8	60	60	0.27	11.01		
5.1	60	60	0.27	6.11		
			Average:	14.5		
Vane	**q_u read.**	**q_u**	**q_u**	**S_u**		
(-)	(kg/cm2)	(kg/cm2)	(kPa)	(kPa)		
1.0	0.15	0.15	14.7	7.4		
0.2	0.41	0.08	8.0	4.0		
			Average:	5.7		
Test	FC-1	FC-2	TV-1	TV-2		
Wt. Soil+Tare (g)	20.01	15.06	15.50	14.19		
Wt. DrySoil+Tare (g)	15.15	5.97	9.46	5.29		
Wt. Water (g)	4.86	9.09	6.04	8.9		
Wt. Tare (g)	1.27	1.29	1.27	1.27		
Wt. DrySoil (g)	13.88	4.68	8.19	4.02		

Date:	6/6/2014		
Tube No:	1-6		
Sample Depth:	0.15-0.23 m		
Wt. Tube+Sample (g):	546.63	Tube Dia. (cm):	7.240
Wt. Tube (g):	214.76	Tube Length (cm):	7.573
Wt. Sample (g):	331.87	Volume (cm^3):	311.8
ρ (g/cm^3):	1.06	ν (Assumed):	0.45

ΔL	**f**	**Δt**	**L_{tt}/λ**	**v_s**	**G_{max}**	**E**
(mm)	(Hz)	(ms)	(-)	(m/s)	(kPa)	(kPa)
55.09	500	2.295	1.1	24.0	613	1779
55.09	600	2.156	1.3	25.6	695	2015
55.09	750	2.016	1.5	27.3	795	2305
55.09	1000	1.84	1.8	29.9	954	2767
55.09	1250	1.701	2.1	32.4	1116	3238
37.44	750	1.359	1.0	27.5	808	2343
37.44	1000	1.74	1.7	21.5	493	1429
37.44	1250	2.628	3.3	14.2	216	627
37.44	1500	1.623	2.4	23.1	566	1643
			Average:	25.1	695.2	2016.1

Pennetration	**Cone Mass**	**Cone Angle**	**k**	**S_u**
(mm)	(g)	(deg)	(-)	(kPa)
4.56	60	60	0.27	7.64
2.88	60	60	0.27	19.16
2.38	60	60	0.27	28.06
5.67	60	60	0.27	4.94
6.23	60	60	0.27	4.09
5.8	60	60	0.27	4.72
			Average:	11.4

Vane	**q_u read.**	**q_u**	**q_u**	**S_u**
(-)	(kg/cm2)	(kg/cm2)	(kPa)	(kPa)
0.2	0.56	0.11	11.0	5.5
0.2	0.50	0.10	9.8	4.9
			Average:	5.2

Test	FC-1	FC-2	TV-1	TV-2
Wt. Soil+Tare (g)	14.64	16.20	11.24	12.29
Wt. DrySoil+Tare (g)	3.57	5.89	2.93	4.07
Wt. Water (g)	11.07	10.31	8.31	8.22
Wt. Tare (g)	1.27	1.28	1.29	1.27
Wt. DrySoil (g)	2.3	4.61	1.64	2.8
w (%)	481.3	223.6	506.7	293.6

Date:	6/6/2014					
Tube No:	1-6					
Sample Depth:	0.23-0.30 m					
	Wt. Tube+Sample (g):	551.87		Tube Dia. (cm):	7.248	
	Wt. Tube (g):	217.44		Tube Length (cm):	7.648	
	Wt. Sample (g):	334.43		Volume (cm^3):	315.6	
	ρ (g/cm^3):	1.06		ν (Assumed):	0.45	

ΔL	**f**	**Δt**	**L_{tt}/λ**	**v_s**	**G_{max}**	**E**
(mm)	(Hz)	(ms)	(-)	(m/s)	(kPa)	(kPa)
56.57	300	3.299	1.0	17.1	312	904
56.57	400	3.215	1.3	17.6	328	952
56.57	500	3.02	1.5	18.7	372	1078
56.57	600	2.918	1.8	19.4	398	1155
56.57	700	2.956	2.1	19.1	388	1126
40.23	400	2.678	1.1	15.0	239	694
40.23	500	2.651	1.3	15.2	244	708
40.23	600	2.455	1.5	16.4	285	825
40.23	750	2.604	2.0	15.4	253	734
			Average:	17.1	313.2	908.3

Pennetration	**Cone Mass**	**Cone Angle**	**k**	**S_u**
(mm)	(g)	(deg)	(-)	(kPa)
3.94	60	60	0.27	10.24
4.06	60	60	0.27	9.64
3.8	60	60	0.27	11.01
2.36	60	60	0.27	28.53
6.73	60	60	0.27	3.51
4.3	60	60	0.27	8.60
			Average:	11.9

Vane	**q_u read.**	**q_u**	**q_u**	**S_u**
(-)	(kg/cm2)	(kg/cm2)	(kPa)	(kPa)
0.2	0.45	0.09	8.8	4.4
0.2	0.45	0.09	8.8	4.4
			Average:	4.4

Test	FC-1	FC-2	TV-1	TV-2
Wt. Soil+Tare (g)	13.46	13.77	11.56	13.86
Wt. DrySoil+Tare (g)	3.25	3.63	2.97	3.43
Wt. Water (g)	10.21	10.14	8.59	10.43
Wt. Tare (g)	1.26	1.26	1.31	1.30
Wt. DrySoil (g)	1.99	2.37	1.66	2.13
w (%)	513.1	427.8	517.5	489.7